

SURFACE INTEGRITY OF LASER CUTTING NITINOL SHAPE MEMORY ALLOY

by

CHENHAO FU

YUEBIN GUO, COMMITTEE CHAIR

MARK E. BARKEY
J. BRIAN JORDON
GREGORY B. THOMPSON
MARK L. WEAVER

A DISSERTATION

Submitted in partial fulfillment of the requirements
for the degree of Doctor of Philosophy in the
Department of Mechanical Engineering
in the Graduate School of
The University of Alabama

TUSCALOOSA, ALABAMA

2015

ABSTRACT

Every year, millions of people experience new or recurrent stroke or heart attack. Cholesterol plaque buildup is the culprit for these fatal diseases. One standard procedure to treat these diseases is inserting a stent into the arteries to retain the blood flow.

Stent materials are critical for product performance and functionality. Nitinol, a nearly equiatomic nickel-titanium shape memory alloy, has been widely used to fabricate vascular stents due to the excellent mechanical properties, fatigue and corrosion resistance, and biocompatibility. The challenges for manufacturing Nitinol stents are manifested in two aspects: (i) stents are miniature devices that demand a very precise and complex meshed geometry; and (ii) Nitinol is very difficult to be shaped by mechanical cutting due to strong work hardening, excessive tool wear, and bur formation. These technical hurdles can be overcome by laser cutting. A fine focused laser beam can produce a micrometer size kerf on Nitinol, and the non-contact thermal process can also eliminate pressing issues inherent in mechanical cutting.

Conventional dry laser cutting is a high-temperature process which may generate thermal damage such as heat affected zone (HAZ), recast layer, micro-cracks, and tensile residual stresses. The thermal damage and ablation-induced contamination are critical technical barriers for fatigue performance and biocompatibility of Nitinol stents.

To reveal the underlying process mechanism of laser cutting nitinol, this research focuses on the following aspects: (1) A critical assessment on the state-of-the-art of laser cutting Nitinol was conducted. (2) Low plasticity burnishing (LPB) was used to understand the deformation

behavior and material properties of superelastic Nitinol. A method of modeling superelasticity and thermal shape memory of Nitinol was developed. (3) A 3-dimensional finite element model of pulsed laser cutting was developed to better understand the process mechanism in laser cutting of Nitinol. A novel thermal loading model with high spatial accuracy was developed to simulate a moving volumetric pulsed heat flux. The predicted kerf geometry and dimensions agreed well with experimental data. Also, the effects of cutting speed, pulse power, and pulse width on kerf profile, temperature, and heat affected zone (HAZ) were investigated. (4) A fiber laser cutting system was instrumented to experimentally investigate surface integrity of Nitinol. In addition, the process window for optimal surface integrity was identified. (5) Tensile and fatigue testing was conducted to evaluate the impact of surface integrity including thermal damage of laser cut Nitinol on static strength and fatigue performance. (6) Recommendations for possible future research directions were also outlined.

DEDICATION

This work is dedicated to my wife and my parents.

LIST OF ABBREVIATIONS AND SYMBOLS

E^*	Effective modulus
E_1	Elastic modulus of the burnishing tool
E_2	Elastic modulus of the workpiece
ν_1	Poisson's ratio of the burnishing tool
ν_2	Poisson's ratio of the workpiece
R	Effective curvature
R_1	Curvature of tool
R_2	Curvature of the workpiece
F	Burnishing force
P	Load input
r	Radius of the tool
a	Contact radius
p_0	Maximum contact pressure
δ	Approach of distant points
τ_1	Maximum shear stress
σ_r	Maximum tensile stress
$\sigma_{1,2,3}$	Principal stresses
E_a	Austenite elasticity
V_a	Austenite Poisson's ratio

E_m	Martensite elasticity
V_m	Martensite Poisson's ratio
ε^L	Transformation strain
$(\frac{\delta\sigma}{\delta T})_L$	$(\frac{\delta\sigma}{\delta T})$ loading
σ_L^S	Start of transformation loading
σ_L^E	End of transformation loading
T_0	Reference temperature
$(\frac{\delta\sigma}{\delta T})_U$	$(\frac{\delta\sigma}{\delta T})$ unloading
σ_U^S	Start of transformation unloading
σ_U^E	End of transformation unloading
σ_{CL}^E	Start of transformation stress during loading in compression, as a positive value
ε_V^L	Volumetric transformation strain
N_p	Number of stress-strain pairs to define yield curve
$\sigma_I^p, \varepsilon_I, \dots, \sigma_{11}^p, \varepsilon_{11}$	Stress-strain points in the yield curve
S_{22}	Normal stress in width direction
S_{33}	Normal stress in depth direction
PE_{33}	Plastic strain in depth direction
z	Distance underneath the surface
P	Laser power
P_{peak}	Peak pulse power
τ	Pulse width
f	Laser frequency
I	Laser intensity

A	Laser absorption coefficient
R_o	Laser spot radius on the top surface
R_b	Laser spot radius on the bottom surface
B	Gaussian shape factor
r	Distance to beam center
m	Ratio of period to pulse width
N	N^{th} period
h	Sample thickness
D	Decay coefficient to define conical shape of volumetric heat flux
v	Laser cutting speed
t	Simulation time
r	Instantaneous laser spot radius
E	Pulse energy
ε	Total strain
ε^{el}	Elastic strain
ε^{tr}	Transformation strain
ε^L	Maximum residual strain
ζ_s	Fraction of martensite under loading
t	Deviatoric stress
F	Drucker-Prager-type loading function
C^{AS}	Material constant
H^{AS}	Activation of the phase transformation
α	Taper angle
d_{entry}	Width of entry kerf
d_{exit}	Width of exit kerf

ACKNOWLEDGEMENTS

I would like to thank my research advisor, Dr. Yuebin Guo, for his visionary technical guidance and financial support in conducting this research. His mentorship has allowed me to accomplish the professional and personal goals in my graduate school career for which I am truly grateful. I would also like to thank all my committee members, Drs. Mark Barkey, Brian Jordon, Gregory Thompson, and Mark Weaver for their invaluable input, inspiring questions, and support to the research.

I would like to acknowledge my fellow students for their support, help, and most importantly friendship during the progress of this research: Zack Snyder, John McKinney, Michael Sealy, Wei Li, Mesiam Salahshoor, Jingfu Liu, Ziyu Liu, Dan Zhang, Chao Li, and Dongwei Sun. My thanks also goes to Mr. Kenneth Dunn, James Yarbrough, Jim Edmonds, and Sam Tingle in the machine shop for their assistance in making testing samples and sharing experience.

CONTENTS

ABSTRACT	ii
DEDICATION	iv
LIST OF ABBREVIATIONS AND SYMBOLS	v
ACKNOWLEDGEMENTS	viii
LIST OF TABLES	xvi
LIST OF FIGURES	xvii
1. INTRODUCTION	1
1.1 Nitinol Vascular Stents	1
1.1.1 Motivation.....	1
1.1.2 Stent Functions.....	3
1.1.3 Nitinol Shape Memory Alloy.....	3
1.1.4 Nitinol Stents Manufacturing.....	4
1.2 Requirements for High Performance Stents	5
1.3 Current Problems	6
1.4 Research Objectives.....	7
1.5 References.....	8
2. STATE-OF-ART, CHALLENGES, AND OUTLOOK ON LASER CUTTING OF NITINOL VASCULAR STENT	10
2.1 Nitinol Vascular Stents	10
2.1.1 Nitinol Stents: Functions and Design Principles	10

2.1.2	Manufacturing Process Chain of Nitinol Stents.....	13
2.1.3	Critical Issues for High Performance Nitinol Stents.....	14
2.2	Nitinol Material.....	16
2.2.1	Nitinol and Nitinol History	16
2.2.2	Nitinol Properties	16
2.3	Laser Cutting of Nitinol Stents	19
2.3.1	Laser Introduction.....	19
2.3.2	Laser Types.....	20
2.3.3	Long Pulse Lasers vs. Ultra-short Pulse Lasers.....	22
2.3.4	Long Pulse Laser Processing of Nitinol.....	24
2.3.5	Advantages/Disadvantages for Long Pulse Lasers	28
2.3.6	Ultra-short Pulse Laser Processing of Nitinol	30
2.3.7	Advantages/Disadvantages for Ultra-short Pulse Lasers	33
2.4	Water-assisted Laser Cutting of Nitinol	34
2.4.1	Process Concept	34
2.4.2	Experimental Setup.....	34
2.4.3	Surface Integrity Improvement	35
2.5	Surface Integrity on Fatigue.....	38
2.5.1	FDA Requirement.....	38
2.5.2	Fatigue Testing Methods.....	38
2.5.3	Fatigue Crack Growth Behavior	41
2.5.4	Effect of Surface Integrity on Fatigue	43
2.6	Surface Integrity on Corrosion.....	44

2.7	Pressing Issues/Challenges	46
2.8	References.....	48
3.	A STUDY OF DEFORMATION BEHAVIOR AND MATERIAL PROPERTIES OF NITINOL USING LOW PLASTICITY BURNISHING.....	57
	Abstract.....	57
3.1	Introduction.....	59
3.1.1	Nitinol Alloy	59
3.1.2	Surface Integrity.....	60
3.1.3	Low Plasticity Burnishing.....	60
3.1.4	Research Objective	61
3.2	LPB Experiment.....	62
3.2.1	Experimental Setup.....	62
3.2.2	SE508 Work Material	64
3.3	LPB Process Analysis	65
3.3.1	Burnishing Pressure/Force	65
3.3.2	Peak Pressure vs. Stress-Strain Curve	66
3.3.3	Track Depth/Width	68
3.3.4	Maximum Shear Stress and Location in Subsurface	69
3.4	Experimental Results	71
3.4.1	Characterization of Burnishing Tracks	71
3.5	Finite Element Analysis Procedure.....	73
3.5.1	Mesh.....	73
3.5.2	Loading Condition	75
3.5.3	Modeling of Superelastic-Plastic Behavior of SE508	75

3.6	Simulation Results	77
3.6.1	Dent Profiles vs. Experimental Data.....	77
3.6.2	Stress Profiles of Loaded Condition	78
3.6.3	Residual Stress and Strain Profiles	81
3.6.4	Convergence Analysis	82
3.7	Conclusions.....	83
3.8	References.....	84
4.	A PREDICTIVE MODEL AND VALIDATION OF LASER CUTTING OF NITINOL WITH A NOVEL MOVING VOLUMETRIC PULSED HEAT FLUX	87
	Abstract	87
4.1	Introduction.....	88
4.1.1	Nitinol Material.....	88
4.1.2	Laser Cutting of Nitinol	90
4.1.3	Problem and Objectives	91
4.2	Heat Flux Modeling in Laser Cutting	92
4.3	Simulation Procedure.....	96
4.3.1	Mesh.....	96
4.3.2	Modeling of Moving Volumetric (3D) Heat Flux of Pulse Laser	97
4.3.3	Simulation Conditions	100
4.4	Modeling of Nitinol Superelasticity and Shape Memory	102
4.4.1	Mechanical Behavior	102
4.4.2	Physical Properties.....	105
4.5	Results and Discussion	106

4.5.1	Prediction and Validation of Kerf Geometry	106
4.5.2	Laser Cutting Temperature and Stress Development	109
4.5.3	Heat Affected Zone (HAZ).....	110
4.6	Conclusions.....	111
4.7	References.....	112
5.	PROCESS – SURFACE INTEGRITY MAP IN FIBER LASER CUTTING OF SHAPE MEMORY ALLOY	115
	Abstract	115
5.1	Introduction.....	116
5.2	Laser Cutting Experimental Procedure	117
5.3	Process - Surface Integrity Map.....	118
5.3.1	Kerf Profile	118
5.3.2	Surface Roughness.....	119
5.3.3	Subsurface Microstructure Characterization.....	121
5.3.4	Element Analysis	123
5.3.5	Nanohardness Profile and HAZ	124
5.3.6	Process – Surface Integrity Map for Optimal Surface Integrity	125
5.4	Process Mechanisms	126
5.5	Conclusions.....	129
5.6	References.....	130
6.	THE EFFECT OF SURFACE INTEGRITY ON TENSILE AND FATIGUE STRENGTH OF NITINOL BY FIBER LASER CUTTING	132
	Abstract	132
6.1	Introduction.....	133

6.1.1	Nitinol Material.....	133
6.1.2	Stent Application and Laser Cutting Process.....	133
6.1.3	Research Objective	134
6.2	Literature Review.....	135
6.2.1	Effect of Surface Integrity on Tensile Performance by Laser Cutting.....	135
6.2.2	Effect of Surface Integrity on Fatigue Performance by Laser Cutting.....	136
6.3	Experimental Procedure.....	138
6.3.1	Laser Cutting Experimental Setup	138
6.3.2	Experimental Conditions	138
6.3.3	Surface Integrity Characterization	140
6.3.4	Tensile and Fatigue Testing	141
6.4	Experimental Results	141
6.4.1	Surface Integrity.....	141
6.4.2	Tensile Testing.....	144
6.4.3	Fatigue Testing.....	147
6.5	Finite Element Analysis.....	149
6.5.1	Mesh.....	149
6.5.2	Material Modeling of Nitinol.....	150
6.6	Simulation Results	153
6.6.1	Load – Displacement	153
6.6.2	Stress Evolution	154
6.6.3	Phase Transformation	155
6.7	Conclusion	156

6.8	Reference	157
7.	SUMMARY, CONCLUSIONS AND RECOMMENDATIONS.....	160
7.1	Summary and Conclusions	160
7.2	Recommendations.....	161
7.2.1	Improvement on the Laser Cutting Process.....	161
7.2.2	Surface Treatment after Laser Cutting.....	162
7.2.3	Fatigue Testing.....	162

LIST OF TABLES

2.1	Stent Types, Materials and Advantages/Disadvantages	11
2.2	General Comparison of Different Types of Lasers.....	22
2.3	Common Fatigue Testing Sample Forms, Testing Method, and Key Findings.....	41
3.1	Composition of the SE508 Nitinol.....	64
3.2	Material Properties of the LPB Ball.....	66
3.3	LPB Experiment Plan	67
3.4	Pressure vs. Burnishing Depth/Width.....	69
3.5	LPB Loading in FEA Simulations	75
3.6	Material Constants of SE508 Nitinol.....	77
4.1	Representative Heat Flux Models.....	94
4.2	Simulation Conditions	100
4.3	UMAT Material Constants of Nitinol.....	105
4.4	Physical Properties of Nitinol.....	106
5.1	Laser Cutting Conditions	118
6.1	Compositions of Nitinol SE508.....	138
6.2	Laser Cutting Conditions for Three Levels of Surface Integrity	140
6.3	UMAT Material Constants of Nitinol in Tension.....	152

LIST OF FIGURES

1.1	Trends on stenting procedure and bypass in the U.S., 1996-2010.....	2
1.2	Total global market size and growth for coronary stent devices by region, 2010-2016.....	2
1.3	Cardiovascular stent.....	3
1.4	Schematic of laser cutting stent setup.....	5
2.1	(a) a biodegradable urethral stent with tubular mesh, (b) a typical metallic coronary stent, (c) a tubular slot balloon expandable magnesium alloy stent, and (d) a polymer coated metallic stent showing the microdrop structure	12
2.2	(a) stent design pyramid, (b) a typical manufacturing process chain for stents.....	13
2.3	Stress-strain-temperature diagram of Nitinol.....	18
2.4	Biomechanical compatibility of Nitinol: deformation behavior compared with living tissues.....	19
2.5	Typical components of a laser.	20
2.6	Schematic of laser cutting front	23
2.7	A drilled hole on steel using pulse duration of (a) 3.3 ns and (b) 200 fs.....	24
2.8	Optical images showing laser cut kerfs of Nitinol.....	25
2.9	Typical striation pattern in laser cutting in the form of periodic lines.....	26
2.10	(a) Optical image shows the microstructure around the cut surface at the speed of 6.7mm/s, (b) Hardness profile at different cutting speed. The authors used a pulsed Nd:YAG laser to cut Nitinol	27

2.11	Stent for (a) as cut, (b) pickled, (c) annealed, and (d) electropolished	29
2.12	(a) An optical micrograph shows the microstructure under the machined surface (arrow), (b) Microhardness at various depths from the machined surfaces (as compared to Nd:YAG laser. The authors used 150 fs femtosecond laser to process Nitinol	32
2.13	Average induced stress as a function of laser fluence for (a) femtosecond laser (b) nanosecond laser.	33
2.14	Schemes of water-assisted laser cutting process.....	34
2.15	SEM images of the back wall: (a) dry cutting and (b) wet cutting	36
2.16	(a) Dry cutting showing debris and recast, (b) underwater cutting is debris-free and recast free result	36
2.17	Cut in 50 μm stainless steel sheet with (a) water-jet guided laser system and (b) remote laser system. Please note the identical scale of these microscope images.....	37
2.18	Crack growth parameters (Paris exponent m and fatigue threshold ΔK_{th}) for Nitinol as a function of R ratio. As expected, the threshold values decrease with increasing R ratio. Data are presented as mean \pm one standard deviation	42
2.19	Fatigue life for the unwelded sample and weldment at different rotational speed	44
2.20	Potentiodynamic cyclic polarization for Nitinol disc samples. (1) Mechanically polished (Mp), (2) chemically etched (Ce), (3) electropolished (Ep), (4) chemically etched, boiled in water and heat treated (CeWbHt) samples	46
3.1	Schematic of low plasticity burnishing (LPB).....	62
3.2	LPB fixture design.	63
3.3	LPB experimental setup.....	63
3.4	Quasi-static mechanical properties compared with Hertz peak pressure	67
3.5	Burnishing pressure vs. theoretical and experimental depth	72
3.6	Three-dimensional FEA of burnishing (not to scale).	74

3.7	Superelastic-plastic behavior based on the uniaxial behavior	76
3.8	Experimental and simulated track profiles.	78
3.9	Von Mises stress (a) S33 stress (b) S22 stress, and (c) in subsurface	79
3.10	(a) S22 stress and (b) S33 stress (b) in width direction	80
3.11	3D contour of shear stress.....	80
3.12	Residual stress and strain profiles in subsurface.....	81
3.13	Max. S33 and PE33 in the subsurface	82
3.14	Deformation at rolling end vs. element number	83
4.1	Stress-strain-temperature diagram of Nitinol.....	88
4.2	(a) Cardiovascular Nitinol stent by laser cutting, (b) laser cutting schematic	89
4.3	Simulation schematic of pulsed laser cutting.....	97
4.4	Schematic of the moving volumetric heat flux of pulsed laser.....	98
4.5	Modeling procedure of moving volumetric heat flux of pulsed laser.....	99
4.6	Laser pulse shape for simulation cases 7, 8, and 9	101
4.7	Superelastic-plastic characteristics of Nitinol.....	104
4.8	(a) Representative prediction of laser cut kerf and (b) comparison between predicted and measured striated surfaces	106
4.9	The effect of cutting speed, peak power, and pulse width on (a) kerf width and (b) taper	107
4.10	The effects of cutting speed, peak power, and pulse width on (a) temperature and (b) stress in the subsurface.....	110
4.11	The effect of cutting speed, peak power, and pulse width on HAZ thickness	111
5.1	Fiber laser cutting Nitinol SMA – process characteristics.....	117
5.2	Kerf width as a function of laser power and cutting speed.....	119

5.3	(a) Roughness as a function of laser power and cutting speed; (b-c) surface topography w. low and high roughness	120
5.4	Measure of the effect size (η^2), i.e. measure of the degree of association between process parameters and kerf characteristics.....	121
5.5	Representative kerf geometry: (a) clean cut w.o. dross, (b) rough cut w. recast and dross, and (c) top view of the entry recast	122
5.6	(a, b) EBSD grain boundary; (c, d) grain misorientation.....	123
5.7	EDS of the machined surface: (a) high power w. low speed; (b) low power w. high speed.....	124
5.8	Representative nanohardness profile in the subsurface.	125
5.9	Process – surface integrity map for optimal surface integrity.	126
5.10	(a) 3D simulation setup; (b) modeling of moving pulsed volumetric heat flux.	127
5.11	The predicted and measured surface topography: (a-c) high power w. low speed, (d-f) low power w. high speed.	129
6.1	Laser cutting Nitinol experimental setup (a) laser cutting system configuration, (b) Nitinol sheet sample before cut, (c) Nitinol sample after laser cut, and (d) sample dimensions.....	139
6.2	Representative samples with three distinct levels of surface integrity. ...	142
6.3	Nanohardness profiles in the subsurface.....	143
6.4	Tensile testing setup.....	145
6.5	Load displacement curves for different laser cutting conditions	145
6.6	Fracture load at three surface integrity levels	146
6.7	Fracture load as a function of (a) roughness and (b) max. recast thickness.....	147
6.8	Fatigue testing setup	147
6.9	Fatigue life at three levels of surface integrity.....	148

6.10	Fatigue life as a function of (a) roughness and (b) max. recast thickness.....	149
6.11	Simulation schematic of tensile and fatigue loading	150
6.12	Superelastic-plastic behavior based on the uniaxial behavior	152
6.13	Predicted load – displacement curve and the experimental data	153
6.14	von Mises stress evolution at different displacements.....	154
6.15	S22 distribution along the thickness direction at different displacements	155
6.16	Martensitic transformation at the stress concentration locations	156
7.1	Schematic of water assisted laser cutting setup	161

CHAPTER 1

INTRODUCTION

1.1 Nitinol Vascular Stents

1.1.1 Motivation

Cholesterol plaque buildup is the culprit for heart attack and stroke. American Heart Association data shows near 800,000 people in the US experience a new or recurrent stroke every year. It accounts for 1 of 18 deaths in the US. If the plaque buildup reaches a dangerous level, patients have to be surgically treated using bypass or angioplasty which places a stent into the arteries to push the plaque against the wall to retain the blood flow. Since stenting procedure is less invasive and more economic, the use of vascular stents becomes a major choice as shown in [Fig. 1.1](#) [1]. It is expected that the global market for coronary stents will reach \$ 10.6 billion by 2016 as shown in [Fig. 1.2](#) [2].

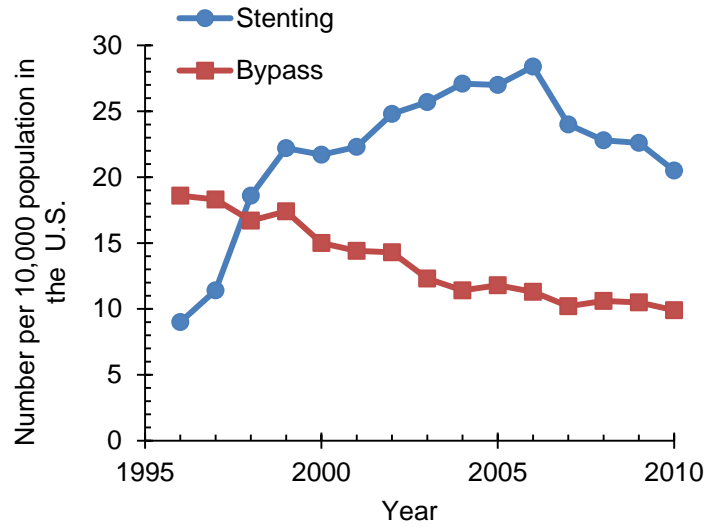


Fig. 1.1 Trends on stenting procedure and bypass in the U.S., 1996-2010 [1].

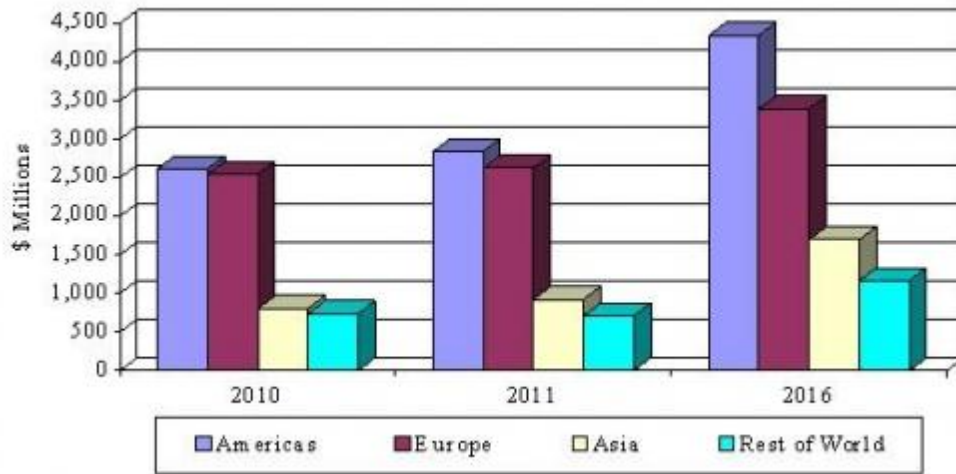


Fig. 1.2 Total global market size and growth for coronary stent devices by region, 2010-2016 [2].

1.1.2 Stent Functions

A stent is a cylindrical meshed medical device used to widen a narrow or stenosed lumen in order to maintain the patency of the lumen (Fig. 1.3). Currently, stents are being increasingly used to cure plaque related diseases associated with blood vessels and gastrointestinal, renal, and biliary tracts [3].

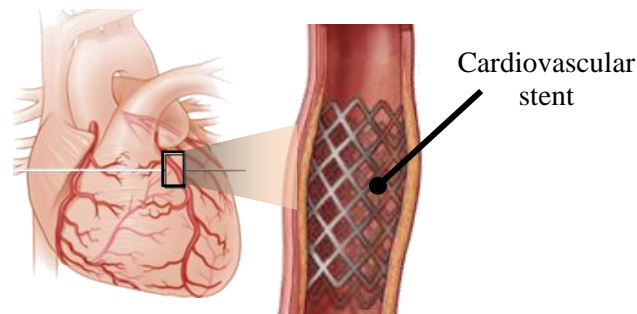


Fig. 1.3 Cardiovascular stent.

There are two main methods for stent delivery. The first one is balloon-expanded stent delivery. In this method, the stent is slipped over the outside of a balloon catheter. When the catheter is positioned at right place, the balloon is inflated and the stent expands. The second technique is self-expanding stent delivery. The self-expanding stents are manufactured into their expanded shape and then cooled and compressed to fit within a catheter. After the catheter is delivered at the appropriate position, the stent will expand to its pre-defined shape elastically upon the removal of constraint [4].

1.1.3 Nitinol Shape Memory Alloy

The stent materials are critical for product performance and functionality. Traditional materials such as polymers, stainless steel, and cobalt-chromium have been used in stent

manufacturing for over 20 years. However the unmet medical needs have led to the efforts of improving material properties and developing new material for vascular stents.

Nitinol, a nearly equiatomic nickel-titanium shape memory alloy, has been widely used to fabricate vascular stents due to the superelasticity and thermal shape memory. In addition, Nitinol has excellent biocompatibility and fatigue and corrosion resistance, which also make Nitinol popular in fabricating stents [5].

1.1.4 Nitinol Stents Manufacturing

Stents can be manufactured by conventional methods such as braiding and knitting. Wire material is used in these processes. The advantages of these processes are that adjustable flexibility can be achieved with relatively simple operations. However, these processes have very low efficiency. Photochemical etching is also widely used to manufacture stents. The advantages of this process include a large number of parts can be processed in a single run [6] and free of stress and burr [7]. The limitation of the process is the low aspect ratio (depth/width) of 1:1 which prevents this technique to manufacture standard coronary stents (aspect ratio 5:1 to 12:1) [7].

By far, the vast majority of coronary stents are produced by laser cutting from tubes [6,8]. The common setup (Fig. 1.4) [9] of the laser cutting process is using a finely focused Nd:YAG laser beam passing through coaxial gas jet structure to imping on the surface of the tube, in which the linear and rotary velocity of the tube is precisely controlled [10]. In this setup, the laser is mounted on the translation/rotation system. The system moves the tube with respect to the laser beam in order to cut the tube into the designed structure.

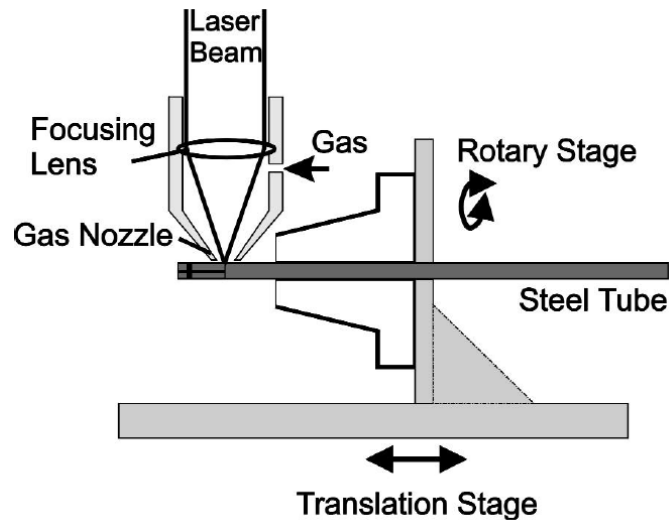


Fig. 1.4 Schematic of laser cutting stent setup [9].

1.2 Requirements for High Performance Stents

Based on the International Standard ISO 25539-2: “*Cardiovascular implants- Endovascular devices-Part 2: Vascular Stent*” [11], the intended performance of the stent shall include at least the following specifications:

- The ability of the stent should be consistently, accurately and safely deployed.
- The ability of the stent to ensure effective fixation and apposition in the intended location within the vasculature.
- The ability of the stent to maintain adequate integrity.
- The consistency of the stent to dimensions and its design for compatibility for use in specified vessel diameters.
- The ability of the stent to maintain adequate flood flow through the lumen.
- The compatibility of the stent with exposure to magnetic resonance imaging (MRI) field.

- The stent should meet specified biocompatibility requirement of ISO 10993 series.
- The visibility of the stent under fluoroscopy or other technology.

It is also suggested that fatigue testing of the stent should include in vitro testing until ten-year equivalent cycles in an appropriate test solution to simulate physiological condition.

According to the “*Non-clinical engineering tests and recommended labeling for intravascular stents and associated delivery systems*” by U.S. Food and Drug Administration (FDA) in 2010 [12], stent defects as a result of manufacturing or subsequent damage can contribute to clinical complications.

1.3 Current Problems

The pressing problems in laser cutting Nitinol are summarized as follows:

- Conventional dry laser cutting is a high-temperature process which generates a heat-affected zone (HAZ) that modifies the surface and near-surface microstructure and properties. This is a particular disadvantage in biomedical stents where a white/recast layer can form that contains a modified microstructure, oxidation, microcracks, and tensile residual stress. This thermal damage and ablation-induced contamination would be very detrimental to fatigue performance of Nitinol stents machined by dry laser cutting, which is a major concern for stent manufacturers [13].
- Phase transformation (austenite-martensite) temperatures of Nitinol are very low (-100°C–100°C). The laser-induced thermal loading and Nitinol’s unique properties couple where recovery, recrystallization, and phase transformation are

prevalent. As a result, surface integrity becomes a major concern. Yet, little research has been done in elucidating the mechanism of surface integrity which is critical for stents.

- Furthermore, the process-induced surface integrity, in particular white layer, on fatigue behavior (endurance and crack behavior) has yet to be understood.

1.4 Research Objectives

This research aims to produce superior surface integrity, achieve high durability in laser cutting Nitinol shape memory alloy, and understand the basic science underlying the intrinsic laser cutting-property-function relationship.

To realize this objective, a synergistic experimental, theoretical, and computational study is planned as follows:

- Understand deformation behavior and material properties using low plasticity burnishing.
- Understand the basic material removal mechanism of laser cutting process by developing a multiphysics simulation model using thermal loading subroutine and a material subroutine of shape memory and superelasticity of Nitinol.
- Create a fiber laser cutting process to efficiently machine Nitinol and conduct comprehensive experimental study to determine the influence of critical process parameters on surface integrity (surface finish, edge quality, microstructure, residual stress, micro/nano-hardness, and chemical compositions).
- Determine the process-induced surface integrity including white layer on static strength and fatigue performance.

This dissertation is a compilation of seven chapters. The 1st chapter gives the research motivation, research problems and objectives. The 2nd chapter provides a comprehensive literature review on surface integrity in laser cutting Nitinol. The 3rd chapter focuses on the understanding of material behavior using low plasticity burnishing. The 4th chapter has developed a finite element model of laser cutting of Nitinol with a pulsed moving volumetric heat flux. The 5th chapter focuses on the experimental study of the surface integrity of Nitinol by fiber laser cutting. The 6th chapter explores the static and fatigue properties of the laser cut Nitinol samples with distinct surface integrity. The last chapter discusses the future research directions.

1.5 References

- [1] Centers for Disease Control and Prevention. 2012. Discharges with at least one procedure in nonfederal short-stay hospitals, by sex, age, and selected procedures: United states, selected years 1990 through 2009-2010.
- [2] BCC Research L. 2013 Global markets for coronary stent devices – HLC111A. <www.bccresearch.com>.
- [3] H.J. Chun, E.S. Kim, J.J. Hyun, Y.D. Kwon, B. Keum, C.D. Kim, 2010, Gastrointestinal and biliary stents, *Journal of Gastroenterology and Hepatology*, 25(2): 234-243.
- [4] Pruitt LA and Chakravartula AM. 2011. *Mechanics of biomaterials: Fundamental principles for implant design*. Cambridge University Press.
- [5] T. Duerig, A. Pelton, D. Stöckel, 1999, An overview of nitinol medical applications, *Materials Science and Engineering: A*, 273: 149-160.
- [6] D. Stoeckel, C. Bonsignore, S. Duda, 2002, A survey of stent designs, *Minimally Invasive Therapy & Allied Technologies*, 11(4): 137-147.
- [7] A. Schuesseler, 2007, Manufacturing of stents: Optimize the stent with new manufacturing technologies, *New technologies in vascular biomaterials: fundamentals about stent II*, : 93-106.

- [8] D. Stoeckel, A. Pelton, T. Duerig, 2004, Self-expanding nitinol stents: Material and design considerations, *European Radiology*, 14(2): 292-301.
- [9] C. Momma, U. Knop, S. Nolte, 1999, Laser cutting of slotted tube coronary stents—state-of-the-art and future developments, *Progress in Biomedical Research*, 4(1): 39-44.
- [10] Y.P. Kathuria, 2005, Laser microprocessing of metallic stent for medical therapy, *Journal of Materials Processing Technology*, 170(3): 545-550.
- [11] ISO-25539-2. 2008. Cardiovascular implants - endovascular devices - part 2: Vascular stents.
- [12] U.S. Food and Drug Administration. 2010. Non-clinical engineering tests and recommended labeling for intravascular stents and associated delivery systems.
- [13] Z. Lin, A. Denison. 2004, *Medical Device Materials: Proceedings from the Materials & Processes for Medical Devices Conference 2003*, 8-10 September 2003, Anaheim, California, 205.

CHAPTER 2

STATE-OF-ART, CHALLENGES, AND OUTLOOK ON LASER CUTTING OF NITINOL VASCULAR STENT

2.1 Nitinol Vascular Stents

2.1.1 Nitinol Stents: Functions and Design Principles

Cholesterol plaque buildup is the culprit for heart attack and stroke. American Heart Association data shows near 795,000 people in the US experience a new or recurrent stroke every year. It accounts for 1 of 18 deaths in the US. If the plaque buildup reaches a dangerous level, surgery may be needed to remove the plaque. One of the normal procedures is called angioplasty which involves placing a stent into the arteries to push the plaque against the wall to retain the blood flow.

A stent is usually defined as a cylindrical medical device used to widen a narrow or stenosed lumen in order to maintain the patency of the lumen. Currently, stents are being increasingly used in blood vessels and gastrointestinal, renal, and biliary tracts [1].

The stent materials are critical for product performance and functionality. Traditional materials such as stainless steel and cobalt-chrome have been used in stent manufacturing for over 20 years. However the unmet medical needs have led to the efforts of improving material properties and developing new material for vascular stents. Based on the material and its degradability, stents can be categorized as degradable polymer stents, non-degradable bare metal

stent, degradable bare metal stent, and polymer coated metal stents. The possible materials, associated advantages and disadvantages are summarized in [Table 2.1](#). The example of each type of stent can be found in [Fig. 2.1](#).

Table 2.1 Stent Types, Materials and Advantages/Disadvantages

Stent type	Material	Advantages	Disadvantages
Degradable polymer stent	PLLA	<ul style="list-style-type: none"> • Drug-eluting • Degradability • Low stent thrombosis rate [2,3] 	<ul style="list-style-type: none"> • Inflammation [4] • Stent recoil [5] • Mechanical limitation [6] • Degradation uncontrolled [2]
Non-degradable bare metal stent	SS, Nitinol, CoCr	<ul style="list-style-type: none"> • Radiopacity • Preventing recoil [2] • Mechanical strength [4] 	<ul style="list-style-type: none"> • Fatigue issues [4] • No potential as drug carrier [4] • In-stent restenosis [2]
Degradable bare metal stent	Mg	<ul style="list-style-type: none"> • Degradability • Less inflammatory compared to polymers • Reduced restenosis rate [6] 	<ul style="list-style-type: none"> • Low radiopacity [3,4,6] • Degradation uncontrolled [2]
Polymer coated metal stents	CoCr, Nitinol, SS + PLA, PGA, PLGA	<ul style="list-style-type: none"> • Combined antirestenotic benefits of drug-eluting stent and safety benefits of bare-metal stents [7] 	<ul style="list-style-type: none"> • Drug releasing rate uncontrolled [7]

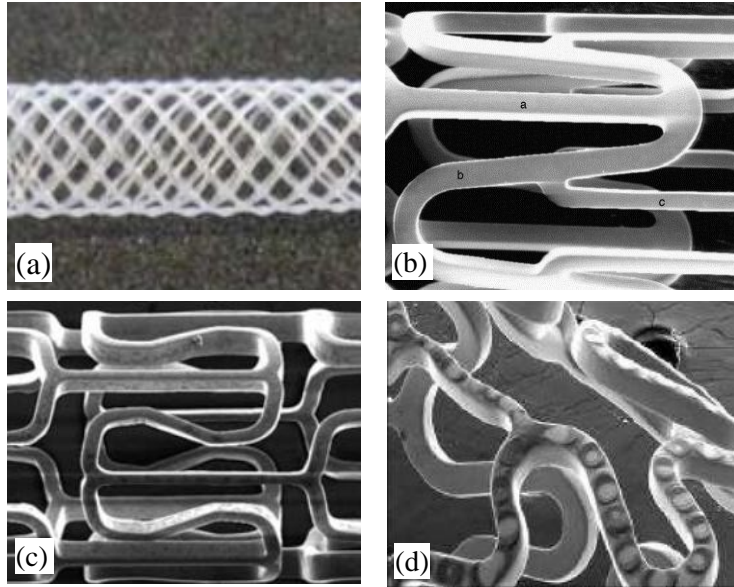


Fig. 2.1 (a) a biodegradable urethral stent with tubular mesh [8], (b) a typical metallic coronary stent [9], (c) a tubular slot balloon expandable magnesium alloy stent [6], and (d) a polymer coated metallic stent showing the microdrop structure [7].

In the past 30 years, dramatic changes have occurred in the composition and design of stents. For example, the first stent was made of plastic, and now, most stents are made of metal. For metallic stents, Nitinol alloys are preferred due to their flexibility and maintenance of shape in a curved lumen [10]. Moreover, the non-linear mechanical response of Nitinol is more close to natural materials, such as hair, bone, and tendon [11]. The design of Nitinol stents began with wire coils, since Nitinol was only available in wire form at that time. After Nitinol tube became available since mid-1990s, most Nitinol stent are made from laser cutting of Nitinol tubing [12]. With the continuous grow of micromachining capability, the development direction during the next decades will be: smaller, more flexible, and less invasive [13].

2.1.2 Manufacturing Process Chain of Nitinol Stents

Stoeckel et al. [14] proposed the concept of stent design pyramid (Fig. 2.2(a)). The starting point is materials used. Then the classification branches out into forms of materials, manufacturing methods, geometrical configurations, and additions to stents.

Stents can be manufactured by conventional methods such as braiding and knitting. Wire material is used in these processes. The advantages of these processes are adjustable flexibility can be achieved with relatively simple operations. However, these processes have very low efficiency. Photochemical etching is also widely used to manufacture stents. The advantages of this process include a large number of parts can be processed in a single run [14] and free of stress and burr [4]. The limitation of the process is the low aspect ratio (depth/width) of 1:1, which prevents the application of this technique to stent design of standard coronary stents (aspect ratio 5:1 to 12:1) [4].

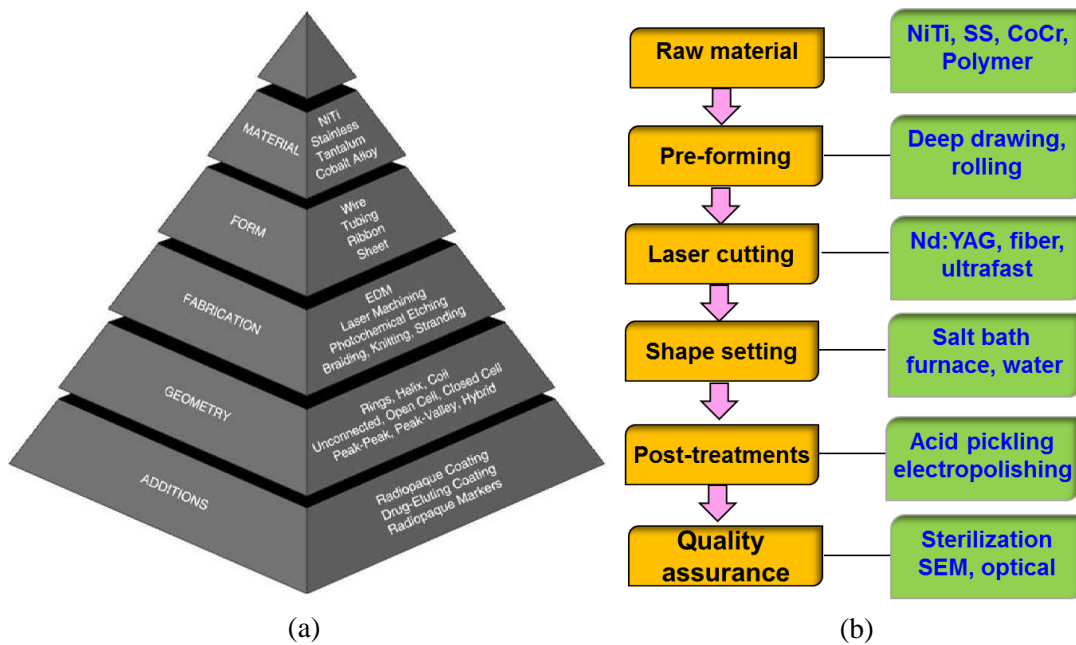


Fig. 2.2 (a) stent design pyramid [14], (b) a typical manufacturing process chain for stents.

By far, the vast majority of stents are produced by laser cutting from tubes [12,14]. The common setup of the laser cutting process is using a finely focused Nd:YAG laser beam passing through coaxial gas jet to imping on the surface of the tube as the linear and rotary velocity of the tube is precisely controlled [15]. In this setup, the laser is mounted on translation/rotation system. The system moves the tube with respect to the laser beam in order to cut the tube into the designed structure.

Post-processing is critical to enhanced stent performance. One of the most widely used post-processing techniques in stent manufacturing is electropolishing. This process is found to be not only increases the fatigue performance [16] but also the corrosion performance [12]. A detailed manufacturing process chain for stents can be found in [Fig. 2.2\(b\)](#).

2.1.3 Critical Issues for High Performance Nitinol Stents

Based on the International Standard ISO 25539-2: “*Cardiovascular implants- Endovascular devices-Part 2: Vascular Stent*” [17], the intended performance of the stent shall include at least following:

- The ability of the stent should be consistently, accurately, and safely deployed.
- The ability of the stent to ensure effective fixation and apposition in the intended location within the vasculature.
- The ability of the stent to maintain adequate integrity.
- The consistency of the stent to dimensions and its design for compatibility for use in specified vessel diameters.
- The ability of the stent to maintain adequate flood flow through the lumen.

- The compatibility of the stent with exposure to magnetic resonance imaging (MRI) field.
- The stent should meet specified biocompatibility requirement of ISO 10993 series.
- The visibility of the stent under fluoroscopy or other technology.

It is also suggested that fatigue testing of the stents should be included in vitro testing until ten-year equivalent cycles in an appropriate test solution to simulate physiological condition.

According to the “*Non-clinical engineering tests and recommended labeling for intravascular stents and associated delivery systems*” by U.S. Food and Drug Administration (FDA) in 2010 [18], stent defects as a result of manufacturing or subsequent damage can contribute to clinical complications. One typical manufacturing flaw is the thermal damage after laser cutting process. Thermal damage such as burrs, heat affected zone (HAZ), recast layer, micro-cracks, and tensile residual stresses can detrimentally affect the performance of a stent, leading to a shorter fatigue life, decreased corrosion resistance, and even failure after insertion. Therefore, the important quality features that should be considered for high quality laser cutting stents are: (1) consistent kerf width, (2) smooth cut edge, (3) high geometrical accuracy, (4) clean cut without dross and burrs, and (5) absence of HAZ.

This paper summarizes the current state-of-art of laser cutting process on Nitinol alloys for stent applications and links the relationship between laser cutting process and the product performance. In this review, four integral topics: material (Nitinol alloys), laser cutting process, surface integrity, and performance (fatigue and corrosion) are addressed.

2.2 Nitinol Material

2.2.1 Nitinol and Nitinol History

Nitinol is a nickel-titanium alloy of near equiatomic composition. It was first discovered in the early 1960's and some of the first experimentations were conducted by the Naval Ordnance Laboratory. The public introduction of Nitinol was brought about in 1968 and thereafter a series of devices were patented in the regard of using the mechanical energy from Nitinol [19].

Nitinol are well known for their outstanding properties, namely, superelasticity, shape memory, and biocompatibility. Many of the early applications of Nitinol focused on the shape memory effect. In recent years a lot of attention has been aimed towards the superelasticity of Nitinol, with particular emphasis in biomedical applications [20]. One of the earliest Nitinol biomedical applications is orthodontic wires [21]. Intravascular stent was first introduced by Dr. Charles Dotter in 1983, who implanted stents for dog's femoral artery [22]. The first human stenting procedure was performed by Paul and Sigwart in 1986 as a scaffold [23]. By the year of 2002, Stockel et al. [14] classified over 100 different commercialized stent designs. The stent market was estimated to be near \$3 billion, and was expected to double with the advent of drug eluting devices.

2.2.2 Nitinol Properties

Nitinol exhibit unique properties i.e. superelasticity, shape memory, and biocompatibility. The basis for superelasticity and shape memory in Nitinol alloys is a temperature and/or stress induced phase transformation process (as opposed to conventional diffusion induced transformations). The reversible solid state crystalline phase transformation occurs between a

high symmetry parent phase (austenite) and a low symmetry product phase (martensite). Nitinol austenite is a B2 (cubic) type ordered structure and Nitinol martensite is a monoclinic distortion of a B19 lattice. When Nitinol is in martensite phase, it has the special ability to undergo certain amount of plastic deformation without causing slip. This process of plasticity is called twinning, which involves a shift of atoms on one side of twinning plane to form a mirror image of atoms on the other side of the twinning plane.

Guo et al. [24] summarized the stress-strain-temperature diagram (Fig. 2.3) to illustrate the superelasticity and shape memory process of Nitinol alloys based on the phase transformation process.

Superelasticity: Superelasticity means Nitinol can have a wider elastic region (up to 8%) compared to conventional materials such as stainless steel. Assuming Nitinol initially is in an austenitic state at the origin point O. With applied stress, Nitinol will be loaded along path $O \rightarrow E$, where a phase transformation from austenite to martensite and detwinning of martensite will simultaneously occur. A large elastic strain up to 8% can be achieved. Upon unloading along the path $E \rightarrow O$, the material will transform back to austenite, and the superelastic deformation will be recovered, demonstrating a hysteresis loop in the stress-strain diagram.

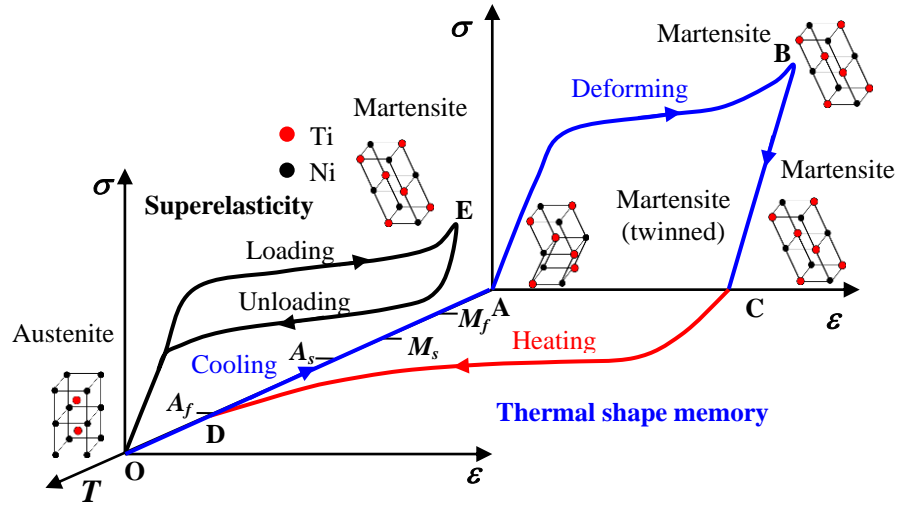


Fig. 2.3 Stress-strain-temperature diagram of Nitinol [24].

Thermal shape memory: Shape memory describes the process in which Nitinol returns to its previously defined shape when heated above the transition temperature. In the thermal shape memory part of the diagram, when Nitinol is cooled along path $O \rightarrow A$ without applied stress below martensite finish temperature (M_f), complete austenite to martensite (twinned) transformation will occur. The material is plastically deformed through reorientation and detwinning of martensite along path $A \rightarrow B$. Then, unloading from $B \rightarrow C$ will cause elastic unloading of the reoriented detwinned martensite and the material stays deformed. After heating above the austenite finish temperature (A_f), the material transforms from martensite to austenite and recovers the pseudoplastic deformation, thus “remembering” its previously defined shape.

Biocompatibility: Biocompatibility is an essential characteristic of an implant device. There are two main factors that determine the biocompatibility of a material: (a) the host reactions induced by the material and (b) the ability of the material to remain its functionality inside human body. Superior biocompatibility is one of the outstanding features that enable Nitinol to be one of the most successful implant alloys. As indicated by Stoeckel et al. [12],

Nitinol share a very similar mechanical response to biological material such as hair, tendon and bone. At body temperature, Nitinol loading and unloading curves show plateaus, along with large strains which is similar to nature materials (Fig. 2.4). Another reason why Nitinol is biocompatible in the human body is due to a uniform and homogeneous layer of TiO_2 oxide covering its surface [25]. Pérez et al. found that the thicker and more uniform the oxide layer, the longer the corrosion resistance in simulated body fluid [26]. This oxide layer also prevents Nickel, which is the major cause of allergenic contact dermatitis, from leaching out of the material and into the human body [27].

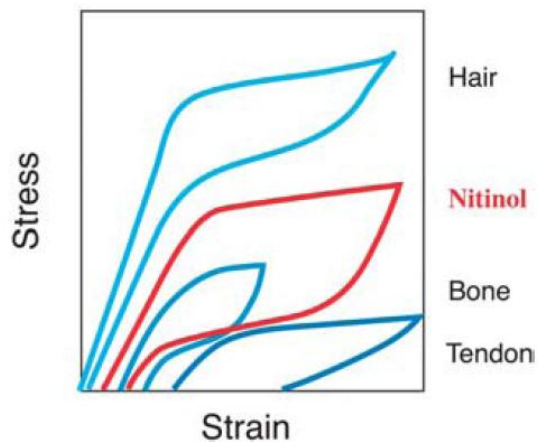


Fig. 2.4 Biomechanical compatibility of Nitinol: deformation compared with tissues [12].

2.3 Laser Cutting of Nitinol Stents

2.3.1 Laser Introduction

The term laser is short for “*Light Amplification by Stimulated Emission of Radiation*”. Stimulated emission corresponds to a process where two identical photons are generated by the impact of another photon. A laser is built based on this phenomenon. Typical components

(Fig. 2.5) of a laser are a laser active medium, a mechanism to supply energy, and an optical feedback system which achieved by a pair of mirrors on both end of the laser medium. The excited atoms or molecules are stimulated and additional photons are generated as the light circulates between the two mirrors. This process is also known as the “light amplification”. In order for the laser activatable medium to amplify light, energy needs to be provided by a pumping process. For gas lasers, the energy is typically supplied as electrical voltage. For solid state lasers, the supplied energy is usually in form of light generated by flash lamps or diodes.

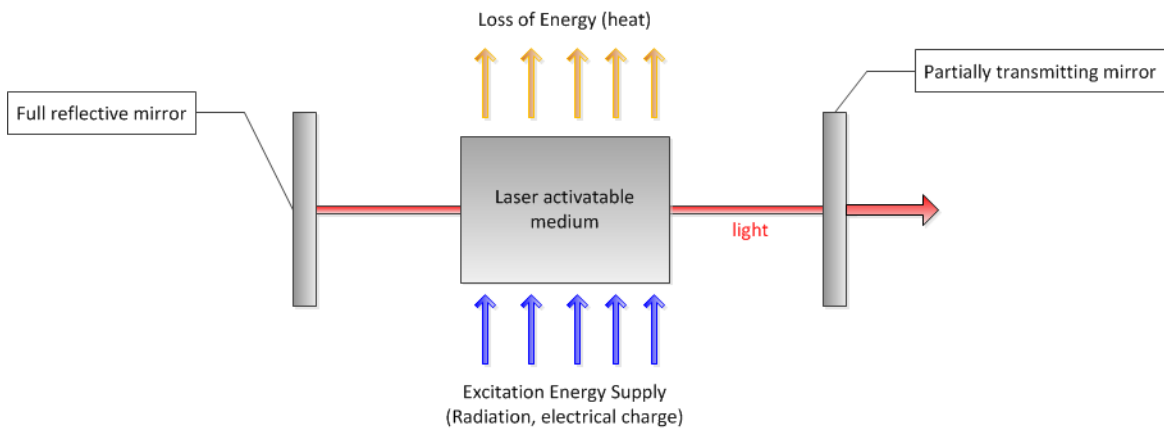


Fig. 2.5 Typical components of a laser.

2.3.2 Laser Types

Since the first laser cutting system in mid-1960s, more and more attention has been put into laser technology due to its wide range of applications and its remarkable cutting capability. Different types of lasers are used in material processing including carbon dioxide (CO₂) lasers, neodymium-doped yttrium aluminum garnet (Nd:YAG) lasers, fiber lasers, excimer lasers, and ultra-short pulse lasers [28]. For laser cutting and micromachining, CO₂, Nd:YAG, fiber, and

ultra-short pulse lasers are the most common lasers used. These lasers are discussed in the following section.

CO₂ Lasers: CO₂ laser is one of the lasers that use gas as gain medium. It is one of the most widely used industrial lasers. CO₂ lasers typically emit a wavelength of 10.64 micrometers, and it is easily absorbed by organic materials such as glass, plastics, and fabrics [29]. Most CO₂ lasers can be operated at continuous mode. Laser cutting at continuous mode generally generates a smoother surface when compared to pulsed mode [30].

Nd:YAG Lasers: Nd:YAG lasers are solid state lasers using yttrium-aluminium garnet doped with neodymium as the laser medium. It is another most widely used industrial laser. Nd:YAG lasers typically emit a wavelength of 1.064 micrometers, which is ten times smaller than CO₂ lasers. Due to the small wavelength, Nd:YAG lasers are primarily used on cutting metals [29].

Fiber lasers: A fiber laser is a variation based on the standard solid-state laser, with the gain medium being an optical fiber. The very commonly used fiber structure is dual-core structure. An undoped outer core collects the pump light and guide it along the fiber. The inner core is often doped with some rare-earth elements that are stimulated by the pump light to generate photons. Fiber laser are optically pumped. The most common pumping source is diodes. The major advantages of diode-pumped fiber lasers include: (1) a smaller size can be achieved with comparable output power due to the flexibility of the fiber, (2) the optical quality of the laser beam can be significantly improved due to remarkable light-guiding ability of fiber, and (3) the diode can have a long service life, leading to a low maintenance cost of the systems.

Ultra-short pulse lasers: The ultra-short pulse lasers are commonly refer to those have a pulse duration shorter than 10 picosecond [31]. The majority of ultrafast lasers have a pulse

regime of 100 fs to 1 ps. Due to the ultra-short laser pulses, the laser material interaction happens so fast that laser ablation occurs before thermal diffusion and transport heats up to the surrounding material. Therefore, in ultra-short pulse laser material interaction, thermal diffusion into the material is minimal, thus HAZ can be minimized. However, one of the drawbacks is that the maintenance cost is very high due to the complexity of the system.

A general comparison of lasers can be found in [Table 2.2](#).

Table 2.2 General Comparison of Different Types of Lasers [32,33]

	CO ₂ Laser	Nd:YAG Laser	Fiber Laser	Femtosecond Laser
Beam Quality M ²	Poor	Good	Excellent	Good
Industrial Experience	High	High	Moderate	Moderate
HAZ	Big	Small	Small	Not detectable
Cutting Quality	Poor	Good	Good	Excellent
Cutting Speed	High	Moderate	High	Low
Maintenance cost	Moderate	Moderate	Low	High
Acquisition Cost US \$	~15,000	~80,000	~36,000	>220,000

2.3.3 Long Pulse Lasers vs. Ultra-short Pulse Lasers

The mechanism of laser cutting is very complex due to different interactions between the laser beam and material. The basic mechanism can be summarized as a thermal heating of a melting and/or evaporating cut front ([Fig. 2.6](#)) in a narrow cut kerf as indicated by Olsen et al. [34].

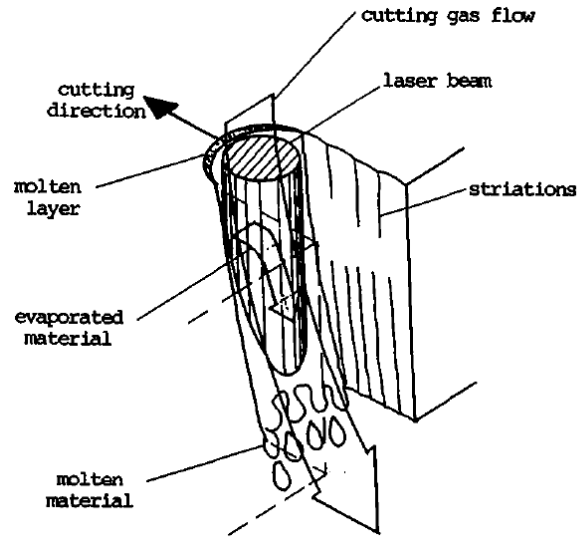


Fig. 2.6 Schematic of laser cutting front [34].

For long pulse lasers, the dominating laser cutting mechanism is fusion cutting. When material is melted by the laser and expelled from the cut kerf by a high pressure assist gas jet, the molten material is likely to re-solidify near the cutting zone, forming recast laser and dross. The excessive heat input also diffuses into the surrounding material to form a heat affected zone (HAZ).

For ultra-short pulse lasers, the femtosecond pulse duration can induce very high peak intensity. For example, a laser pulse with a pulse width of 100 fs (10^{-13} s) and a pulse energy of only one-third of 1 mJ has a peak intensity of 10^{15} W/cm² when focused to a 20 μ m diameter spot [35]. At this high intensity, the electric field is sufficiently high to induce non-linear effect, i.e. multiphoton absorption [35,36] and vaporize material within a very small amount of time. The direct phase transition of the materials to vapor state produces extremely high cut quality with smooth surfaces and clean cuts. The HAZ can be minimized since thermal diffusion time is strongly limited by the ultra-short pulse. Chichkov et al. [37] presented the comparison between

nanosecond pulse laser and femtosecond pulse laser in drilling holes on steel. Fig. 2.7 clearly shows that with pulse duration in femtosecond range, the produced cut is very smooth, with no burrs and free of deposition.

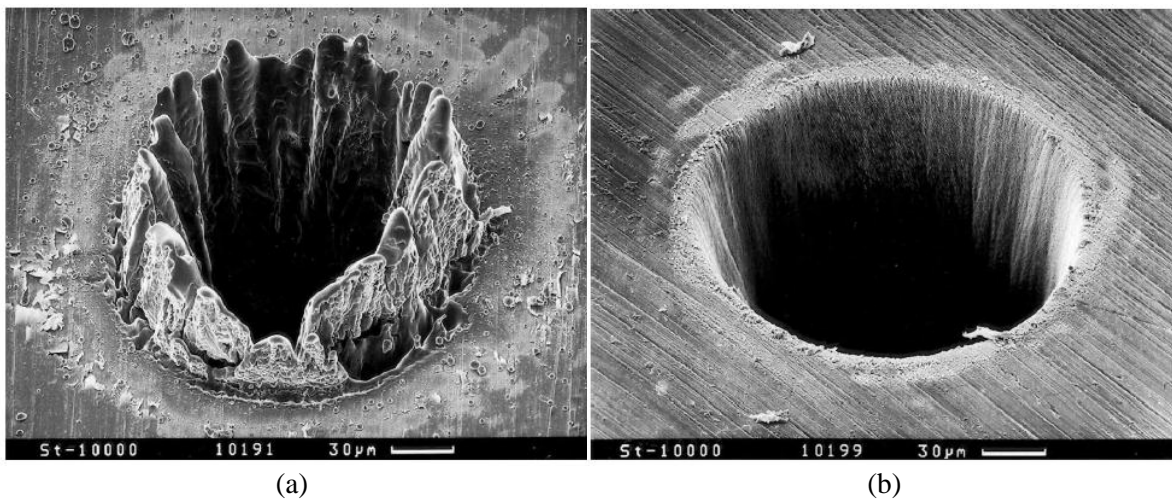


Fig. 2.7 A drilled hole on steel using pulse duration of (a) 3.3 ns and (b) 200 fs [37].

It is clear that ultra-short pulse lasers have opened new possibilities for stent manufacturing. Smaller HAZ, cleaner cut can be obtained. Moreover, these lasers have the capability to cut some materials that conventional lasers cannot cut such as transparent polymers. However, due to the low material removal rate, high acquisition cost, and high maintenance, the stent manufacturing using ultra-short pulse lasers is not yet well commercialized in industry.

2.3.4 Long Pulse Laser Processing of Nitinol

Important features such as cutting geometry, surface finish, heat affected zone (HAZ), and residual stress can be greatly affected by laser cutting process parameters. Previous researches that used long pulse lasers cut Nitinol material is reviewed in this section.

Cutting geometry: In lots of laser cutting applications, the desired cutting geometry is critical for better product performance. For instance, in stent applications, straight edges with desired taper angle will lead to uniform fluid flow in the blood vessel. Geometrical attributes that need to be considered after laser cutting are (1) kerf width (both on entry and exit), (2) taper angle, and (3) kerf deviation, etc. A typical laser cut kerf of Nitinol is shown in Fig. 2.8.

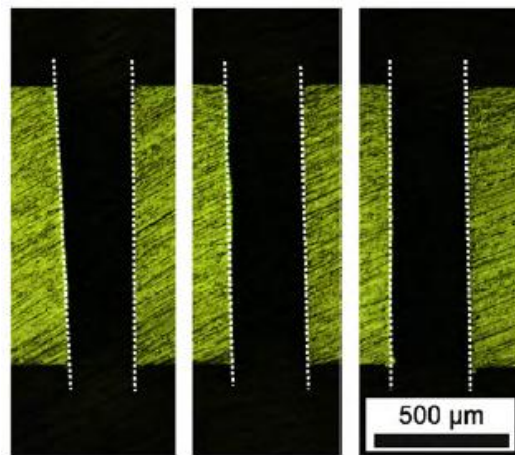


Fig. 2.8 Optical images showing laser cut kerfs of Nitinol [38].

In most cases, the top kerf width will be slightly wider than the bottom kerf, forming a taper angle. This phenomenon can be explained by several factors. For example, beam intensity losses, beam defocusing, and gas pressure losses across the material thickness [39]. For Nitinol, kerf width will generally increase with increasing pulse energy and decreasing cutting speed due to higher energy accumulation [38,40]. Increasing pulse width results in a bigger taper angle [38], and a negative laser beam offset decreases the taper angle [40].

Surface finish: Periodic lines usually appear on laser cut surfaces, also known as striations (Fig. 2.9 [41]). It affects the roughness and precision of components. Depending on whether or not assisting gas is used, the mechanisms of striation formation are different [41,42].

Striations-free cuts can be obtained by a proper selection of process parameters [43,44]. For Nitinol alloys, with assisting gas, high repetition rate produces better surface quality due to high pulse overlapping [45]. Pfeifer et al. [38] found that minimum roughness was achieved at intermediate cutting speeds of 6 to 10 mm/s and a pulse width between 0.3 and 0.5 ms when using Nd:YAG laser. Anything outside these optimal cutting parameters led to a significant roughness increase on Nitinol.

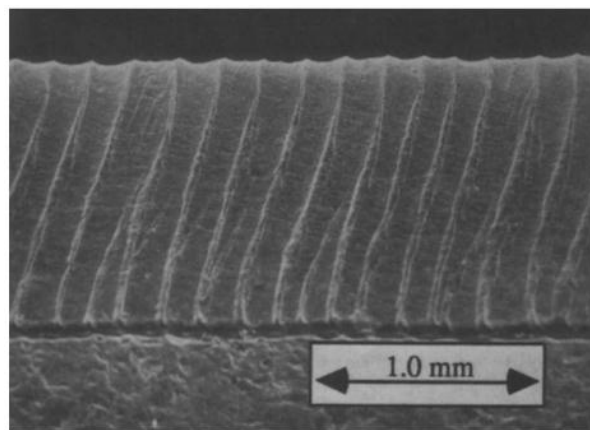


Fig. 2.9 Typical striation pattern in laser cutting in the form of periodic lines [41].

HAZ and recast layer: HAZ is the area on base material, where the microstructure and properties have been altered by the intensive heat input. The size of HAZ is a critical factor to determine the cutting quality, especially in thin medical devices that are sensitive to thermal distortions. There are multiple factors that can affect the size of HAZ, e.g., thermal diffusivity of the base material, laser power, cutting speed, and pulse width. Stournaras et al. [46] found that laser power and cutting speed were the most important parameters in determining the size of HAZ. Higher laser power combined with lower cutting speed resulted in extended HAZ due to the fact that more heat accumulated within the workpiece.

The heat generated from laser cutting alters the microstructure and microhardness. There are two common methods to measure these changes: (1) revealing the grain structure using chemical etching and (2) microhardness test on the material near and in the HAZ. However, there are limitations in both of these methods. Which one of these testing methods will reveal a better and more accurate result is still to be determined. Fig. 2.10 shows 75 μm thickness of HAZ was achieved when using Nd:YAG laser cutting Nitinol supported by both microscopic view of the cutting edge and hardness results [38].

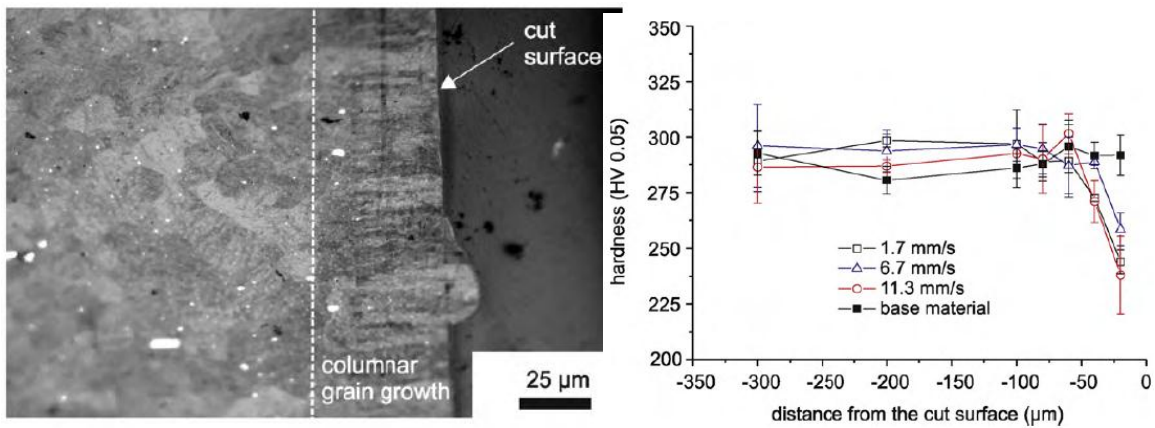


Fig. 2.10 (a) Optical image shows the microstructure around the cut surface at the speed of 6.7mm/s, (b) Hardness profile at different cutting speed. The authors used a pulsed Nd:YAG laser to cut Nitinol [38].

Recast is formed due to the re-solidification of the molten materials in the vicinity of the cut edges. This region usually reveals a higher hardness and is subjected to high stress and cracks [47]. Yilbas et al. [48] found that laser parameters such as pulse energy, pulse width, and pulse frequency can effectively control recast layer formation. Also, a vaporization dominated laser cutting process can suppress the formation of recast layer [49].

Residual stress: Residual stress is the stress that remains in the bulk material after the removal of external force or thermal gradient. Based on the mechanical nature of residual stress, it can be categorized as compressive or tensile residual stress. The compressive residual stress is known to hinder the formation and growth of the cracks and thus, is beneficial for fatigue performance. Tönshoff et al. [50] theoretically compared the thermal stresses from laser cutting ceramics using CO₂, Nd:YAG, and excimer lasers. It was found that thermal induced stresses can be reduced by a short laser pulse with high beam intensity. Amer et al. [51] found that high tensile stresses, up to 0.8 GPa, were induced in laser machining silicon wafers.

There is no literature on measuring residual stress of Nitinol after laser cutting. Due to the fact that Nitinol may go through a phase transformation after heating, the mechanism for residual stress generation will be very complex. Hence, further experimental as well as theoretical work is needed to better understand the residual stress formation and distribution of Nitinol by laser cutting.

2.3.5 Advantages/Disadvantages for Long Pulse Lasers

Modern laser cutting machines that used long pulse lasers and equipped with a CNC motion control system can offer high speed, high accuracy, and the capability for flexibility. Drawbacks are the occurrences of thermal damages such as burrs, HAZ, micro-cracks, and high tensile residual stress [52]. Post-processes are therefore needed to remove these annoyances to enhance product performance. Processes such as pickling, annealing, and electropolishing are very effective in removing burrs, micro-cracks, and HAZ to produce a very smooth surface [53]. [Fig. 2.11](#) shows the progress on surface finish of these post-processes.

Post-processes are essential for better quality of final products. However, we need to be conservative when using the post-processes due to the fact that (1) they are high cost and time consuming, (2) most of the post-processing procedures involves the use of hazardous chemicals, and thus can potentially contaminate the final product, and (3) they can detrimentally affect the final products, even failure of the component. For example, James et al. [54] reported several cases where stent structure failed after ultrasonic cleaning process. He stated that under certain ultrasonic frequency, resonance may occur, leading to the fatigue damage of a cleaned sample. Geller et al. [55] found that acid pickling and electropolishing descaled stent strut width of 30%. The reduction of strut width can lead to decreased stent strength.

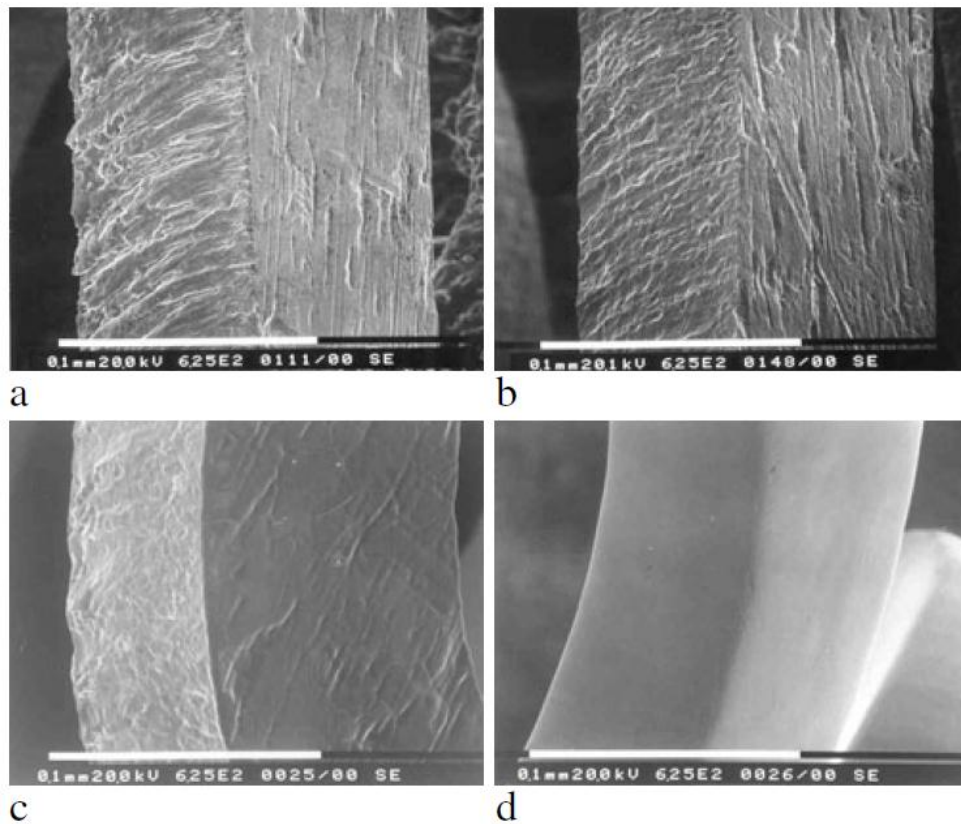


Fig. 2.11 Stent for (a) as cut, (b) pickled, (c) annealed, and (d) electropolished [56].

If burr formation, recast layer deposition, HAZ, and micro-cracks formation can be minimized after laser cutting, then some post-processes can be eliminated, cost and time can also be significantly reduced, leading to a decrease in economic, social, and environmental burden. One way to achieve aforementioned goals is the use of ultra-short pulse laser to achieve the “cold machining” [57]. Some previous ultra-short pulse laser micromachining experiments on Nitinol and results are reviewed in the following section.

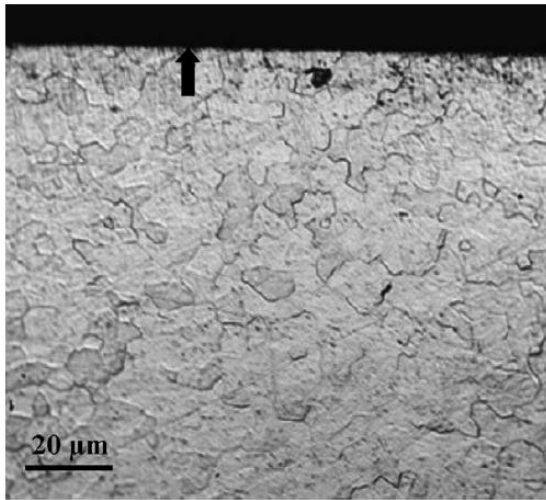
2.3.6 Ultra-short Pulse Laser Processing of Nitinol

The progress in ultra-short pulse laser technique through the development of chirped-pulse amplification [58] has made available ultra-short pulse laser systems for micro-cutting and drilling. In ultra-short pulse machining, the ablation occurs mainly in vapor phases. The absorbed laser energy is first deposited into the thermal energy of electrons (which are well above evaporation threshold). Then the thermal energy is transferred to the lattice in a picosecond time scale. Thermal diffusion into the material is minimal, leading to an insignificant amount of liquid phase, absence of which allows a better control of the machining process [59]. Due to the non-traditional laser-material interaction between ultra-short pulse laser and the workpiece, the characteristics of cutting geometry, surface roughness, HAZ, recast layer, and residual stress will be different.

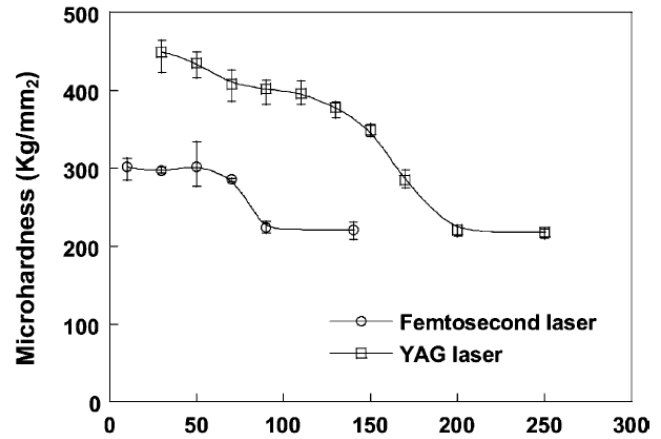
Cutting geometry: It was found that the focal position has a significant influence on the kerf geometry when using femtosecond laser to process Nitinol. When the laser beam was exactly focused on the top surface, the minimal kerf width, maximal depth of cut and minimal kerf angle was obtained [60]. High aspect ratio up to 60 was also achieved in the study.

Surface roughness: Smallest surface roughness of 0.2 μm was achieved by Huang et al. [59], when using small beam power and intermediate beam spacing. The achieved roughness by a 150 fs laser is very close to those using milling with certain feed rate and EDMed sample with finish trim cut [24]. Zheng et al. [60] found the roughness range of Nitinol after femtosecond machining was 2 – 5 μm when changing output power and overlap. This high roughness might be attributed to the fact that multiple passes are need to cut through the sample.

HAZ and recast layer: Huang et al. [59] compared the hardness of Nitinol using femtosecond laser and Nd:YAG laser. It was found that the hardened layer is 70 μm thick when using femtosecond layer, while the hardened layer is 170 μm when using Nd:YAG laser (Fig. 2.12). Also, the recast layer is found to be 7 μm using femtosecond laser and it was much less than EDMed Nitinol samples that have a recast layer of 20 μm [61]. Zheng et al. [60] found no microstructure change at the kerf edges. It was stated that the minimization of the HAZ was due to the negligible thermal diffusion. Also, no recast layer and micro-cracks were found in the study.



(a)



(b)

Fig. 2.12 (a) An optical micrograph shows the microstructure under the machined surface (arrow), (b) Microhardness at various depths from the machined surfaces (as compared to Nd:YAG laser). The authors used 150 fs femtosecond laser to process Nitinol [59].

Residual stress: Amer et al. [62] compared induced stresses by femtosecond lasers to nanosecond lasers in silicon wafers as shown in Fig. 2.13. It was concluded that with ultrashort pulse lasers, the thermal induced tensile residual stress could be reduced since there was a minimal thermal impact on the workpiece.

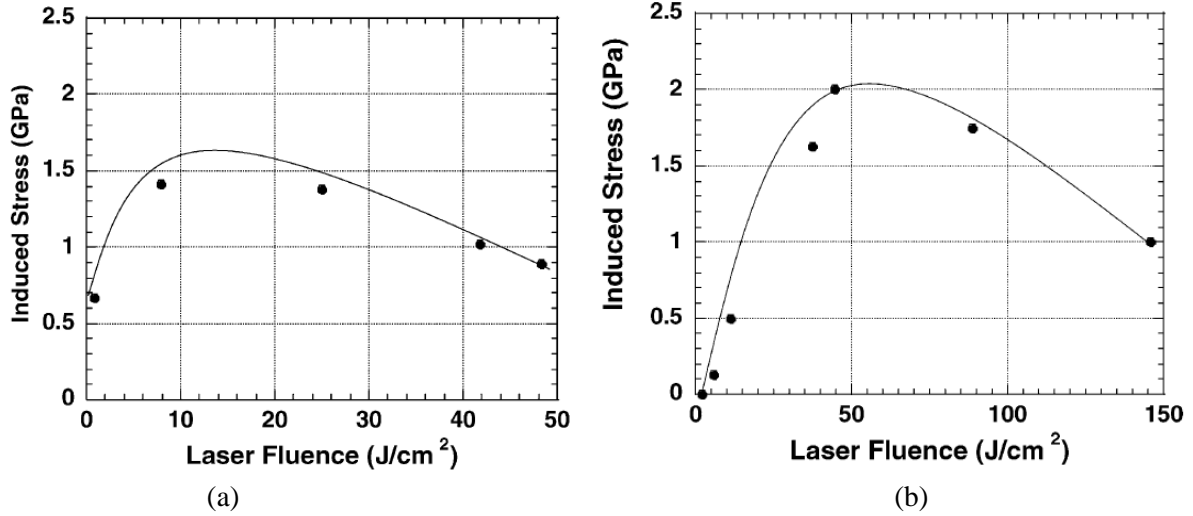


Fig. 2.13 Average induced stress as a function of laser fluence for (a) femtosecond laser (b) nanosecond laser.

2.3.7 Advantages/Disadvantages for Ultra-short Pulse Lasers

The advantages of using ultra-short pulse lasers are very obvious. The vaporization dominated process has very high precision and very small amount of recast and debris. Also, the ultra-short pulse duration leads to a very short thermal diffusion time, and thus, the HAZ, tensile residual stress, and micro-cracks can be eliminated. However, the major drawbacks of using ultra-short pulse lasers are the very high maintenance cost as well as the low material removal rate (MRR) as a result of low average power.

Li et al. [63] found that with highest laser fluence of 100 J/cm² and lowest scanning speed of 10 mm/min, the maximum material removal rate was 50 μm/scan. This indicates that even for small applications such as coronary stents that has a wall thickness of 150 μm, multiple passes are needed in order to get a throughout cut. The need for multiple passes will significantly increase the complexity and the time of the manufacturing process. Thus, in order to meet the industrial yield, future customization between laser types and process characteristics is required.

One example of the customizations is the use of water in laser cutting process. In this work, this process is called “wet” laser cutting.

2.4 Water-assisted Laser Cutting of Nitinol

2.4.1 Process Concept

The idea of using water in laser processing has been studied since 1970. Steam cleaning, shock processing, and water-assisted laser ablation technique have been developed. For cutting applications, the use of water relies on the physical phenomena that include [64]:

- Light transportation within a waterjet
- Water convection/explosive evaporation carries debris away
- More effective cooling of workpiece and ejected material
- Reduced atmospheric pollution by waste gases and aerosols

2.4.2 Experimental Setup

The common experimental setups are summarized in Fig. 2.14.

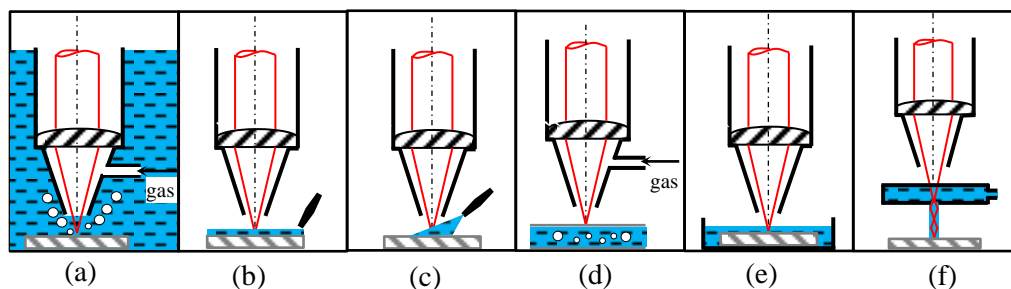


Fig. 2.14 Schemes of water-assisted laser cutting process, literature sources (a) [65], (b) [66], (c) [67], (d) [68], (e) [69], and (f) [70].

2.4.3 Surface Integrity Improvement

It has been proved that water-assisted laser cutting can effectively reduce the HAZ and dross due to cooling and ejecting effect of water. Early researches used under water Nd:YAG laser to cut 304L stainless steel for nuclear applications. A narrower and more regular kerf and less sedimented dross was found [65]. Other trials that used a thin layer (1 mm) of water film [66], and a water steam spray [67] were performed. The main reason to add water in these laser cutting processes is the elimination of debris redeposition near machined area due to the convection of water and bubble-induced motion.

For stent applications, 3 types of water-assisted laser machining can be found in literatures, see [Fig. 2.14\(d\)](#), [\(e\)](#), and [\(f\)](#). Muhammad et al. [68] proposed “wet” stent machining with the presence of N₂ assist gas and continuous water flow through the inner part of the tube along the tube axis. It was found that wet cutting resulted in narrower kerf width, lower surface roughness, less dross, absence of backwall damage ([Fig. 2.15](#)), and a smaller HAZ. Underwater femtosecond laser cutting was proposed by Muhammad et al. [69], the nitinol sample was placed 1 mm under water in Petri dish. It was showed that only 2% of laser power was absorbed by water, allowing 98% of laser power to reach the target. The results showed that femtosecond laser cutting in air still resulted in recast, debris, and HAZ. However, underwater cutting is a debris-free, recast-free process with no HAZ and backwall damage, see [Fig 2.16](#).

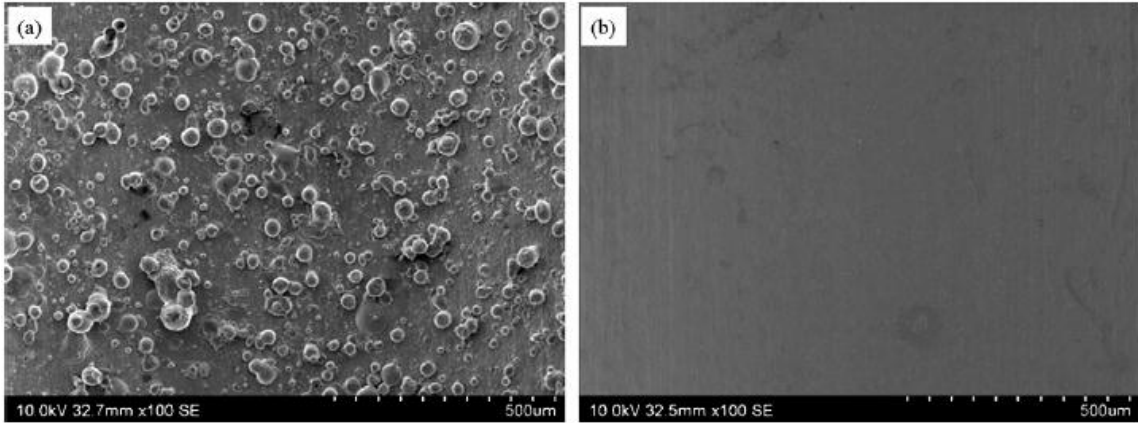


Fig. 2.15 SEM images of the back wall: (a) dry cutting and (b) wet cutting [68].

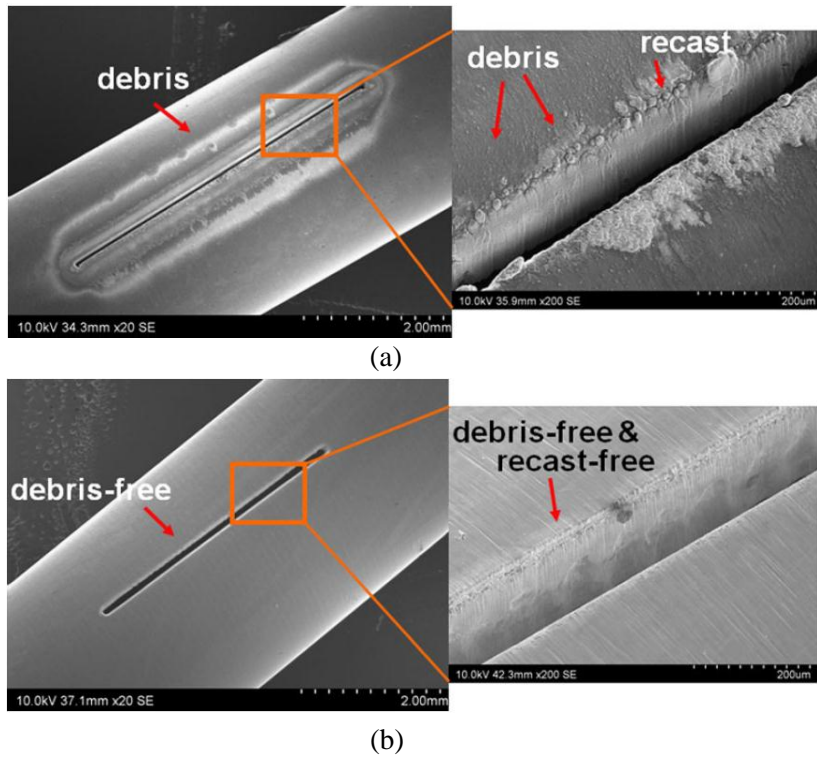


Fig. 2.16 (a) Dry cutting showing debris and recast, (b) underwater cutting is debris-free and recast free result [69].

A very distinctive water-guided laser cutting scheme was reported in [70,71,72,73,74,75]. The process employs a laser beam which is completely reflected at the air-water interface in a water jet, where the beam can be guided over a distance up to 10 cm, permitting production of parallel high aspect ratio cut kerfs. No focusing or distance control is required. The process concept can be found in Fig. 2.14(e). The water jet cools the cut area and eliminates any heat effects such as HAZ and micro-cracks. The water jet also removes the ablated material from the cut so that contamination can be reduced and accuracy can be increased. Hock et al. [75] did a comparative study using fiber laser and water-jet guided laser cutting of thin metal sheets. It was concluded that dross-free cuts with almost no HAZ and small kerf width was sustained by water-jet guided laser cutting process, whereas small dross, notable HAZ, and varying kerf width is observed for fiber laser cutting (Fig. 2.17). However, process time for water-guided process is considerably higher than those for fiber laser cutting. A commercial water-assisted laser cutting machine has been developed by Synova S.A.

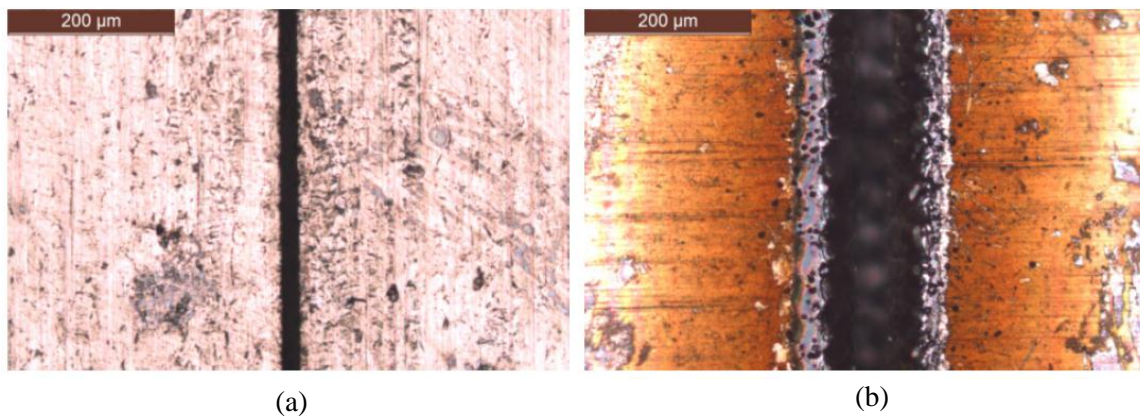


Fig. 2.17 Cut in 50 μm stainless steel sheet with (a) water-jet guided laser system and (b) remote laser system. Please note the identical scale of these microscope images [75].

2.5 Surface Integrity on Fatigue

2.5.1 FDA Requirement

There is a special emphasis on the fatigue and durability of the stents by the aforementioned ISO standard. It is suggested that long-term durability under anticipated physiological conditions shall be performed. More specifically, the fatigue testing of the stent should include in vitro testing until ten-year equivalent cycles in an appropriate test solution to simulate physiological condition. Food and Drug Administration also requires 400 million cycles (10 years) before failure for an intravascular stent.

2.5.2 Fatigue Testing Methods

It is of great importance to understand the in vivo loading condition after the stents are inserted inside human body. If a similar loading condition can be designed in fatigue testing, a more accurate fatigue life can be predicted and the fatigue performance of the stents can be better understood.

In vivo situations, stents are submitted to irregular cyclic loading against flexible tissues and “single-event” overloads. Recent studies have shown that arteries, particularly the superficial femoral artery (SFA), experience a dynamic combination of axial compression and extension, radial compression, bending, and torsion [76,77,78,79,80]. In particular, three-dimensional magnetic resonance imaging (MRI) of the SFA has revealed that this artery undergoes significant twisting of $60^\circ \pm 34^\circ$ when the hip and knee are flexed under simulated walking conditions [76,79]. Also, due to the unique mechanical behavior and phase transformation under applied stress and temperature variations, the fatigue mechanism in Nitinol alloys is quite different. Duerig et al. [20] and Morgan [81] stated that Nitinol alloys present a high strength against low-

cycle fatigue with strain control, whereas do not perform well in high-cycle stress controlled fatigue.

There are generally three basic approaches to evaluate the fatigue behavior of Nitinol. The traditional way is to monitor the total life of a specimen as a function of applied stress (stress control). A second way for fatigue analysis is to control the deformation per cycle in fatigue testing. This is referred to as the strain-life method. The third approach to fatigue assessment is the “damage tolerance” test based on fracture mechanics. Pre-existing cracks are designed and the growth of the crack is considered as a function of number of cycles and applied stress.

It is a well-known rule of thumb that strain based fatigue test is preferred over stress based fatigue test on Nitinol alloys. It is because the monotonic stress-strain curve shows that global strain is continuous whereas stress tends to ‘plateau’ due to the detwinning mechanism in martensite or due to stress induced martensitic transformation in superelastic material. Therefore, the stress is constant over a wide range of strains. This makes stress based test conditions less certain than strain based. Furthermore, displacement controlled testing requires less sophisticated equipment than load controlled testing.

Another characteristic of Nitinol fatigue is that unlike most conventional metallic materials, the amplitude of the alternating strain in Nitinol has a much more significant effect on the fatigue life than the applied mean strain.

A very comprehensive review that focused on giving a more universal understanding of the inherent fatigue and fracture resistance of Nitinol for biomedical applications can be found in [82]. The total life fatigue testing of Nitinol alloys developed over time, it starts with “stress-life” test using standard uniaxial tension-compression on dogbone specimen. Varying conditions such as material composition, testing temperature, microstructure would lead to significant change in

the fatigue limits. The testing methods then gradually evolve to “strain-life” due to the uniqueness of the stress-strain behavior of the material. Rotating bending test on Nitinol wires was widely used as the fatigue testing method. It is a convenient way to collect strain based fatigue data. The strain amplitude is calculated by the ratio of the wire diameter to the curvature diameter, so a range of strain amplitudes can be achieved for a given wire diameter with slight adjustments in the curvature. Later on, the subcomponents of stent are tested, the processing sequence of the specimens are exactly as the medical device. These specimens therefore can reflect the actual material condition of the devices. Multiaxial fatigue test can reveal a more accurate fatigue behavior of Nitinol medical devices under complex in vivo loading, e.g. partially reversible and fully reversible torsional load. Also, commercially available fatigue test machine nowadays can perform even more complex simulated biological loading conditions. The supplementary information can be found in [Table 2.3](#).

Table 2.3 Common Fatigue Testing Sample Forms, Testing Method, and Key Findings

Form	Test method	Key findings	Ref.
Dogbone	Tension-compression	10^7 cycles fatigue was found to decrease with increasing M_s . 1000 cycles were obtained at strain amplitude of 10%, where conventional engineering materials sustain only strain amplitude of 1%.	[83]
Dogbone	Tension-tension	10^6 cycles fatigue limit increased with increasing test temperature	[84]
Wire	Bending-rotation	Low cycle fatigue data conform to the Coffin-Mason law. Nitinol presents a high strength against low-cycle fatigue with strain control, whereas do not perform well in high-cycle stress controlled fatigue.	[85,8 6,87,8 8,89,9 0,91,9 2]
Diamond-shaped stent subcomponent	Stent pulsatile fatigue test	Non-traditional constant life diagrams were constructed. Increase in volume fraction of stress-induced martensite resulted in a greater tolerance of strain amplitude.	[93,9 4]
Shaft	Partly and fully reversed torsion	Functional property damping capacity evolves with cycle numbers and test frequency.	[95]
Tube	Fully reversed torsion	Modified Coffin-Manson equation was proposed for multiaxial fatigue.	[96]

2.5.3 Fatigue Crack Growth Behavior

There are many factors that need to be considered when evaluating the fatigue crack growth behavior of Nitinol. Crystallographic orientations i.e. superelastic austenite, stable austenite, thermal martensite, and mixed phase are critical when considering the fatigue crack growth behavior. Robertson et al. [82] concluded that Nitinol with martensite microstructure have the best crack growth resistance, while superelastic austenite Nitinol have worst resistance as shown in Fig. 2.18.

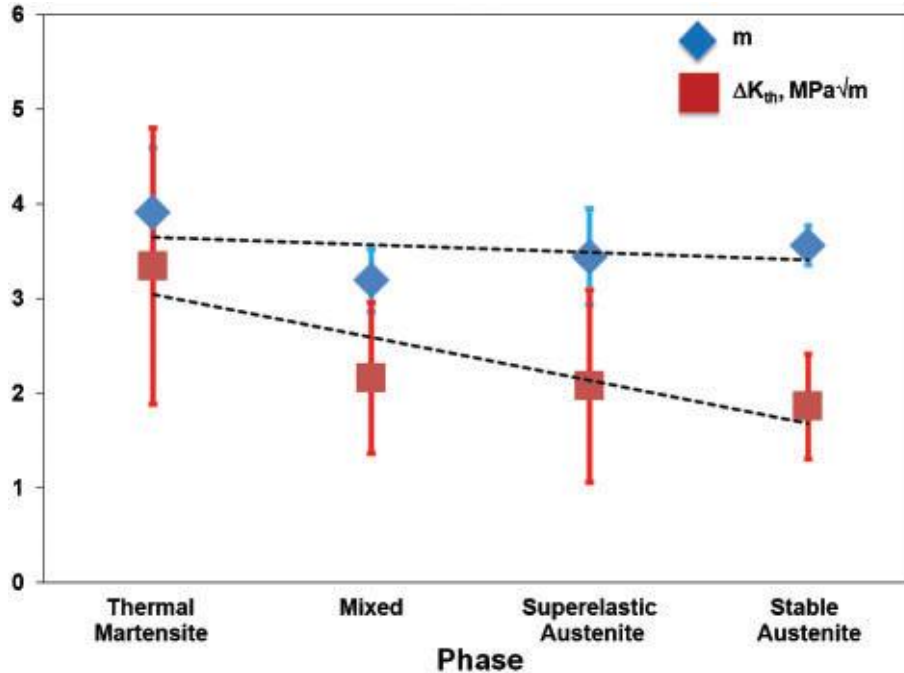


Fig. 2.18 Crack growth parameters (Paris exponent m and fatigue threshold ΔK_{th}) for Nitinol as a function of R ratio. As expected, the threshold values decrease with increasing R ratio. Data are presented as mean \pm one standard deviation [82].

The inclusions that present in Nitinol have not been very widely studied, but it is an integral part of the study of crack initiation, propagation, fatigue, and biocompatibility. Particulates in Nitinol products are often associated with the non-purity of the ways in which the Nitinol is produced, namely vacuum arc and induction melting. Shabalovskaya et al. [97] studied inclusions in superelastic and shape memory Nitinol (50.8 at.% Ni) rods. An auger spectrum of the inclusion showed the nominal composition of the TiO_2 particle. It is observed that in commercially available material, certain particles, or strings of particles exceeded the sizes and concentrations considered acceptable by ASTM standard F2063-05 (39 μm inclusion size, and 2.8 area percent including porosity created by particles). This is exceptionally bad since Nitinol products are being made smaller and smaller, even down to a comparable size with such particulates.

Robertson and co-workers [98] provided a comprehensive characterization of the in vitro fatigue–crack growth properties and fracture toughness behavior in thin-walled Nitinol tubing typically used in commercial stent manufacturing in simulated physiological environment, in order to realize quantifiable engineering parameters for designing against premature failure from overload and/or in vivo fatigue damage in endovascular self-expanding stents. It was concluded that load ratio and test frequency played an important role in the fatigue-crack growth behavior.

2.5.4 Effect of Surface Integrity on Fatigue

For conventional metallic materials, it has been found that surface conditions significantly affect the fatigue performance [99,100]. Laser induced thermal damages such as recast layer, micro-cracks, and tensile residual stresses are very likely to detrimentally affect Nitinol fatigue performance. However, based on a literature survey, the effect of surface integrity on the fatigue performance of Nitinol devices has not been well studied, and the relationship between process parameters, surface integrity, and product functionality is simply not established.

A research done by Chan et al. [101] revealed that after laser welding, the defects at weld zones were most susceptible sites for crack nucleation. As a result, the fatigue life for weldments were shorter than unwelded samples (Fig. 2.19). The hypothesis is that laser cut Nitinol samples will show the similar trend and future studies are needed to confirm this hypothesis.

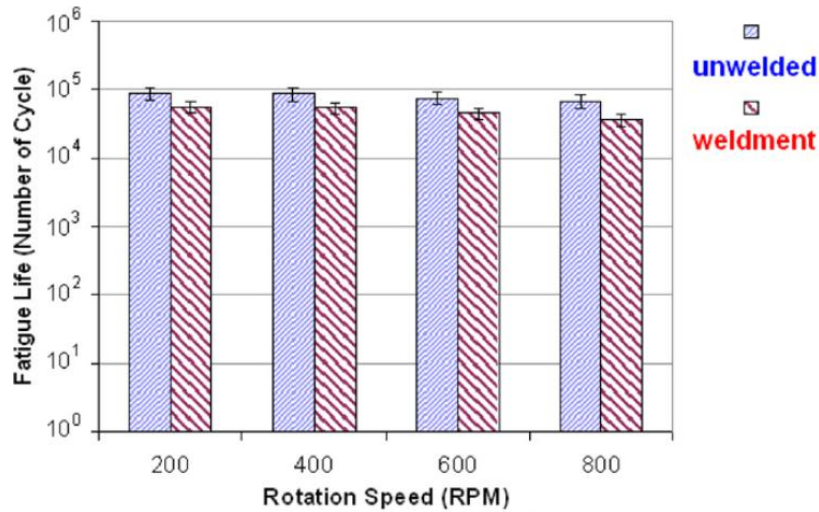


Fig. 2.19 Fatigue life for the unwelded sample and weldment at different rotational speed [101].

2.6 Surface Integrity on Corrosion

Nitinol alloys, recognized as implantable materials, the biocompatibility must be demonstrably superior. More specifically, it must be nontoxic, noncarcinogenic, chemically and physically stable, and corrosion resistant so that it causes appreciably little or no foreign body reaction.

The corrosive environment inside human body will gradually degrade the implants. One of the major clinical consequences of such corroding implants is the release of solutes, i.e. the corrosion products, may lead to histological changes in the local tissue by either direct toxic effects or a local hypersensitive reaction [102]. For Nitinol alloys, one of the major elements, nickel, is a well-known allergen, which will detrimentally affects skin, causes dermatitis [103]. A recent report demonstrated that the highest Ni ion release over a 25-day immersion period was found to be 0.002 $\mu\text{g}/\text{day}$. This Ni level is negligible compared with the daily intake of Ni in ordinary diet [104].

One of the earliest researches trying to understand Nitinol in vivo corrosion behavior was done by Castleman et al. [105], it was found that after 17 months implantation in dogs, there were no signs of either generalized or localized corrosion. It was well accepted that the corrosion behavior of Nitinol is much closer to Ti than to Ni due to the fact that the passive oxide film formed on Nitinol is similar to that of titanium [106]. Another research showed that the passive layer, even after being mechanically damaged by handling, fretting or fatigue fracture, will continuously grow in thickness and become comparable in corrosion resistance to non-damaged electrochemically polished samples [107]. The most desirable and stable oxide is Ti based TiO_2 film, which is beneficial for Nitinol biocompatibility. On the contrary, the Ni based oxide layer is non-stable and soluble, which is detrimental to Nitinol biocompatibility [108].

Such passive layer can be prepared via various techniques including oxidization in air/water/steam and chemically/electrochemically passivation. Surface parameters i.e. elemental/oxide composition, crystalline/amorphous character [109], heterogeneity, wettability are very import to determine Nitinol corrosion resistance and biological performance [108].

Powder immersion reaction assisted coating (PIRAC) was found to considerable improve corrosion behavior of Nitinol alloy in terms of pitting corrosion and exceeding low metal ion release rate as compared to untreated samples [110]. Low-temperature plasma coating was applied to Nitinol, and it was found that plasma-treated Nitinol alloys revealed increased surface hydrophilicity and enhanced anticoagulation property [111].

Different surface treatment processes such as mechanical polishing, electropolishing have significant influence on the corrosion performance of Nitinol alloys [104,112,113]. It was concluded by Cisse et al. [104] that electropolishing followed by chemical passivation led to the lowest corrosion rate when compared to other surface treated methods, namely mechanical

polishing. Also, electropolished surface revealed zero pitting corrosion. The Ni release rate after electropolishing was also negligible. Wever et al. [114] and Balakrishnan et al. [115] confirmed these results both in vitro and in vivo, respectively. A detailed comparison of corrosion behavior for various Nitinol surfaces can be found in Fig. 2.20 [116].

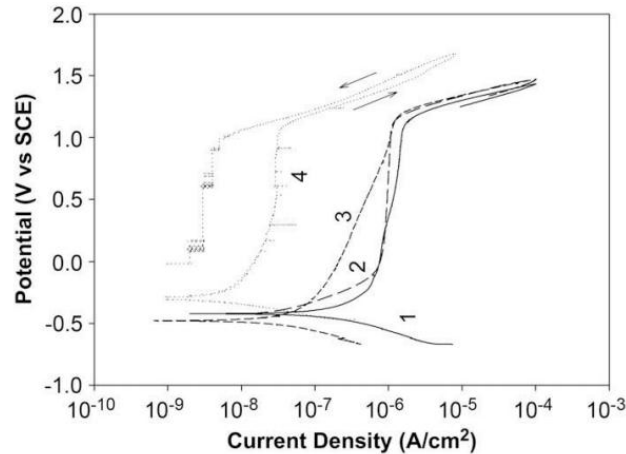


Fig. 2.20 Potentiodynamic cyclic polarization for Nitinol disc samples. (1) Mechanically polished (Mp), (2) chemically etched (Ce), (3) electropolished (Ep), (4) chemically etched, boiled in water and heat treated (CeWbHt) samples [116].

To conclude, even though bare Nitinol surfaces are still prone to corrosion, electropolishing, as a simple but powerful way, can offer the best corrosion resistance, and can improve Nitinol surface used for implantation. Therefore, it can be inferred that electropolishing is still an essential post-process after laser cutting for Nitinol in cardiovascular applications.

2.7 Pressing Issues/Challenges

Nitinol is widely used in cardiovascular stents and these devices are often made by laser cutting. The pressing problems in laser cutting Nitinol are summarized as follows:

- Conventional dry laser cutting is a high-temperature process which generates a heat-affected zone (HAZ) that modifies the surface and near-surface microstructure and properties. This is a particular disadvantage in biomedical stents where a white/recast layer can form that contains a modified microstructure, oxidation, microcracks, and tensile residual stress. This thermal damage and ablation-induced contamination would be very detrimental to fatigue performance of Nitinol stents machined by dry laser cutting, which is a major concern for stent manufacturer.
- Phase transformation (austenite-martensite) temperatures of Nitinol are very low (-100°C – 100°C). The laser-induced thermal loading and Nitinol's unique properties couple where recovery, recrystallization, and phase transformation are prevalent. As a result, surface integrity becomes a major concern. Yet, little research has been done in elucidating the mechanism of surface integrity which is critical for stents.
- Even though laser cutting with ultra-short pulse lasers and water-assisted lasers has proven to be effective in reducing the thermal damage, it is still lack of industrial practice due to high cost and complexity of the systems. In addition, comprehensive experimental study to determine the influence of critical process parameters on surface integrity (surface finish, edge quality, microstructure, residual stress, micro/nano-hardness, and chemical compositions) in “wet” laser cutting is yet to be done.
- Furthermore, the basic science underlying the intrinsic laser cutting-property-functionality relationship has yet to be understood.

2.8 References

- [1] H.J. Chun, E.S. Kim, J.J. Hyun, Y.D. Kwon, B. Keum, C.D. Kim, 2010, Gastrointestinal and biliary stents, *Journal of Gastroenterology and Hepatology*, 25(2): 234-243.
- [2] S.S. Lobodzinski, 2008, Bioabsorbable coronary stents, *Cardiology Journal*, 15(6): 569-571.
- [3] J.A. Ormiston, P.W. Serruys, 2009, Bioabsorbable coronary stents, *Circulation: Cardiovascular Interventions*, 2(3): 255-260.
- [4] A. Schuesseler, 2007, Manufacturing of stents: Optimize the stent with new manufacturing technologies, *New technologies in vascular biomaterials: fundamentals about stent II*, : 93-106.
- [5] H. Tamai, K. Igaki, E. Kyo, K. Kosuga, A. Kawashima, S. Matsui, H. Komori, T. Tsuji, S. Motohara, H. Uehata, 2000, Initial and 6-month results of biodegradable poly-L-lactic acid coronary stents in humans, *Circulation*, 102(4): 399-404.
- [6] C. Di Mario, H. Griffiths, O. Goktekin, N. Peeters, J. Verbist, M. Bosiers, K. Deloose, B. Heublein, R. ROHDE, V. Kasese, 2004, Drug-Eluting bioabsorbable magnesium stent, *Journal of Interventional Cardiology*, 17(6): 391-395.
- [7] S. Garg, P.W. Serruys, 2010, Coronary stents- looking forward, 56(10): 43-78.
- [8] T. Isotalo, J. Nuutinen, A. Vaajanen, P.M. Martikainen, M. Laurila, P. Törmä, M. Talja, T.L.J. Tammela, 2005, Biocompatibility and implantation properties of 2 differently braided, biodegradable, self-reinforced polylactic acid urethral stents: An experimental study in the rabbit, *The Journal of Urology*, 174(6): 2401-2404.
- [9] A. Raval, A. Choubey, C. Engineer, D. Kothwala, 2004, Development and assessment of 316LVM cardiovascular stents, *Materials Science and Engineering: A*, 386(1-2): 331-343.
- [10] Y.K. Chen, V. Jakribettu, E.W. Springer, R.J. Shah, J. Penberthy, S.R. Nash, 2006, Safety and efficacy of argon plasma coagulation trimming of malpositioned and migrated biliary metal stents: A controlled study in the porcine model, *The American Journal of Gastroenterology*, 101(9): 2025-2030.
- [11] S.A. Shabalovskaya, 1996, On the nature of the biocompatibility and on medical applications of NiTi shape memory and superelastic alloys, *Biomedical Materials and Engineering*, 6(4): 267-289.
- [12] D. Stoeckel, A. Pelton, T. Duerig, 2004, Self-expanding nitinol stents: Material and design considerations, *European Radiology*, 14(2): 292-301.

- [13] T. Duerig, 2002, The use of superelasticity in modern medicine, *MRS Bulletin-Materials Research Society*, 27(2): 101-104.
- [14] D. Stoeckel, C. Bonsignore, S. Duda, 2002, A survey of stent designs, *Minimally Invasive Therapy & Allied Technologies*, 11(4): 137-147.
- [15] Y.P. Kathuria, 2005, Laser microprocessing of metallic stent for medical therapy, *Journal of Materials Processing Technology*, 170(3): 545-550.
- [16] Z. Lin, A. Denison. 2004, *Medical Device Materials: Proceedings from the Materials & Processes for Medical Devices Conference 2003, 8-10 September 2003, Anaheim, California*, 205.
- [17] ISO-25539-2. 2008. Cardiovascular implants - endovascular devices - part 2: Vascular stents.
- [18] U.S. Food and Drug Administration. 2010. Non-clinical engineering tests and recommended labeling for intravascular stents and associated delivery systems.
- [19] F.E. Wang, 1986, Nitinol, a “memory “alloy in action, *Metallography*, 19(2): 257-259.
- [20] T. Duerig, A. Pelton, D. Stöckel, 1999, An overview of nitinol medical applications, *Materials Science and Engineering: A*, 273: 149-160.
- [21] G.F. Andreasen, T.B. Hilleman, 1971, An evaluation of 55 cobalt substituted nitinol wire for use in orthodontics, *The Journal of the American Dental Association*, 82(6): 1373-1375.
- [22] C.T. Dotter, R. Buschmann, M.K. McKinney, J. Rösch, 1983, Transluminal expandable nitinol coil stent grafting: Preliminary report. *Radiology*, 147(1): 259-260.
- [23] P.W. Serruys, M.J. Kutryk, A.T. Ong, 2006, Coronary-artery stents, *New England Journal of Medicine*, 354(5): 483-495.
- [24] Y. Guo, A. Klink, C. Fu, J. Snyder, 2013, Machinability and surface integrity of nitinol shape memory alloy, *CIRP Annals - Manufacturing Technology*, 62(1): 83-86.
- [25] N. Figueira, T. Silva, M. Carmezim, J. Fernandes, 2009, Corrosion behaviour of NiTi alloy, *Electrochimica Acta*, 54(3): 921-926.
- [26] L.M. Pérez, L. Gracia-Villa, J.A. Puértolas, M. Arruebo, S. Irusta, J. Santamaría, 2009, Effect of nitinol surface treatments on its physico-chemical properties, *Journal of Biomedical Materials Research Part B: Applied Biomaterials*, 91B(1): 337-347.
- [27] N. Morgan, 2004, Medical shape memory alloy applications—the market and its products, *Materials Science and Engineering: A*, 378(1): 16-23.

- [28] Steen WM. 1998. Laser material processing. London: Springer Verlag.
- [29] Ready JF. 1997. Industrial applications of lasers. Access Online via Elsevier.
- [30] G. Chryssolouris, 1991, Laser machining-theory and practice.
- [31] J. Meijer, K. Du, A. Gillner, D. Hoffmann, V.S. Kovalenko, T. Masuzawa, A. Ostendorf, R. Poprawe, W. Schulz, 2002, Laser machining by short and ultrashort pulses, state of the art and new opportunities in the age of the photons, CIRP Annals - Manufacturing Technology, 51(2): 531-550.
- [32] X. Chen, X. Liu, 1999, Short pulsed laser machining: How short is short enough? Journal of laser applications, 11: 268.
- [33] Luxon JT, Parker DE, Plotkowski PD. 1987. Lasers in manufacturing: An introduction to the technology. IFS.
- [34] F.O. Olsen, L. Alting, 1989, Cutting front formation in laser cutting, CIRP Annals-Manufacturing Technology, 38(1): 215-218.
- [35] X. Liu, D. Du, G. Mourou, 1997, Laser ablation and micromachining with ultrashort laser pulses, Quantum Electronics, IEEE Journal of, 33(10): 1706-1716.
- [36] P.R. Miller, R. Aggarwal, A. Doraiswamy, Y.J. Lin, Y.S. Lee, R.J. Narayan, 2009, Laser micromachining for biomedical applications, JOM Journal of the Minerals, Metals and Materials Society, 61(9): 35-40.
- [37] B. Chichkov, C. Momma, S. Nolte, F. Von Alvensleben, A. Tünnermann, 1996, Femtosecond, picosecond and nanosecond laser ablation of solids, Applied Physics A: Materials Science & Processing, 63(2): 109-115.
- [38] R. Pfeifer, D. Herzog, M. Hustedt, S. Barcikowski, 2010, Pulsed nd: YAG laser cutting of NiTi shape memory alloys—Influence of process parameters, Journal of Materials Processing Technology, 210(14): 1918-1925.
- [39] N. Rajaram, J. Sheikh-Ahmad, S. Cheraghi, 2003, CO₂ laser cut quality of 4130 steel, International Journal of Machine Tools and Manufacture, 43(4): 351-358.
- [40] K. Yung, H. Zhu, T. Yue, 2005, Theoretical and experimental study on the kerf profile of the laser micro-cutting NiTi shape memory alloy using 355 nm nd: YAG, Smart Materials and Structures, 14(2): 337.
- [41] A. Ivarson, J. Powell, J. Kamalu, C. Magnusson, 1994, The oxidation dynamics of laser cutting of mild steel and the generation of striations on the cut edge, Journal of Materials Processing Technology, 40(3): 359-374.

- [42] M. Vicane, G. Simon, H. Urbassek, I. Decker, 1987, Hydrodynamical instability of melt flow in laser cutting, *Journal of Physics D: Applied Physics*, 20(1): 140.
- [43] L. Li, M. Sobih, P. Crouse, 2007, Striation-free laser cutting of mild steel sheets, *CIRP Annals-Manufacturing Technology*, 56(1): 193-196.
- [44] Y. Yan, L. Li, K. Sezer, D. Whitehead, L. Ji, Y. Bao, Y. Jiang, 2012, Nano-second pulsed DPSS nd: YAG laser striation-free cutting of alumina sheets, *International Journal of Machine Tools and Manufacture*, 53(1): 15-26.
- [45] N. Muhammad, D. Whitehead, A. Boor, W. Oppenlander, Z. Liu, L. Li, 2012, Picosecond laser micromachining of nitinol and platinum-iridium alloy for coronary stent applications, *Applied Physics A: Materials Science & Processing*, 1-11.
- [46] A. Stournaras, P. Stavropoulos, K. Salonitis, G. Chryssolouris, 2009, An investigation of quality in CO₂ laser cutting of aluminum, *CIRP Journal of Manufacturing Science and Technology*, 2(1): 61-69.
- [47] S. Lv, Y. Wang, S.J. Ji, 2006, Quality analysis of pulsed laser cutting of superalloy sheet, *Key Engineering Materials*, 315: 113-117.
- [48] B. Yilbas, 1997, Parametric study to improve laser hole drilling process, *Journal of Materials Processing Technology*, 70(1): 264-273.
- [49] C. Yeo, S. Tam, S. Jana, M.W. Lau, 1994, A technical review of the laser drilling of aerospace materials, *Journal of Materials Processing Technology*, 42(1): 15-49.
- [50] H. Tönshoff, C. Emmelmann, 1989, Laser cutting of advanced ceramics, *CIRP Annals-Manufacturing Technology*, 38(1): 219-222.
- [51] M.S. Amer, L. Dosser, S. LeClair, J.F. Maguire, 2002, Induced stresses and structural changes in silicon wafers as a result of laser micro-machining, *Applied Surface Science*, 187(3): 291-296.
- [52] M.H. Wu. 2002, *Materials Science Forum*, 285-292.
- [53] Y.P. Kathuria, 2006, The potential of biocompatible metallic stents and preventing restenosis, *Materials Science and Engineering: A*, 417(1-2): 40-48.
- [54] B. James, C. McVeigh, S. Rosenbloom, E. Guyer, S. Lieberman, 2010, Ultrasonic cleaning-induced failures in medical devices, *Journal of Failure Analysis and Prevention*, 10(3): 223-227.
- [55] Z.E. Geller, K. Albrecht, J. Dobránszky. 2008, *Materials science forum*, 367-372.

- [56] H. Zhao, J. Van Humbeeck, J. Sohler, I. De Scheerder, 2003, Electrochemical polishing of 316L stainless steel slotted tube coronary stents: An investigation of material removal and surface roughness, *Progress in Biomedical Research*, 8: 70-81.
- [57] L. Chen. 2008, *ICALEO 2008*, 320-324.
- [58] D. Strickland, G. Mourou, 1985, Compression of amplified chirped optical pulses, *Optics Communications*, 55(6): 447-449.
- [59] H. Huang, H. Zheng, G. Lim, 2004, Femtosecond laser machining characteristics of nitinol, *Applied Surface Science*, 228(1): 201-206.
- [60] H. Zheng, A. Zareena, H. Huang, 2003, Femtosecond laser processing of nitinol, *Applied Surface Science*, 228, 201-206.
- [61] W. Theisen, A. Schuermann, 2004, Electro discharge machining of nickel–titanium shape memory alloys, *Materials Science and Engineering: A*, 378(1–2): 200-204.
- [62] M. Amer, M. El-Ashry, L. Dosser, K. Hix, J. Maguire, B. Irwin, 2005, Femtosecond versus nanosecond laser machining: Comparison of induced stresses and structural changes in silicon wafers, *Applied Surface Science*, 242(1): 162-167.
- [63] C. Li, S. Nikumb, F. Wong, 2006, An optimal process of femtosecond laser cutting of NiTi shape memory alloy for fabrication of miniature devices, *Optics and lasers in engineering*, 44(10): 1078-1087.
- [64] A. Kruusing, 2004, Underwater and water-assisted laser processing: Part 1—general features, steam cleaning and shock processing, *Optics and Lasers in Engineering*, 41(2): 307-327.
- [65] J. Alfille, G. Pilot, D. de Prunele. 1996, *Lasers, Optics, and Vision for Productivity in Manufacturing I*, 134-144.
- [66] A. Dupont, P. Caminat, P. Bournot, J. Gauchon, 1995, Enhancement of material ablation using 248, 308, 532, 1064 nm laser pulse with a water film on the treated surface, *Journal of Applied Physics*, 78(3): 2022-2028.
- [67] M. Geiger, W. Becker, T. Rebhan, J. Hutfless, N. Lutz, 1996, Increase of efficiency for the XeCl excimer laser ablation of ceramics, *Applied Surface Science*, 96: 309-315.
- [68] N. Muhammad, D. Whitehead, A. Boor, L. Li, 2010, Comparison of dry and wet fibre laser profile cutting of thin 316L stainless steel tubes for medical device applications, *Journal of Materials Processing Technology*, 210(15): 2261-2267.

- [69] N. Muhammad, L. Li, 2012, Underwater femtosecond laser micromachining of thin nitinol tubes for medical coronary stent manufacture, *Applied Physics A: Materials Science & Processing*, 107(4): 849-861.
- [70] B. Richerzhagen, R. Housh, F. Wagner, J. Manley, 2004, Water jet guided laser cutting: A powerful hybrid technology for fine cutting and grooving, *Progress in Theoretical Chemistry and Physics*, chapter, 5.
- [71] C. Li, D. Johnson, R. Kovacevic, 2003, Modeling of waterjet guided laser grooving of silicon, *International Journal of Machine Tools and Manufacture*, 43(9): 925-936.
- [72] T.A. Mai, B. Richerzhagen, P.C. Snowdon, D. Wood, P.G. Maropoulos. 2007, *Lasers and Applications in Science and Engineering*, 64590P-64590P-7.
- [73] B. Richerzhagen, M. Kutsuna, H. Okada, T. Ikeda. 2003, *LAMP 2002: International Congress on Laser Advanced Materials Processing*, 91-94.
- [74] J. Manley, R. Housh, F. Wagner, B. Richerzhagen, 2004, Water-guided lasers create clean cuts, *Laser Focus World*, 40(5): S15-S18.
- [75] K. Hock, B. Adelman, R. Hellmann, 2012, Comparative study of remote fiber laser and water-jet guided laser cutting of thin metal sheets, *Physics Procedia*, 39: 225-231.
- [76] C.P. Cheng, N.M. Wilson, R.L. Hallett, R.J. Herfkens, C.A. Taylor, 2006, In vivo MR angiographic quantification of axial and twisting deformations of the superficial femoral artery resulting from maximum hip and knee flexion, *Journal of vascular and interventional radiology*, 17(6): 979-987.
- [77] D.E. Allie, C.J. Hebert, C. Walker, 2004, Nitinol stent fractures in the SFA, *Endovasc Today*, 7: 22-34.
- [78] A. Nikanorov, H.B. Smouse, K. Osman, M. Bialas, S. Shrivastava, L.B. Schwartz, 2008, Fracture of self-expanding nitinol stents stressed in vitro under simulated intravascular conditions, *Journal of vascular surgery*, 48(2): 435-440.
- [79] C.P. Cheng, G. Choi, R.J. Herfkens, C.A. Taylor, 2010, The effect of aging on deformations of the superficial femoral artery resulting from hip and knee flexion: Potential clinical implications, *Journal of Vascular and Interventional Radiology*, 21(2): 195-202.
- [80] A. Ganguly, J. Simons, A. Schneider, B. Keck, N.R. Bennett, R. Fahrig, 2011, In-vitro imaging of femoral artery nitinol stents for deformation analysis, *Journal of Vascular and Interventional Radiology*, 22(2): 236-243.
- [81] N.B. Morgan, 2004, Medical shape memory alloy applications—the market and its products, *Materials Science and Engineering: A*, 378(1-2): 16-23.

- [82] S. Robertson, A. Pelton, R. Ritchie, 2012, Mechanical fatigue and fracture of nitinol, *International Materials Reviews*, 57(1): 1-37.
- [83] K.N. Melton, O. Mercier, 1979, Fatigue of NITI thermoelastic martensites, *Acta Metallurgica*, 27(1): 137-144.
- [84] S. Miyazaki, Y. Sugaya, K. Otsuka. 1988, Proceedings of the MRS International Meeting on Advanced Materials. 251-256.
- [85] G. Eggeler, E. Hornbogen, A. Yawny, A. Heckmann, M. Wagner, 2004, Structural and functional fatigue of NiTi shape memory alloys, *Materials Science and Engineering: A*, 378(1): 24-33.
- [86] A.M. Figueiredo, P. Modenesi, V. Buono, 2009, Low-cycle fatigue life of superelastic NiTi wires, *International Journal of Fatigue*, 31(4): 751-758.
- [87] S. Miyazaki, K. Mizukoshi, T. Ueki, T. Sakuma, Y. Liu, 1999, Fatigue life of Ti-50 at.% ni and Ti-40Ni-10Cu (at.%) shape memory alloy wires, *Materials Science and Engineering: A*, 273: 658-663.
- [88] T.A. Sawaguchi, G. Kausträter, A. Yawny, M. Wagner, G. Eggeler, 2003, Crack initiation and propagation in 50.9 at. pct ni-ti pseudoelastic shape-memory wires in bending-rotation fatigue, *Metallurgical and Materials Transactions A*, 34(12): 2847-2860.
- [89] H. Tobushi, T. Hachisuka, S. Yamada, P. Lin, 1997, Rotating-bending fatigue of a TiNi shape-memory alloy wire, *Mechanics of Materials*, 26(1): 35-42.
- [90] M. Wagner, T. Sawaguchi, G. Kausträter, D. Höffken, G. Eggeler, 2004, Structural fatigue of pseudoelastic NiTi shape memory wires, *Materials Science and Engineering: A*, 378(1): 105-109.
- [91] J. Yang. 1997, SMST: Proceedings os the Second International Conference on Shape Memory and Superelastic Technologies, 479-484.
- [92] J.M. Young, K.J. Van Vliet, 2005, Predicting in vivo failure of pseudoelastic NiTi devices under low cycle, high amplitude fatigue, *Journal of Biomedical Materials Research Part B: Applied Biomaterials*, 72(1): 17-26.
- [93] D. Tolomeo, S. Davidson, M. Santinoranout. 2000, Proc. Int. Conf. on 'SMST', 409-417.
- [94] A. Pelton, V. Schroeder, M. Mitchell, X. Gong, M. Barney, S. Robertson, 2008, Fatigue and durability of nitinol stents, *Journal of the mechanical behavior of biomedical materials*, 1(2): 153-164.

- [95] W. Predki, M. Klönne, A. Knopik, 2006, Cyclic torsional loading of pseudoelastic NiTi shape memory alloys: Damping and fatigue failure, *Materials Science and Engineering: A*, 417(1–2): 182-189.
- [96] A. Runciman, D. Xu, A.R. Pelton, R.O. Ritchie, 2011, An equivalent strain/Coffin–Manson approach to multiaxial fatigue and life prediction in superelastic nitinol medical devices, *Biomaterials*, 32(22): 4987-4993.
- [97] S. Shabalovskaya, J. Anderegg, J. Van Humbeeck, 2008, Critical overview of nitinol surfaces and their modifications for medical applications, *Acta biomaterialia*, 4(3): 447-467.
- [98] S.W. Robertson, R.O. Ritchie, 2007, In vitro fatigue–crack growth and fracture toughness behavior of thin-walled superelastic nitinol tube for endovascular stents: A basis for defining the effect of crack-like defects, *Biomaterials*, 28(4): 700-709.
- [99] Bannantine JA, Comer JJ, Handrock JL. 1990. *Fundamentals of metal fatigue analysis*. Prentice Hall Englewood Cliffs, NJ.
- [100] A. Javidi, U. Rieger, W. Eichlseder, 2008, The effect of machining on the surface integrity and fatigue life, *International Journal of Fatigue*, 30(10): 2050-2055.
- [101] C.W. Chan, H.C. Man, F.T. Cheng, 2013, Fatigue behavior of laser-welded NiTi wires in small-strain cyclic bending, *Materials Science and Engineering: A*, 559(0): 407-415.
- [102] L. Reclaru, R. Lerf, P.-. Eschler, J.-. Meyer, 2001, Corrosion behavior of a welded stainless-steel orthopedic implant, *Biomaterials*, 22(3): 269-279.
- [103] G. Manivasagam, D. Dhinasekaran, A. Rajamanickam, 2010, Biomedical implants: Corrosion and its prevention—a review, *Recent Patents on Corrosion Science*, 2: 40-54.
- [104] O. Cisse, O. Savadogo, M. Wu, L.H. Yahia, 2002, Effect of surface treatment of NiTi alloy on its corrosion behavior in hanks' solution, *Journal of Biomedical Materials Research*, 61(3): 339-345.
- [105] L. Castleman, S. Motzkin, F. Alicandri, V. Bonawit, A. Johnson, 1976, Biocompatibility of nitinol alloy as an implant material, *Journal of Biomedical Materials Research*, 10(5): 695-731.
- [106] N. Figueira, T. Silva, M. Carmezim, J. Fernandes, 2009, Corrosion behaviour of NiTi alloy, *Electrochimica Acta*, 54(3): 921-926.
- [107] V. Schroeder, 2009, Evolution of the passive film on mechanically damaged nitinol, *Journal of Biomedical Materials Research Part A*, 90(1): 1-17.
- [108] S. Shabalovskaya, J. Ryhänen, L.H. Yahia. 2002, *Materials Science Forum*, 131-138.

- [109] C.C. Shih, S.J. Lin, K.H. Chung, Y.L. Chen, Y.Y. Su, 2000, Increased corrosion resistance of stent materials by converting current surface film of polycrystalline oxide into amorphous oxide, *Journal of Biomedical Materials Research*, 52(2): 323-332.
- [110] D. Starosvetsky, I. Gotman, 2001, Corrosion behavior of titanium nitride coated Ni–Ti shape memory surgical alloy, *Biomaterials*, 22(13): 1853-1859.
- [111] G. Wang, Y. Shen, Y. Cao, Q. Yu, R. Guidoin, 2007, Biocompatibility study of plasma-coated nitinol (NiTi alloy) stents, *IET Nanobiotechnology*, 1(6): 102-106.
- [112] B.G. Pound, 2006, Susceptibility of nitinol to localized corrosion, *Journal of Biomedical Materials Research Part A*, 77(1): 185-191.
- [113] B. Thierry, M. Tabrizian, C. Trepanier, O. Savadogo, L.H. Yahia, 2000, Effect of surface treatment and sterilization processes on the corrosion behavior of NiTi shape memory alloy, *Journal of Biomedical Materials Research*, 51(4): 685-693.
- [114] D. Wever, A. Veldhuizen, M. Sanders, J. Schakenraad, J. Van Horn, 1997, Cytotoxic, allergic and genotoxic activity of a nickel-titanium alloy, *Biomaterials*, 18(16): 1115-1120.
- [115] N. Balakrishnan, B. Uvelius, P. Zaszczurynski, D.L. Lin, M.S. Damaser, 2005, Biocompatibility of nitinol and stainless steel in the bladder: An experimental study, *The Journal of urology*, 173(2): 647-650.
- [116] S.A. Shabalovskaya, G.C. Rondelli, A.L. Undisz, J.W. Anderegg, T.D. Burleigh, M.E. Rettenmayr, 2009, The electrochemical characteristics of native nitinol surfaces, *Biomaterials*, 30(22): 3662-3671.

CHAPTER 3

A STUDY OF DEFORMATION BEHAVIOR AND MATERIAL PROPERTIES OF NITINOL USING LOW PLASTICITY BURNISHING

Abstract

Nitinol alloys have received considerable attention in biomedical and aerospace applications. Surface integrity of Nitinol devices by various manufacturing processes is crucial for their functionality. Low plasticity burnishing (LPB) is very promising to modify surface integrity due to its unique capability to adjust material properties down to the deep subsurface on the order of a few millimeters. Burnishing mechanics is essential to understand its effect on surface properties. The depth and width of burnished surface materials are characterized to understand the deformation behavior of Nitinol. A 3-dimensional finite element simulation has been developed to incorporate the superelastic mechanical behavior of Nitinol. The simulation predictions are validated with the experimental results. The contact stresses, residual stresses, and strain profiles are investigated to better understand burnishing mechanics.

Nomenclature

E^*	Effective Modulus
E_1	Elastic modulus of the tool
E_2	Elastic modulus of the workpiece
ν_1	Poisson's ratio of the tool
ν_2	Poisson's ratio of the workpiece
R	Effective curvature
R_1	Curvature of tool
R_2	Curvature of the workpiece
F	Burnishing force
P	Load input
r	Radius of the tool
a	Contact radius
p_0	Maximum contact pressure
δ	Approach of distant points
τ_1	Maximum shear stress
σ_r	Maximum tensile stress
$\sigma_{1,2,3}$	Principal stresses
E_a	Austenite elasticity
V_a	Austenite Poisson's ratio
E_m	Martensite elasticity
V_m	Martensite Poisson's ratio
ε^L	Transformation strain
$(\frac{\delta\sigma}{\delta T})_L$	$(\frac{\delta\sigma}{\delta T})$ loading
σ_L^S	Start of transformation loading
σ_L^E	End of transformation loading
T_0	Reference temperature
$(\frac{\delta\sigma}{\delta T})_U$	$(\frac{\delta\sigma}{\delta T})$ unloading
σ_U^S	Start of transformation unloading
σ_U^E	End of transformation unloading
σ_{CL}^E	Start of transformation stress during loading in compression, as a positive value
ε_V^L	Volumetric transformation strain
N_p	Number of stress-strain pairs to define yield curve
$\sigma_{11}^p, \varepsilon_1, \dots, \sigma_{111}^p, \varepsilon_{11}$	Stress-strain points in the yield curve
$S22$	Normal stress in width direction
$S33$	Normal stress in depth direction
$PE33$	Plastic strain in depth direction
z	Distance underneath the surface

3.1 Introduction

3.1.1 Nitinol Alloy

Nitinol is a nickel-titanium alloy of near equiatomic composition with superelastic mechanical properties as well as shape memory properties. Slight variations in the binary alloy composition change the mechanical properties significantly; moreover, heat treatment history and finishing of the material play a vital role in the mechanical properties as well. Typically, superelasticity occurs at elevated temperatures that approach the melting point of the material. Nitinol is composed of nickel and titanium and the accompanying characteristics of both metals distinguish overall properties of a superalloy. Nitinol has superelastic features well below the melting point. As a result, these material properties are advantageous to various biomedical and aerospace applications. Nitinol was first discovered in the early 1960's and some of the first experimental work was conducted by the Naval Ordnance Laboratory. Many of the early applications of Nitinol focused on the shape memory effect where in the recent years a lot of attention has been aimed toward the superelasticity of Nitinol with particular emphasis in biomedical applications. The physiological conditions of the in vivo environment within the human body are isothermal where the temperature of the body turns out to be ideal for the superelastic properties of binary Nitinol [1]. The non-linear effect of the superelasticity of Nitinol is based on a mechanical event where a diffusionless fully reversible phase transformation evolves. The superelasticity effect of Nitinol originates in an austenitic parent phase where the continued application of stress results in a martensitic phase evolution and this stress induced phase transition is commonly referred to as stress induced martensite (SIM). Nitinol is an ordered intermetallic that has an extremely narrow composition range below 630°C the eutectoid in the phase diagram [2,3].

3.1.2 Surface Integrity

Surface integrity of Nitinol is important for the resistance to corrosion and wear which are primary failure mechanisms in Nitinol devices and components. Surface integrity of a Nitinol device has been shown to correlate the biocompatibility of biomedical Nitinol devices and components [4] where the poor surface finish of biomedical Nitinol devices and components has been shown to produce poor resistance to corrosion [5]. The contribution to high wear resistance of Nitinol is due to several factors, such as: pseudoelasticity, strain hardening, as well as hardness [4,6]. Hence, it shows that a surface modification process is able to enhance these features of a Nitinol implantation device for improving the ability to mitigate corrosion and wear.

3.1.3 Low Plasticity Burnishing

Due to the elegant nature of (50.8 at%Ni-49.2 at%Ti) superelastic (SE) Nitinol, recent attention has been focused on biomedical applications. It is critical that the material has superior resistance to corrosion with excellent fatigue life while meeting and exceeding Food and Drug Administration (FDA) guidelines. According to the 2010 guideline established by FDA, it is recommended that vascular stents undergo bench top pulsatile fatigue testing replicating pressure cycles at accelerated frequencies relative to human conditions. Hence, this particular guideline indicates that a fatigue life requirement of 10 years equivalent to human in vivo physiological conditions substantiates sufficient proof of safety for most patients [7,8]. Low plasticity burnishing (LPB) is a surface finishing technique to tailor surface integrity for specific applications. LPB is a low plasticity process that enhances surface integrity features such as roughness and hardness while providing longer fatigue life [9,10]. LPB is known for producing

high compressive residual stresses in the deeper subsurface, which has been attributed to longer high-cycle fatigue life. LPB provides a deep stable layer of compressive residual stresses in nickel, titanium, steels, and aluminum alloys that can exceed 1mm in depth, which typically exceed the depth of typical corrosion pits [10,11]. LPB is unique in the respect that it employs low plastic cold-work, usually less than 3-5% [12,13], where typical surface modification processes such as shot peening often produce cold-work greater than 80% [2]. A conventional CNC milling machine can be used to implement the process with respect to the desired workspace. Hence, it is thereby hypothesized that LPB would be an enabling surface modification process to improve surface integrity of superelastic Nitinol biomedical devices.

3.1.4 Research Objective

LPB has a great potential to surface treatment of Nitinol alloys for improving fatigue life. However, very little work has been done to understand the basic process mechanics of LPB of Nitinol alloys. Furthermore, the previous studies on burnishing steel alloys are mostly limited to 2D simulations [14,15]. SE508 Nitinol has a unique stress-strain response including phase transformation upon mechanical loading. Therefore, this research aims to provide a deeper understanding to process mechanics of burnishing SE508 Nitinol. The objectives of the study are to: (1) develop a three dimensional (3D) finite element simulation of ball burnishing to provide a basic understanding of process mechanism; (2) predict the contact pressure to induce plastic deformation under the applied load; and (3) gain insight into the stress/strain development in ball burnishing.

3.2 LPB Experiment

3.2.1 Experimental Setup

LPB was performed on a Cincinnati Arrow 2 CNC machine. The process is implemented with the use of a high modulus freely rotating spherical ball that is rolled over the workpiece surface under applied pressures [16]. A schematic of LPB process is seen in Fig. 3.1.

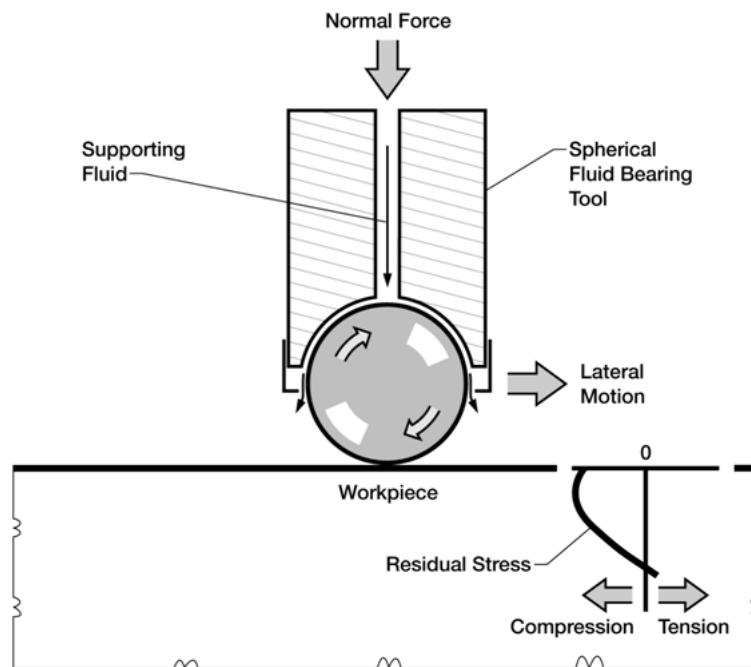


Fig. 3.1 Schematic of low plasticity burnishing (LPB).

A fixture design was necessary to conduct LPB experiments. The fixture design allows the use of a load cell such that the applied load could be measured in order to verify LPB process parameters. Fig. 3.2 illustrates the fixture where a cavity on the top face of the fixture, along with a peripheral fitting, was machined to securely hold the workpiece such that steady-state operating conditions can be ensured. The top plate of the fixture rests on 4 posts where a load cell securely rests below capturing the load data while in operation. The Ecoroll LPB tool with a 12.7 mm ball

diameter was used. The LPB tool was moved at a constant speed of 1000 mm/min in this experiment. The high pressures by the LPB tool are controlled by hydraulic fluid that tends to spill on the workpiece and surrounding areas. The hydraulic fluid is machine friendly and acts as a coolant. The burnishing experimental setup is shown in Fig. 3.3.

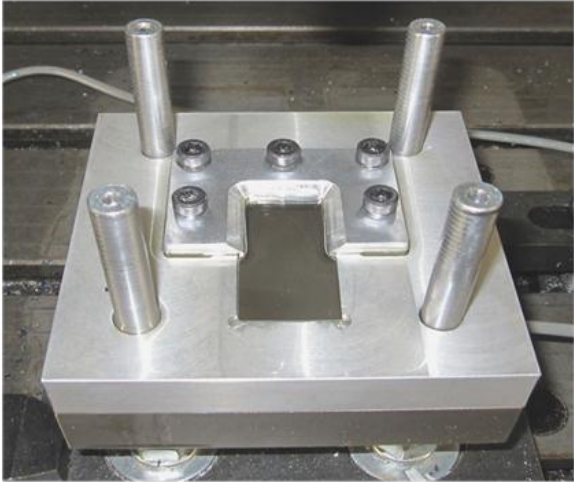


Fig. 3.2 LPB fixture design.

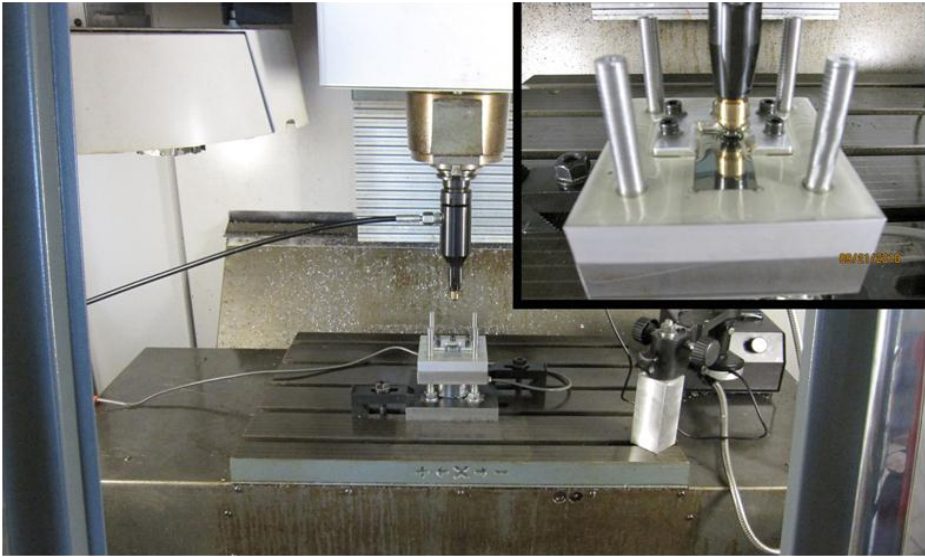


Fig. 3.3 LPB experimental setup.

3.2.2 SE508 Work Material

The work material is superelastic Nitinol SE508 (55.8 at%Ni-44.2 at%Ti) in thin sheet form. The particular compositions of binary nickel-titanium are commonly used in biomedical applications since the mechanical properties are similar to those of biological tissues [17]. The average grain size of the as-received austenitic parent phase Nitinol sheet samples were on the order of ~40 μm . Cold-working is capable of transforming the parent austenite phase into a martensite phase by localized stress distributions (SIM) [18]. The as-received Nitinol sheets are 1.5 mm in thickness and were cut to size by electrical discharge machining (EDM), and mechanically polished to a mirror finish to allow precise measurement of burnished surface profiles [19]. Similarly, a smooth surface contact to the burnishing ball allows for better accuracy in characterizing the experimental results. [Table 3.1](#) illustrates the composition of SE508 Nitinol.

[Table 3.1](#) Composition of the SE508 Nitinol

Nickel (nominal):	55.8 wt.%
Titanium:	Balance
Oxygen (max):	0.05 wt.%
Carbon (max):	0.02 wt.%

3.3 LPB Process Analysis

3.3.1 Burnishing Pressure/Force

The objective is to induce small amounts of uniform plasticity where the tool is in contact with the surface of the workpiece. The quasi-static mechanical properties of SE508 Nitinol may serve as a guideline to determine the critical region of desired plasticity. Hertz theory of elastic contact may be employed within the limits of small deformation [20,21] to characterize the applied LPB loads for SE508 Nitinol. When considering the force input for LPB process, it is important to quantify several parameters such as the tool radius, the effective curvature and stiffness of the tool with respect to the workpiece. These input variables may be quantified by the following equations of Hertz elastic contact.

$$E^* = \left(\frac{1 - \nu_1^2}{E_1} + \frac{1 - \nu_2^2}{E_2} \right)^{-1} \quad 3.1$$

$$\frac{1}{R} = \left(\frac{1}{R_1} + \frac{1}{R_2} \right) \quad 3.2$$

$$F = P \times \pi \times r^2 \quad 3.3$$

The material properties of the Ecoroll LPB ball and the workpiece are listed in [Table 3.2](#). The effective modulus considers the tool and the workpiece; however, the workpiece has two regions of elasticity where the austenitic and martensitic elastic regions were averaged as the overall modulus of elasticity for the workpiece. Since the workpiece is a thin plate of infinite curvature, the value of R_2 is null.

Table 3.2 Material Properties of the LPB Ball

E* (MPa)	E ₁ (MPa)	E ₂ (MPa)	ν ₁	ν ₂	R (mm)	R ₁ (mm)	R ₂ (mm)	r (mm)
37162	315000	37998	0.26	0.3	6.35	6.35	∞	6.35

3.3.2 Peak Pressure vs. Stress-Strain Curve

The peak Hertz pressure p_0 is consistent with the true stress at the corresponding strains in the quasi-static stress-strain curve of SE508 Nitinol. The experimental plan of this investigation is based on Hertz contact theory of elastic bodies and such corresponding values may be observed in Table 3.3. The theoretical pressure values are plotted with the measured quasi-static stress-strain mechanical properties in Fig. 3.4. In the theoretical curve, the pressure values were determined by Hertzian theory, and the corresponding strain values were selected according to the experimental stress-strain response of the material. This plot suggests that values of Hertz peak pressures correspond to true stress and strain values and may serve as a valuable tool in determining the LPB input pressures. Based on Hertzian elastic contact, the contact radius of the spherical indenter is a function of the input load as well as the effective stiffness and curvatures of the two elastic materials in contact. The maximum contact pressure derives from load input with respect to the burnishing ball. Furthermore, the burnishing depth is a function of load input, ball geometry, and an overall effective stiffness. These values may be obtained from the following equations:

$$a = \left(\frac{3 \cdot P \cdot R}{4 \cdot E^*} \right)^{1/3} \quad 3.4$$

$$p_0 = \left(\frac{3 \cdot P}{2 \cdot \pi \cdot a^2}\right) \quad 3.5$$

$$\delta = \left(\frac{9}{16} \frac{P^2}{R \cdot E^*2}\right)^{1/3} \quad 3.6$$

Table 3.3 LPB Experiment Plan

Sample #	Pressure (MPa)	F (N)	p_0 (MPa)	a (mm)	δ (μm)	τ_{max} (MPa)	σ at $r = a$ (MPa)
1	0.15	19	500	0.13	3	155	67
2	0.61	77	800	0.21	7	248	107
3	1.19	151	1000	0.27	11	310	133
4	4.02	509	1500	0.40	26	465	200
5	9.53	1207	2000	0.54	45	620	267
6	13.57	1719	2250	0.60	57	698	300
7	15	1900	2327	0.62	61	721	310
8	20	2534	2561	0.69	74	794	341

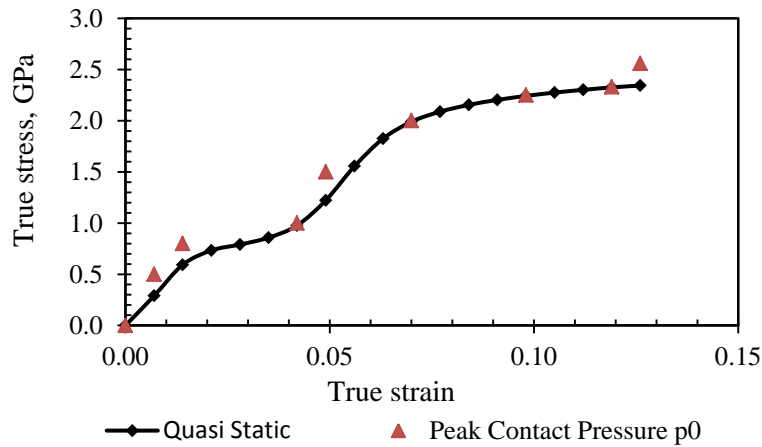


Fig. 3.4 Quasi-static mechanical properties compared with Hertz peak pressure.

3.3.3 Track Depth/Width

During spherical indentation on the surface of a flat contact area, the effect of sink-in and pile-up occur where the load is applied. When the indented material is deformed elastically, the effect of sinking-in occurs. However, when the indented material exceeds the yield stress, the increase in plastic deformation of the indented material has a decrease in sinking-in and an increase in pile-up. The presence of these particular characteristics causes inaccuracies in determining the projected area of contact [22]. It is important to establish a high degree of accuracy when evaluating the true contact area geometry yet the contact area from indentation load-depth data is not necessarily a straightforward process since there is a dependence on the amount of pile-up or sink-in of material around the edge of the indentation [20,23]. Moreover, the effect of pile-up is influenced by loading pressure and the strain hardening mechanical properties of the work material. A general trend can be noted whereas the increase of pressure increases dislocation density with the microstructure of the material and is the dominant factor affecting fatigue life. However, there are a combined series of factors that influence the hardness and surface roughness of the material and not a single stand alone factor [11]. In biomedical applications, the effect of superelasticity is the attractive property of Nitinol and it is vital to preserve the superelastic features. The amount of cold work induced by LPB is of low magnitude and yet the fatigue life can substantially be increased as well as corrosion performance standards. The highest level of cold work induced in this study was 0.2%. Dektak II surface profilometer was used to measure the depth and width of burnished profiles. A governing factor of the LPB process is the size of the tool tip and the applied pressure whereby an acceptable feed may be established. [Table 3.4](#) illustrates the LPB pressures with respect to contact width, depth, and contact radius. It was found that the width of the indentation tracks changed very little with the

increase of pressure although the track width was substantially larger than the penetration depth, which was expected. The contact radius pertains to the Hertzian contact model of an elastic solid.

Table 3.4 shows that the first three burnishing pressures caused only elastic indentation.

Table 3.4 Pressure vs. Burnishing Depth/Width

Pressure (MPa)	Depth (μm)	Width (μm)	Contact Radius (μm)
0.15	-	-	134.2
0.61	-	-	214.7
1.19	-	-	268.4
4.02	0.17	1648.2	402.7
9.53	0.34	1814.8	536.8
13.57	1.33	1879.7	603.9
15	1.14	1666.7	624.5
20	4.18	2018.5	687.3

3.3.4 Maximum Shear Stress and Location in Subsurface

When two elastic solid bodies come into contact the onset of plasticity is dependent on the hardness of the two bodies and loading conditions. For this particular contact problem, the initiation of plastic yielding occurs beneath the surface while creating a stress field. Expressions for the subsurface shear stresses may be observed in equation (3.7) for $\nu = 0.3$ [20]. A linear relationship exists with the Hertzian theoretical values of shear stress and subsurface location. Moreover, a general rule of thumb is that the locations of subsurface maximum shear stresses are about half the distance of the contact radius. This particular characteristic is ideal for generating deep subsurface compressive residual stresses by the use of LPB with a spherical tool tip. The magnitude of the stress field increases as indentation depth or force increases. Once the stress field reaches an equivalent point within the specimen, the material will start to transform to martensite with an increasing hardness [21,24]. According to Hertz theory of contact mechanics,

it can be observed in equation (3.7) that the maximum shear stress is 31% of the applied maximum contact pressure applied at the center of contact. The Hertzian contact solutions hold true in a purely elastic state and a generalized Von Mises Stress criterion is commonly used as a yielding envelope. Upon the average of the principal stresses with the Von Mises criterion, it can be assumed that plastic flow occurs when the distortional strain energy reaches a critical value and the result of the initiated yielding may be observed in equation (3.8).

A consideration of the Hertzian contact mechanics is the sensitivity of Poisson's ratio with respect to the contact angle. The load case of a spherical surface in contact with an infinitely flat surface also bears the consideration of the contact angles and the effect of the surface and subsurface stresses [25,26]. Similarly, the maximum tensile stress for this load case may be ascertained by equation (3.9) where the maximum tensile stress resides at the surface of the work material just outside the contact patch. The radial stress is therefore tensile outside the loaded area. It reaches a maximum value at the edge of the circle at $r = a$. This is the maximum tensile stress occurring anywhere [20]. We can observe that the poisson effect is a parameter involved in the generated tensile stress field whereby a stress deviator has the propensity to exist. It would also be desirable to the intended application for smooth surface to surface contact where many studies indicate the difficulty in the assumptions of classical Hertzian contact mechanics with relation to surface and subsurface stress fields.

Hertz theory of contact mechanics between two elastic bodies imposes the assumption that the contact surfaces are topographically smooth whereby perfect contact takes place. In reality all surfaces are rough to some extent where the true contact takes place at the crest of the surface asperities [19]. Therefore, it implies that smoother surfaces allow a higher degree of

accuracy in determining surface and subsurface stress fields. This becomes an important factor in regard to subsurface residual stresses and the LPB process.

$$\tau_1 = 0.31 \cdot p_0, \text{ at } r = 0, z = 0.48 \cdot a \quad 3.7$$

$$(\sigma_1 - \sigma_2)^2 + (\sigma_2 - \sigma_3)^2 + (\sigma_3 - \sigma_1)^2 = 2 \cdot \sigma_y^2 \quad 3.8$$

$$\sigma_r = \frac{1}{3}(1 - 2\nu_2) \cdot p_0, \text{ at } r = a, z = 0 \quad 3.9$$

3.4 Experimental Results

3.4.1 Characterization of Burnishing Tracks

On the premise that small deformations are imposed upon SE508 Nitinol in this experiment, Hertz theory of contact can be used for a basis model. There are challenges involved with predicting an accurate baseline model when the elastic range of the material is far beyond conventional. The aforementioned experimental plan constitutes the basis of the burnished pressures based on the Hertzian maximum contact pressure and experimentally determined compressive quasi-static stress-strain values. The spring back due to superelasticity may be observed in [Fig. 3.5](#).

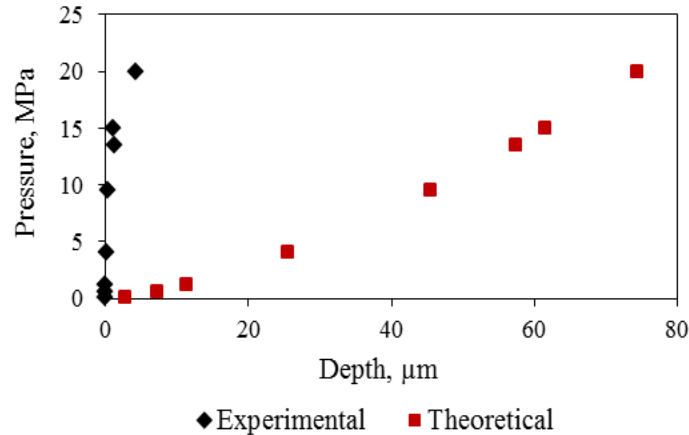


Fig. 3.5 Burnishing pressure vs. theoretical and experimental depth.

Hence, it is necessary to experimentally determine process parameters for LPB. It was determined that the first three applied loads were purely elastic and the critical threshold to induce plastic deformation was established at approximately 4 MPa with respect to a tool tip diameter of 12.7mm. The depth of penetration in Hertz theory of contact mechanics resides in the elastic region and therefore does not indicate permanent indentation. However, it is interesting to note the difference of the indentation depth induced by plasticity in comparison with Hertz theory of elastic contact. While Hertz contact mechanics is not a gauge of the plastic depth of penetration, we can ascertain that there is a large region of elastic springback of this material. We can also use this methodology to predict elasto-plasticity and the evolution of fully-plastic behavior upon the critical threshold of the burnishing pressure to induce plasticity. Past studies indicate that relative high values of pressure and speed are dominating factors where tool speed is a dominating factor in post-processing efficiency. The speed, or dwell time, of the tool has an effect of the evolution of plasticity yet the tool speed was kept at a relatively high value in comparison to literature in efforts for post-processing efficiency and longer fatigue life [18]. An investigation by Seemikeri et al reflected that the dominating parameter was the applied pressure

for increasing fatigue life whereby there was no single factor that had an effect on surface roughness but a combination of parameters [18]. We can expect that there will be greater hardness and pile-up when the spherical tool tip has greater contact area [23,27,28]. As one would expect, the track profiles vary in depth with respect to pressure inputs. However, [Table 3.4](#) shows that there is very little variance in width of each profile tracks. There was undetectable depth penetration with the first three pressure inputs although the remaining pressure inputs reflected depth penetrations ranging from 0.2 μm -4.0 μm with a percent cold work ranging from 0.01% - 0.2%, respectively. The cold work involved in LPB is rather small and therefore the superelastic properties of SE508 Nitinol are not compromised.

3.5 Finite Element Analysis Procedure

3.5.1 Mesh

A 3D finite element model was developed to simulate LPB of SE508 Nitinol using ABAQUS/Explicit [29]. The advantage of the explicit solver is that it is considered to be inexpensive both in time and space since no large number of equations is solved simultaneously. However, the drawback is that a convergence is not guaranteed.

The finite element mesh for burnishing is presented in [Fig. 3.6](#). The workpiece is 1.5 mm in depth which is consistent with actual experimental sample. The width and length of the sample are 2 mm and 8 mm. This simulation consists of two steps. The first step is to roll the ball on workpiece with an applied load and the second step is to remove applied load and lift up the ball. The ball is assumed to be rigid to reduce the computational time since the elastic modulus of the ball is much higher than the workpiece. The ball has an applied load in the center and it is assigned with a rotational speed ω . The rolling distance is 4 mm along positive X direction. The

starting point of rolling is 2 mm away from the left edge. The model is designed to be symmetric about X-Z plane in order to simplify the simulation process and decrease the computational time. The workpiece contains both 8-node 3D finite element with temperature degree of freedom (C3D8RT) and 8-node semi-infinite element (CIN3D8). Semi-infinite elements were used along the left and right surfaces to ensure a non-reflective boundary. This model has 472,628 elements and 503,745 nodes. At the ball/workpiece contact zone, a fine mesh is used. In the far field where there is no contact, a coarse mesh is used. The fine mesh region consists of 10 μm long, 10 μm wide, and 2 μm deep elements. These fine elements were used to provide a suitable spatial resolution with respect to output variables. The friction coefficient is assumed to be 0.05 in order to simulate the highly lubricated interface between the ball and workpiece.

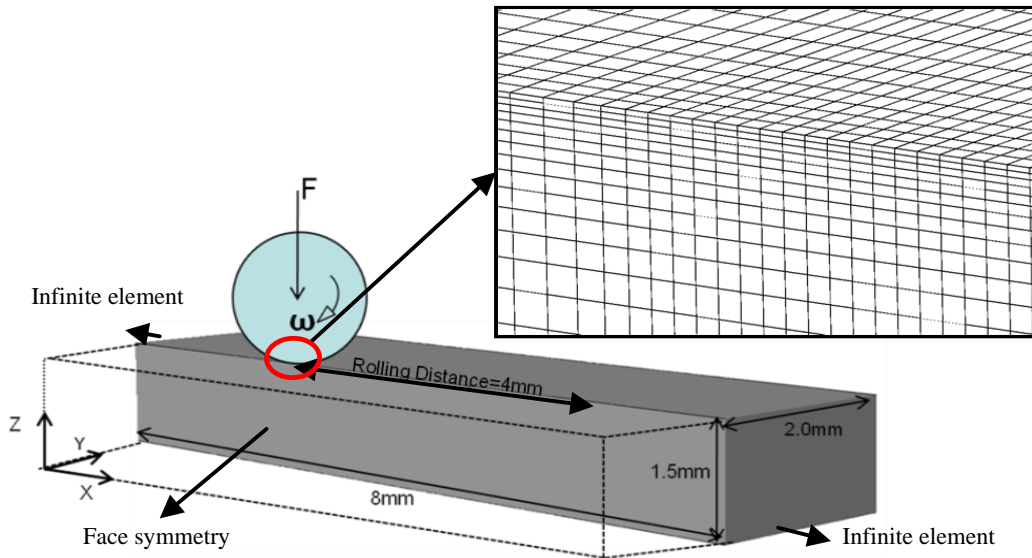


Fig. 3.6 Three-dimensional FEA of burnishing (not to scale).

3.5.2 Loading Condition

Two loads were used in the burnishing simulations and the resulting burnished tracks were measured. These two loads are chosen to produce a plastic deformation on the workpiece. The specific loading condition is listed in [Table 3.5](#).

[Table 3.5](#) LPB Loading in FEA Simulations

Load 1(N)	Load 2 (N)
2540.79	1716.75

3.5.3 Modeling of Superelastic-Plastic Behavior of SE508

In order to model the superelastic-plastic behavior of SE508 Nitinol, a built-in user material subroutine was used in ABAQUS [29], the material inputs are obtained by a curve fitting the experimental data in uniaxial compression to the theoretical stress-strain curve ([Fig. 3.7](#)), under the assumption that tension and compression curve are symmetric with each other. The material constants are listed in [Table 3.6](#).

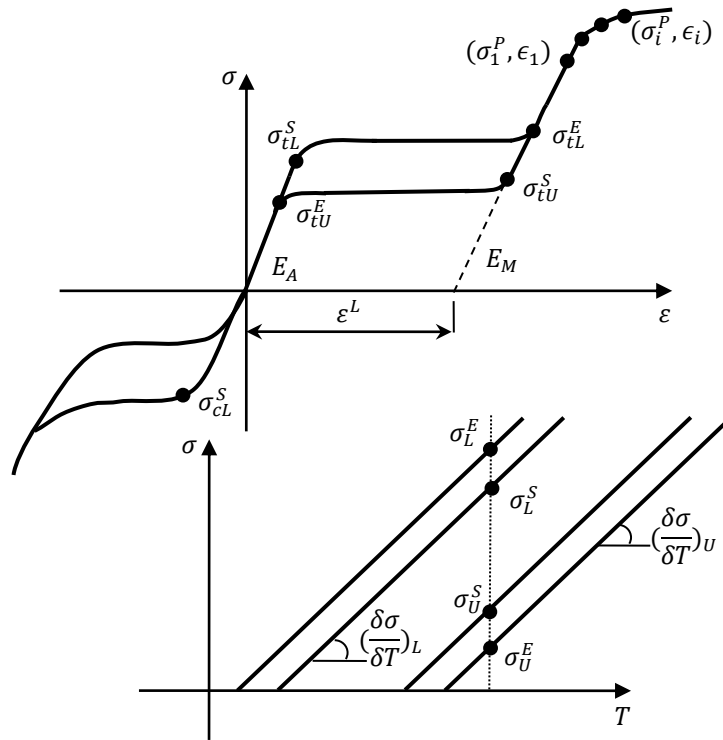


Fig. 3.7 Superelastic-plastic behavior based on the uniaxial behavior [29].

Table 3.6 Material Constants of SE508 Nitinol

Material parameter	Material Constant	Material Parameter	Material Constant
E_a (Pa)	4.23e+10	σ_3^P (Pa)	1.990e+9
V_a	0.3	ϵ_3	0.070
E_m (Pa)	4.29e+10	σ_4^P (Pa)	2.088e+9
V_m	0.3	ϵ_4	0.077
ϵ^L	0.02	σ_5^P (Pa)	2.155e+9
$\left(\frac{\delta\sigma}{\delta T}\right)_L$	0	ϵ_5	0.084
σ_L^S (Pa)	6.00e+8	σ_6^P (Pa)	2.203e+9
σ_L^E (Pa)	1.20e+9	ϵ_6	0.091
T_0 (C°)	22	σ_7^P (Pa)	2.424e+9
$\left(\frac{\delta\sigma}{\delta T}\right)_U$	0	ϵ_7	0.098
σ_u^S (Pa)	5.00e+8	σ_8^P (Pa)	2.275e+9
σ_u^E (Pa)	2.00e+8	ϵ_8	0.105
σ_{CL}^E (Pa)	6.00e+8	σ_9^P (Pa)	2.302e+9
ϵ_V^L	0.02	ϵ_9	0.112
N_p	11	σ_{10}^P (Pa)	2.325e+9
σ_1^P (Pa)	1.556e+9	ϵ_{10}	0.119
ϵ_1	0.056	σ_{11}^P (Pa)	2.343e+9
σ_2^P (Pa)	1.825e+9	ϵ_{11}	0.126
ϵ_2	0.063		

3.6 Simulation Results

3.6.1 Dent Profiles vs. Experimental Data

The comparison between the predicted track profile and experimental track profile under load 1 is shown in Fig. 3.8. Three paths toward width direction were taken on rolling pass. Track profile of each path was plotted. In addition, an average track profile was also plotted. The simulated track width is approximately 2mm and the depth is 2.5 μ m. Generally, there is a good agreement between simulation result and experimental result with regard to deformation and track shape. However, as it is shown in Fig. 3.8, there is no “pile-up” effect observed in simulation while there is a “pile-up” with a height of 0.5 μ m in experiment. This discrepancy

might be due to the assumption of pure rolling in the simulation. Typically, a burnishing process is a combination of rolling and sliding contact. However, the percentage of each contact condition is next impossible to measure in experiment and hence, is hard to simulate. In this study, with the consideration of the presence of lubricant and the free rotate tool tip, the assumption of pure rolling contact is made.

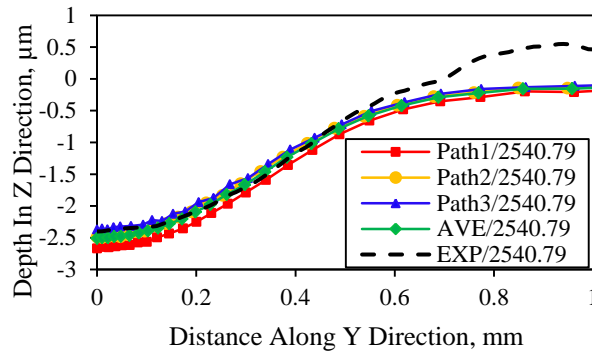


Fig. 3.8 Experimental and simulated track profiles.

3.6.2 Stress Profiles of Loaded Condition

Von Mises, S22, and S33 stresses along the depth direction at the two different loads are shown in Fig. 3.9(a), (b) and (c). In Fig. 3.9(a), the maximum Von Mises stress is 2.09 GPa occurring at 0.37 mm in subsurface for load 1. For load 2, a maximum stress of 1.75 GPa at a depth of 0.32 mm can be found. The magnitude of S33 stress will also increase with burnishing load. However, Fig. 3.9(c) shows that the increase in load does not affect the magnitude of S22.

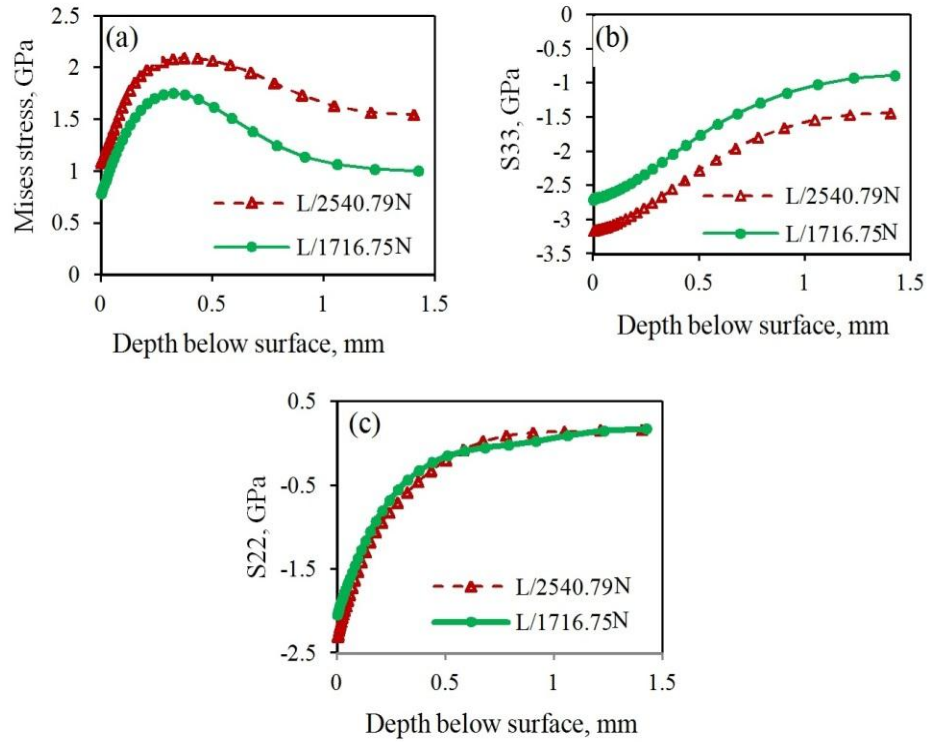


Fig. 3.9 Von Mises stress (a) S33 stress (b) S22 stress, and (c) in subsurface.

Since this is a 3D study, the stress profiles in width direction can also be studied. For both S22 and S33 (Fig. 3.10), there is a compression region up to 1 mm, and then S22 change from compression to tension while S33 approaches to zero. With a greater applied load, the compression zone will be wider.

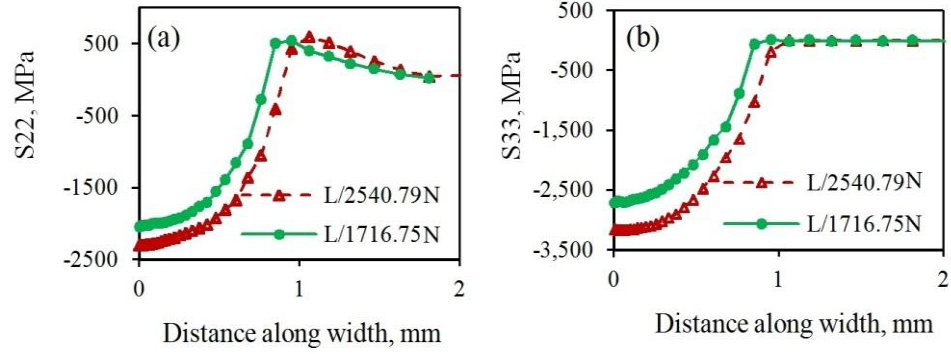


Fig. 3.10 (a) S22 stress and (b) S33 stress in width direction.

Fig. 3.11 (a) shows the subsurface shear stress contour (butterfly shape). This shear profile is symmetric with a change in sign at the center of contact. Fig. 3.11 (b-c) shows the cross-section shear stress contour inside the sample. This butterfly shape is a characteristic of rolling contact [9].

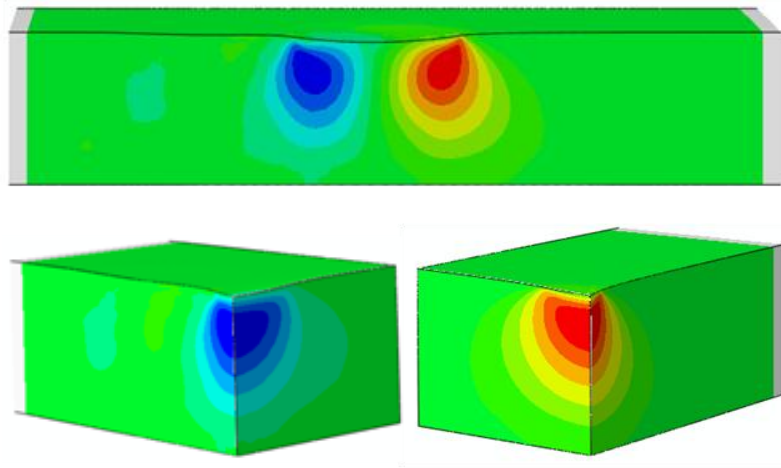


Fig. 3.11 3D contour of shear stress.

3.6.3 Residual Stress and Strain Profiles

The predicted residual Von Mises and S33 stress in depth direction are shown in Fig. 3.12(a) and (b). The S33 stress is tensile within the first 5 μm , then compressive residual stress is achieved. The maximum Von Mises stress occurs at 0.4 mm in subsurface and axial compressive residual stress occurs at around 1.0 mm in subsurface for loading case 1. The magnitude of the S33 residual stress in subsurface is 45.4 MPa for loading case 1 and 2.5 MPa for loading case 2. As expected, the Von Mises stress penetrates deeper in subsurface for the larger load.

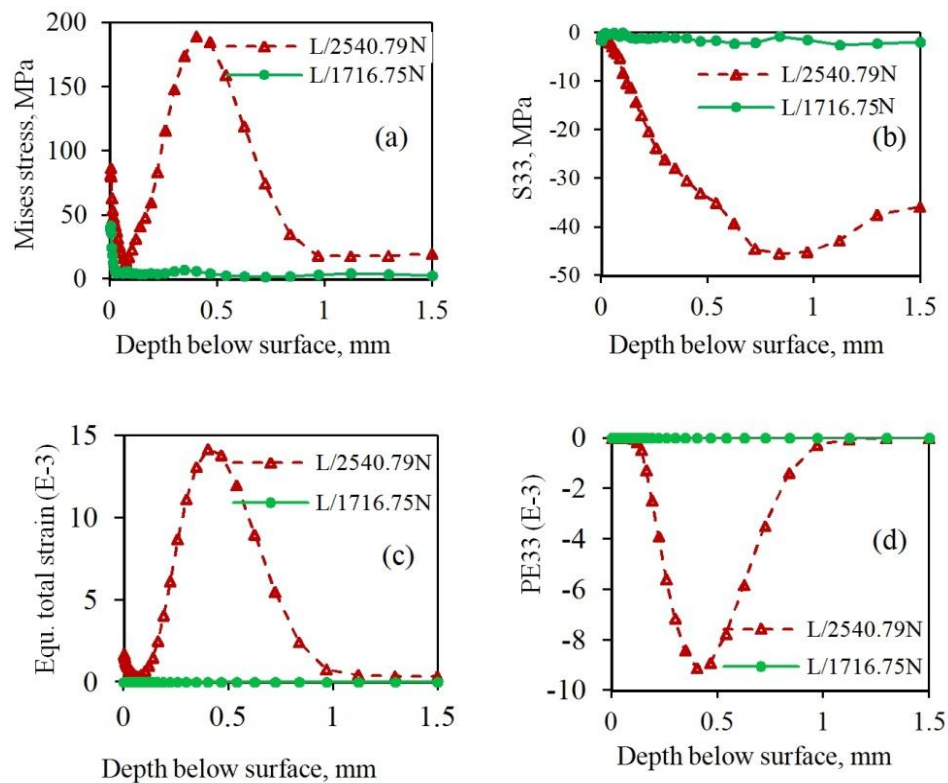


Fig. 3.12 Residual stress and strain profiles in subsurface.

The equivalent total strain and plastic strain PE33 in subsurface are shown in Fig. 3.12(c) and (d). It can be observed that a subsurface “plastic zone” from 0.1-1 mm below the surface for loading case 1. It can be inferred that with an increasing applied load, both the magnitude of residual strain and the width of the plastic zone will increase.

When comparing the depth of maximum S33 and PE33, it can be seen that the compressive residual stress depth is about two times deeper than the plastic residual strain in Fig. 3.13. This indicates that compressive residual stress in the deep subsurface is achieved with only a small amount of plastic deformation, which is a unique characteristic of LPB process.

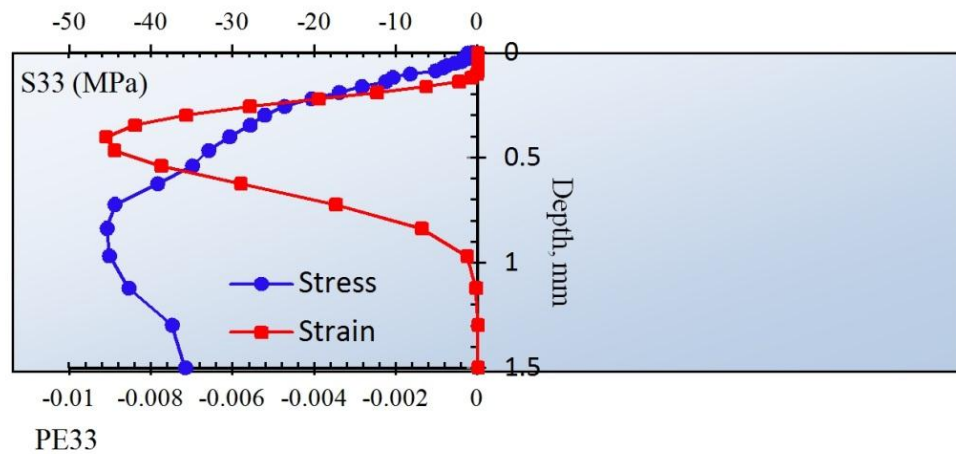


Fig. 3.13 Max. S33 and PE33 in the subsurface.

3.6.4 Convergence Analysis

In order to verify the stability of the simulation results, a convergence analysis was performed by changing element size. The element number changes from 90 to 472,628. The deformation at the rolling ending point was taken as Y-axis in Fig. 3.14. It is illustrated that as

the number of elements increases, the deformation value converges. The converged result occurs when the element number is over 67,202.

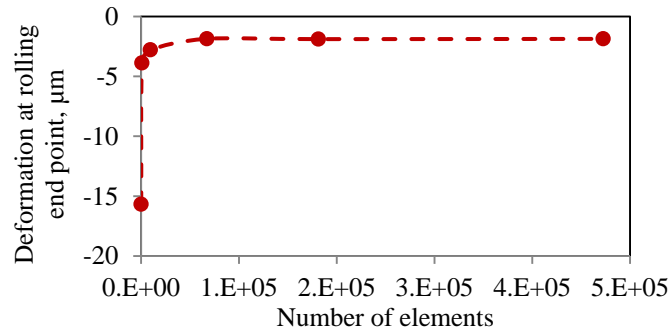


Fig. 3.14 Deformation at rolling end vs. element number.

3.7 Conclusions

LPB of SE508 Nitinol was performed to study the effect of burnishing pressures on material deformations. A 3D finite element simulation of LPB was also developed to understand burnishing mechanics. The results can be summarized as follows:

- When burnishing pressure increases from 4 MPa to 20 MPa, the depth of burnishing tracks change from 0.2 μm - 4.0 μm with a percent cold work from 0.01% - 0.2%, respectively.
- A large region of elastic spring back of this material could be found when compared to the theoretical deformation amount. The superelasticity property could be observed in this study.
- The predicted and measured profiles of the burnishing tracks are in good agreement. This suggests that the superelastic-plastic material model can successfully capture the non-linear behavior of SE508 Nitinol.

- In width direction, S22 stress changes from compression to tension along the path from the tool center and there exists a neutral point.
- When the applied load changed from 1716.75 N to 2540.79 N, the maximum axial compressive residual stress increased from 2.5 MPa to 45.4 MPa. As the load increases, both the depth and magnitude of residual stress will increase. This compressive residual stress is believed to have a beneficial effect on fatigue life.
- Compressive residual stress 45 MPa occurs at ~1.0 mm in subsurface, while compressive residual strain occurs at ~0.4 mm. Producing large compressive residual stress in the subsurface with a small amount of shallow deformation is the unique characteristic of LPB process, which can be predicted by the simulation model.

3.8 References

- [1] T. Duerig, A. Pelton, D. Stöckel, 1999, An overview of nitinol medical applications, *Materials Science and Engineering: A*, 273: 149-160.
- [2] A.R. Pelton, S.M. Russell, J. DiCello, 2003, The physical metallurgy of nitinol for medical applications, *JOM Journal of the Minerals, Metals and Materials Society*, 55(5): 33-37.
- [3] M. Bram, A. Ahmad-Khanlou, A. Heckmann, B. Fuchs, H. Buchkremer, D. Stöver, 2002, Powder metallurgical fabrication processes for NiTi shape memory alloy parts, *Materials Science and Engineering: A*, 337(1): 254-263.
- [4] V. Imbeni, C. Martini, D. Prandstraller, G. Poli, C. Trepanier, T. Duerig, 2003, Preliminary study of micro-scale abrasive wear of a NiTi shape memory alloy, *Wear*, 254(12): 1299-1306.
- [5] M. Es-Souni, M. Es-Souni, H. Fischer-Brandies, 2002, On the properties of two binary NiTi shape memory alloys. effects of surface finish on the corrosion behaviour and in vitro biocompatibility, *Biomaterials*, 23(14): 2887-2894.
- [6] R. Liu, D.Y. Li, 2001, Modification of archard's equation by taking account of elastic/pseudoelastic properties of materials, *Wear*, 251(1-12): 956-964.

- [7] A. Pelton, V. Schroeder, M. Mitchell, X. Gong, M. Barney, S. Robertson, 2008, Fatigue and durability of nitinol stents, *Journal of the mechanical behavior of biomedical materials*, 1(2): 153-164.
- [8] U.S. Food and Drug Administration. 2010. Non-clinical engineering tests and recommended labeling for intravascular stents and associated delivery systems.
- [9] M. El-Khabeery, M. El-Axir, 2001, Experimental techniques for studying the effects of milling roller-burnishing parameters on surface integrity, *International Journal of Machine Tools and Manufacture*, 41(12): 1705-1719.
- [10] C. Seemikeri, P. Brahmkar, S. Mahagaonkar, 2008, Investigations on surface integrity of AISI 1045 using LPB tool, *Tribology International*, 41(8): 724-734.
- [11] P.S. Prevéy, J.T. Cammett, 2004, The influence of surface enhancement by low plasticity burnishing on the corrosion fatigue performance of AA7075-T6, *International Journal of Fatigue*, 26(9): 975-982.
- [12] P.S. Prevéy, R.A. Ravindranath, M. Shepard, T. Gabb. 2003, ASME Turbo Expo 2003, collocated with the 2003 International Joint Power Generation Conference, 657-665.
- [13] P.S. Prevéy, N. Jayaraman, R.A. Ravindranath, M. Shepard. 2007, ASME Turbo Expo 2007: Power for Land, Sea, and Air, 61-69.
- [14] Y. Guo, M.E. Barkey, 2004, FE-simulation of the effects of machining-induced residual stress profile on rolling contact of hard machined components, *International Journal of Mechanical Sciences*, 46(3): 371-388.
- [15] M. Šraml, J. Flašker, I. Potrč, 2003, Numerical procedure for predicting the rolling contact fatigue crack initiation, *International Journal of Fatigue*, 25(7): 585-595.
- [16] M. Geetha, A. Singh, R. Asokamani, A. Gogia, 2009, Ti based biomaterials, the ultimate choice for orthopaedic implants—a review, *Progress in Materials Science*, 54(3): 397-425.
- [17] N. Morgan, 2004, Medical shape memory alloy applications—the market and its products, *Materials Science and Engineering: A*, 378(1): 16-23.
- [18] C. Seemikeri, P. Brahmkar, S. Mahagaonkar, 2008, Low plasticity burnishing: An innovative manufacturing method for biomedical applications, *Journal of Manufacturing Science and Engineering*, 130(2): 021008.
- [19] J. Greenwood, K. Johnson, E. Matsubara, 1984, A surface roughness parameter in hertz contact, *Wear*, 100(1): 47-57.
- [20] Johnson KL. 1987. *Contact mechanics*. Cambridge university press.

- [21] W. Yan, Q. Sun, X.Q. Feng, L. Qian, 2007, Analysis of spherical indentation of superelastic shape memory alloys, *International Journal of Solids and Structures*, 44(1): 1-17.
- [22] O. Bartier, X. Hernot, G. Mauvoisin, 2010, Theoretical and experimental analysis of contact radius for spherical indentation, *Mechanics of Materials*, 42(6): 640-656.
- [23] B. Taljat, G. Pharr, 2004, Development of pile-up during spherical indentation of elastic-plastic solids, *International Journal of Solids and Structures*, 41(14): 3891-3904.
- [24] A. Masud, M. Panahandeh, F. Aurricchio, 1997, A finite-strain finite element model for the pseudoelastic behavior of shape memory alloys, *Computer Methods in Applied Mechanics and Engineering*, 148(1): 23-37.
- [25] V. Brizmer, Y. Kligerman, I. Etsion, 2006, The effect of contact conditions and material properties on the elasticity terminus of a spherical contact, *International Journal of Solids and Structures*, 43(18): 5736-5749.
- [26] M. Knight, L. De Lacerda, L. Wrobel, J. Henshall, 2002, Parametric study of the contact stresses around spherical and cylindrical inclusions, *Computational materials science*, 25(1): 115-121.
- [27] X. Hernot, O. Bartier, Y. Bekouche, R. El Abdi, G. Mauvoisin, 2006, Influence of penetration depth and mechanical properties on contact radius determination for spherical indentation, *International Journal of Solids and Structures*, 43(14): 4136-4153.
- [28] W. Yan, Q. Sun, H. Liu, 2006, Spherical indentation hardness of shape memory alloys, *Materials Science and Engineering: A*, 425(1): 278-285.
- [29] SIMULIA, 2012, ABAQUS 6.12 documentation.

CHAPTER 4

A PREDICTIVE MODEL AND VALIDATION OF LASER CUTTING OF NITINOL WITH A NOVEL MOVING VOLUMETRIC PULSED HEAT FLUX

Abstract

Nitinol alloys are widely used in manufacturing of cardiovascular stents due to excellent biomechanical properties. Laser cutting is the predominant process for stent manufacturing. However, laser cutting induces thermal damage, such as heat affected zone (HAZ), micro cracks, and tensile residual stress, which detrimentally affect product performance. The important process features such as temperature distribution, stress development, and HAZ formation are critical to reduce thermal damage; however they are difficult to measure experimentally due to the highly transient process. To better understand the process mechanism in laser cutting of Nitinol, a 3-dimensional finite element model of pulsed laser cutting was developed. A novel thermal loading model with high spatial accuracy was developed to simulate a moving volumetric pulsed heat flux. A material subroutine was incorporated to model superelasticity and shape memory of Nitinol. The predicted kerf geometry and dimensions agreed well with experimental data. Also, the effects of cutting speed, pulse power, and pulse width on kerf profile, temperature, and heat affected zone (HAZ) were investigated.

In the superelasticity region of Fig. 4.1, Nitinol initially is in an austenitic state at the origin point O. With an applied stress, Nitinol is loaded along path $O \rightarrow E$, where a phase transformation from austenite to martensite and detwinning of martensite simultaneously occur. A large elastic strain up to 8% can be achieved. Upon unloading along path $E \rightarrow O$, the material transforms back to austenite, and the superelastic deformation is recovered demonstrating a hysteresis loop in the stress-strain diagram.

In the thermal shape memory region of Fig. 4.1, when Nitinol is cooled down along path $O \rightarrow A$ without applied stress below martensite finish temperature (M_f), complete austenite to martensite (twinned) transformation occurs. The material is plastically deformed through reorientation and detwinning of martensite along path $A \rightarrow B$. Then, unloading from $B \rightarrow C$ causes elastic unloading of the reoriented detwinned martensite and the material stays deformed. After heating above the austenite finish temperature (A_f), the material transforms from martensite to austenite and recovers the pseudoplastic deformation, thus “remembering” its previously defined shape.

Due to these excellent biomechanical properties, Nitinol has received considerable attention since its discovery in 1962 at the Naval Ordnance Laboratory. Many of the early applications of Nitinol focused on the shape memory effect. In recent years, a lot of attention has been aimed towards the superelasticity of Nitinol, with particular emphasis on biomedical applications [1]. A typical example is cardiovascular stents.

4.1.2 Laser Cutting of Nitinol

A stent is defined as a cylindrical medical device used to widen a narrow or stenosed lumen in order to maintain the patency of the lumen. A typical stent is shown in Fig. 4.2(a). Currently, stents are being increasingly used in blood vessels and gastrointestinal, renal, and biliary tracts [2]. There are many materials used in making stents such as stainless steel, cobalt-chromium, and Nitinol alloys. Nitinol is preferred because of its flexibility and ability to maintain shape in a curved lumen. Moreover, the non-linear mechanical response of Nitinol is similar to natural material, such as hair, bone, and tendon.

The machining challenges of Nitinol stents are manifested in two aspects: (i) stents are miniature devices that demand a very precise and complex meshed geometry; and (ii) Nitinol is very difficult to be shaped by mechanical cutting due to strong work hardening, excessive tool wear, and bur formation [3,4]. These technical hurdles can be overcome by laser cutting. A fine focused laser beam can produce a micrometer size kerf on Nitinol, and the non-contact thermal process can also eliminate pressing issues inherent in mechanical cutting.

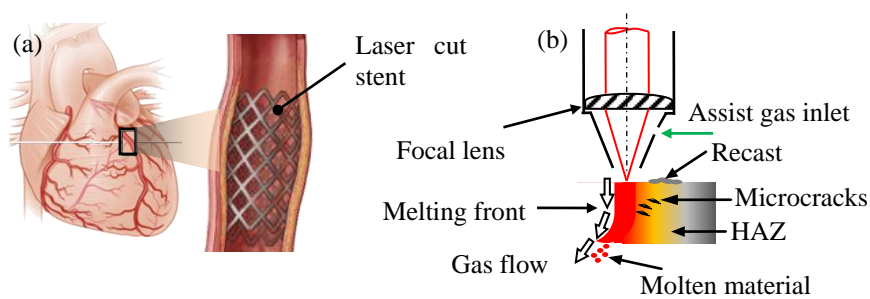


Fig. 4.2 (a) Cardiovascular Nitinol stent by laser cutting, (b) laser cutting schematic.

The fundamental mechanism of laser cutting is thermal heating (absorption and conduction), dynamic melting, and/or evaporating (phase transition and material removal) of the base material in the cut kerf [5,6]. A schematic of laser cutting is shown in Fig. 4.2(b). Molten material is expelled from the kerf by an assisting gas jet. Recast and dross forms when the molten and vaporized material re-solidifies. The heat diffused into the vicinity of the cut zone causes a heat affected zone (HAZ). In addition, microcracks are often formed by laser induced thermal stress [7].

4.1.3 Problem and Objectives

According to the guidance document of intravascular stents by U.S. Food and Drug Administration in 2010 [8], stent defects as a result of manufacturing flaw can contribute to clinical complications or even the failure of devices. The thermal damage from laser cutting can lead to a short fatigue life, decreased corrosion resistance, and failure after insertion. In order to prevent these defects, several post-processes, e.g. electropolishing and ultrasonic cleaning, are added to the manufacturing process chain. This leads to a rise in economic, social, and environmental costs. Therefore, it is important to better understand the laser cutting process and how to laser cut without generating thermal damage.

A few experimental studies were conducted to reduce HAZ in laser cutting of Nitinol [9,10]. However, a predictive model is highly needed to better understand the process mechanism. Such a model needs to consider three integral aspects: a thermal model representing the pulsed laser, a material model describing the unique stress-strain-temperature behavior of Nitinol, and a laser-material interaction model that accounts for the transient thermomechanical phenomena at the cut kerf. However little has been done to systematically integrate a realistic

thermal model with the temperature and stress dependent dynamic phase transformation of Nitinol material to model the thermomechanical behavior in laser cutting process.

To solve these pressing issues, the objectives of this study are to: (i) develop a new thermal model of a laser; (ii) develop a physics-based approach simulating Nitinol superelasticity and thermal shape memory; (iii) predict kerf profile, HAZ, and process characteristics in laser cutting; and (iv) validate the predictions with experimental data.

4.2 Heat Flux Modeling in Laser Cutting

Important process features in laser cutting such as temperature distribution, stress propagation, and HAZ formation are directly related to cutting quality. However, they are difficult to measure experimentally since laser cutting is a highly transient process. Therefore, finite element simulation was used intensively to gain insight into the process. Simulations have been used to aid in determining accurate thermal loading, verifying experimental data, and predicting temperature and residual stress profiles.

An accurate thermal model is critical to simulate the laser cutting process. Representative heat flux models with different features are summarized in [Table 4.1](#). The most commonly used heat flux model has the form of

$$I = \frac{AP}{\pi r_0^2} \exp\left[-B \left(\frac{r}{r_0}\right)^2\right] \quad 4.1$$

where I is the laser intensity, A is the laser absorption coefficient, P is the laser power, r_0 is the spot radius, B is the shape factor of the Gaussian distributed heat flux, and r is the distance to beam center. Examples of finite element models that used this formula can be found in

[11,12,13] (Table 4.1). Yang et al. [11] used this type of heat flux model to simulate laser assisted machining. The heat flux model accurately predicted the temperature and HAZ. Lee [12] used a similar heat flux model to predict the temperature field and the cutting profile. The machined slot had a thickness of approximately 0.5 mm. It was found that this heat flux can effectively predict the kerf profile, temperature, and stress distribution. This type of heat flux was also adopted by Neela et al. [13] to predict temperature field in laser-engineered net shaping process. It was found that the predicted temperature on the top surface matched experimental data.

Different geometrical shapes of heat flux were explored by many researchers [14,15,16,17,18,19,20]. It was shown that a volumetric (3D) heat flux has advantages over a surface (2D) heat flux in predicting the thermal response of the material during laser processing. Moreover, previous works have shown that laser beam absorption not only happens at the workpiece surface, but also at the cylindrical melting front [21,22]. Therefore, researchers proposed different forms of volumetric heat flux to simulate laser processing in different applications. Yilbas et al. [15] simulate laser cutting of thick sheet metal using a volumetric thermal model. The stress field and temperature field were predicted and found to be in agreement with experimental observation. Shuja et al. [18] used a similar volumetric heat flux to simulate laser heating of a moving slab, and it was found that predicted melt thickness agreed with experimental measurements. Lacki et al. [14] stated that the advantage of a conical volumetric heat flux versus a surface heat flux was that it better captured the shape of the thermal field in deep welds during laser melting. Luo et al. [19] and Zain-UI-Abdein et al. [20] found that the use of a conical shape heat flux better simulated the laser-material interaction with high penetration depth.

Table 4.1 Representative Heat Flux Models

Heat flux types	Heat flux equations	Notes	Ref.
Surface (2D) heat flux	$q(x, y) = \frac{2P}{\pi b^2} \exp\left(-2 \frac{x^2 + y^2}{b^2}\right)$	2D Gaussian distribution of surface heat flux	[11]
	$I(x, y) = a(x, y) \frac{P}{R^2} \exp\left(-\frac{x^2 + y^2}{R^2}\right)$	2D Gaussian distribution of surface intensity, absorptivity included	[12]
	$q = \frac{P\eta d}{\pi r_{lb}^2} \exp\left(-\frac{dr^2}{r_{lb}^2}\right)$	2D Gaussian distribution of surface heat flux, beam distribution parameter included	[13]
	$I_l(x, y) = \frac{(1-R)P}{\pi w l} \exp\left(-\frac{x'^2}{w^2} + \frac{y'^2}{l^2}\right)$	Elliptical laser intensity	[17]
Volumetric (3D) heat flux	$S_0 = I_0 \delta(1 - r_f) \exp(-\delta z) \exp\left(-x^2 + \frac{z^2}{a^2}\right)$	Volumetric heat source, absorption depth, Gaussian parameter included	[15]
	$S_0 = I_0 \delta(1 - r_f) \exp(-\delta z) \exp\left[-\left(\frac{r}{a} + \beta\right)^2\right] f(t)$	Volumetric heat source, absorption depth, density parameter included	[18]
Conical (3D) heat flux	$q_v(x, y, z) = \frac{9Q_v}{\pi h r_0^2} \exp\left[-\frac{h^2}{(h-z)^2} \cdot 3 \frac{(x^2 + y^2)}{r_0^2}\right]$	Conical shape volumetric heat flux for high penetration depth	[19]
	$Q_v = \frac{9\eta P}{\pi(1 - e^{-3})(z_e - z_i)(r_e^2 + r_e r_i + r_i^2)} \exp\left(-\frac{3r^2}{r_c^2}\right)$ $r_c = r_i + (r_e - r_i) \cdot \frac{(z - z_i)}{(z_e - z_i)}$	Conical shape volumetric heat flux, distribution parameter of cone as a function of depth included	[20]
Surface (2D) heat flux of pulse laser	$I = I_0 f(r) f(t)$ $f(r) = \exp\left[-2 \frac{(x - vt)^2}{r_0^2}\right]$ $f(t) = \begin{cases} 1, & 0 \leq t \leq t_p \\ 0, & t_p < t \leq nT_t \end{cases}$	Surface heat flux, time function used to simulate laser modulation	[23]

$$\phi(x, y) = I_s(x, y) \int_0^{\Delta t} f(t) dt$$

$$f_N(t) = \sum_{k=0}^{N-1} f(t - kT), \text{ where } T = \frac{1}{\nu}$$

$$b_N(t) = \sum_{k=0}^{N-1} \theta(t - kT) - \theta(t - NT - \tau)$$

The laser fluence of pulses was simulated using time function [24]

Pulsed laser operation is a key feature for current laser cutting processes. Different pulse duration times and repetition rates significantly affect surface roughness [25,26] and residual stress [27]. Therefore, it is critical to incorporate the pulsed laser operation in modeling of heat flux. Xuan et al. [23] simulated a pulsed laser by using a time function to turn on and off the laser based on pulse duration. Kong et al. [24] simulated the pulsed laser in generating 3D surface texture. The validation trials showed that the maximum error in predicted surface texture was 9% as compared to experiments.

HAZ is the material zone in the subsurface for which the microstructure and properties have been altered by intensive thermal loading. The thickness of HAZ is a critical surface integrity factor to determine the cutting performance, especially in stents that are prone to thermal damage. The prediction of HAZ using finite element method is important since a parametric study can help select optimal process parameters to minimize HAZ. Singh et al. [28] used a 3D moving heat source to predict the thickness of HAZ during laser heating. A critical temperature was used as the criteria for the HAZ formation. It was verified experimentally that when material exceeds the critical temperature, the hardness of the material drops, indicating the formation of a HAZ.

Although these simulation works have explored laser processing on different materials using different thermal modeling techniques, there is still little theoretical modeling of a moving

volumetric heat flux by a pulsed laser. A simulation using a 3D moving heat flux in pulsed mode on Nitinol is essential to improve the fundamental understanding of process mechanisms and the influence of process parameters.

4.3 Simulation Procedure

4.3.1 Mesh

The mesh design is shown in [Fig. 4.3](#). The dimensions of the workpiece were 6 mm (length) \times 3 mm (width) \times 1 mm (thickness). The laser cutting direction was along the X-axis. Element size was biased with a higher density of elements along the cutting direction (X-axis). Within the fine mesh in the analysis zone, the element size was 50 μm \times 50 μm \times 10 μm . The boundary condition on the Y-Z plane was fixed to provide proper constraint of the workpiece. The initial temperature was room temperature (20 °C).

The simulation was performed using Abaqus/Standard since the moving heat flux subroutine DFLUX can only be programmed with the implicit solver. The advantage of using the implicit solver was that the temporal discretization was more stable despite a certain reduction in computational efficiency. In order to determine the temperature and stress distribution after laser cutting, a coupled thermal-mechanical analysis was used. The laser cutting process was based on 3-D transient heat transfer.

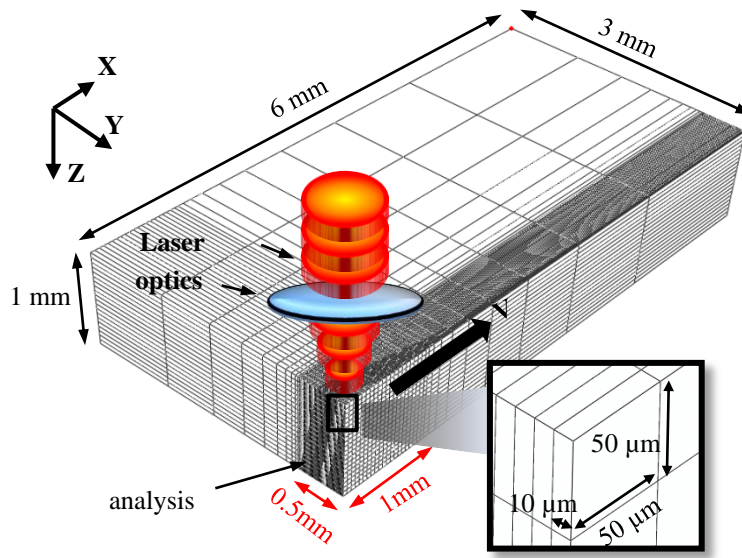


Fig. 4.3 Simulation schematic of pulsed laser cutting.

4.3.2 Modeling of Moving Volumetric (3D) Heat Flux of Pulse Laser

In order to understand the laser cutting process from a theoretical perspective, a schematic of 3D heat flux is shown in Fig. 4.4. When laser pulses hit the top surface, volumetric heat absorption happens. The kerf tapers since more erosion takes place at the top surface than at the bottom. The taper can also be attributed to the intensity decay in the thickness direction due to defocusing of the laser beam. The conical shape volumetric heat flux moves along the workpiece to generate a cutting kerf and form a heat affected zone (HAZ) on both entrance and exit sides of the kerf.

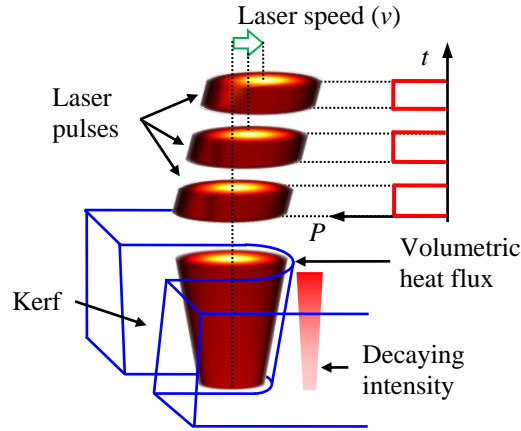


Fig. 4.4 Schematic of the moving volumetric heat flux of pulsed laser.

To simulate the characteristics of the heat flux of laser pulses, a DFLUX user subroutine of conical shape volumetric heat flux was developed. The subroutine featured (1) a moving Gaussian heat flux from laser, (2) a pulsed operation, and (3) a conical volumetric (3D) heat flux.

Fig. 4.5 illustrates the modeling procedure for a moving volumetric heat flux of a pulsed laser. The first step is to define modulated laser power as a function of laser frequency (f), ratio (m) of period ($1/f$) to pulse width (τ), and time (t). The laser pulse shape is assumed to be perfectly rectangular. Laser power (P) is equal to peak power (P_{peak}) during the pulse width. When there is no pulse within one period, P is set to zero. N is an integer that represents the N^{th} period.

The second step is to define the volumetric heat flux. The peak heat flux is determined by the absorption coefficient (A), the time dependent laser power (P), laser spot radius (R_0) on the top surface, and sample thickness (h). Gaussian distribution is applied throughout the sample thickness. The instantaneous laser spot radius (r) is a function of depth (z) and decreases in the thickness direction due to decaying intensity. A decay coefficient (D) is defined to accommodate the conical shape of the volumetric heat flux.

The third step is to define the location of a moving laser as a function of cutting speed (v). The last step is the implementation of the previous three steps via a thermal loading subroutine DFLUX. The DFLUX codes first read in the node coordinates (x, y, z) of the mesh and simulation time (t). Then, the interaction between laser pulses, the volumetric heat flux, and laser movement were taken into account. The novelty of the modeling procedure has two aspects: first, it integrates moving laser pulses with realistic volumetric heat flux to provide more accurate spatial thermal loading; second, it is a versatile approach since only the process parameters need to be defined.

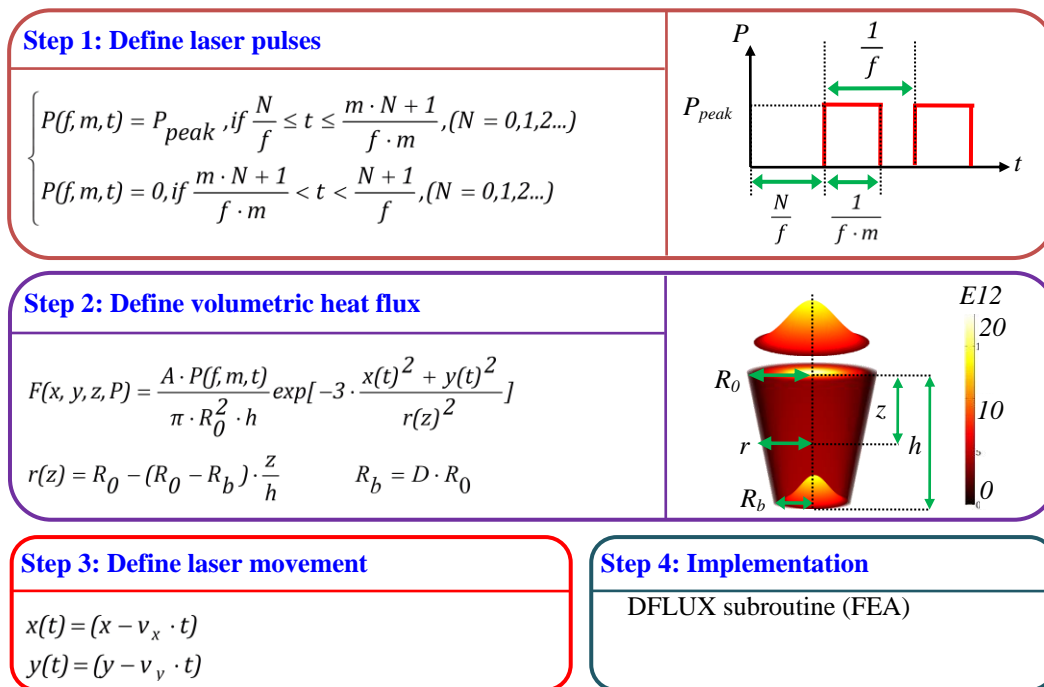


Fig. 4.5 Modeling procedure of moving volumetric heat flux of pulsed laser.

4.3.3 Simulation Conditions

The simulation conditions are listed in [Table 4.2](#). The design-of-experiment (DOE) simulation was a sensitivity analysis to determine the effects of cutting speed (cases 1-3), peak pulse power (cases 4-6), and pulse width (cases 7-9). The detailed laser pulse shape for simulation cases 7, 8, and 9 are shown in [Fig. 4.6](#). In cases 7-9, the average power was 80 W. The average power (P) and the pulse energy (E) were calculated by

$$P = P_0 \times \tau \times f \quad 4.2$$

$$E = P_0 \times \tau \quad 4.3$$

where P is the average power, P_0 is the peak pulse power, τ is the pulse width, f is the laser frequency, and E is the pulse energy.

[Table 4.2](#) Simulation Conditions

Case #	Peak pulse power (W)	Pulse width (ms)	Frequency (Hz)	Cutting speed (mm/s)	Avg power (W)	Pulse energy (J)
1	1600	0.5	100	2	80	0.8
2	1600	0.5	100	5	80	0.8
3	1600	0.5	100	8	80	0.8
4	1000	0.5	100	5	50	0.5
5	1600	0.5	100	5	80	0.8
6	2000	0.5	100	5	100	1.0
7	800	1.0	100	1.7	80	0.8
8	1600	0.5	100	1.7	80	0.8
9	4000	0.2	100	1.7	80	0.8

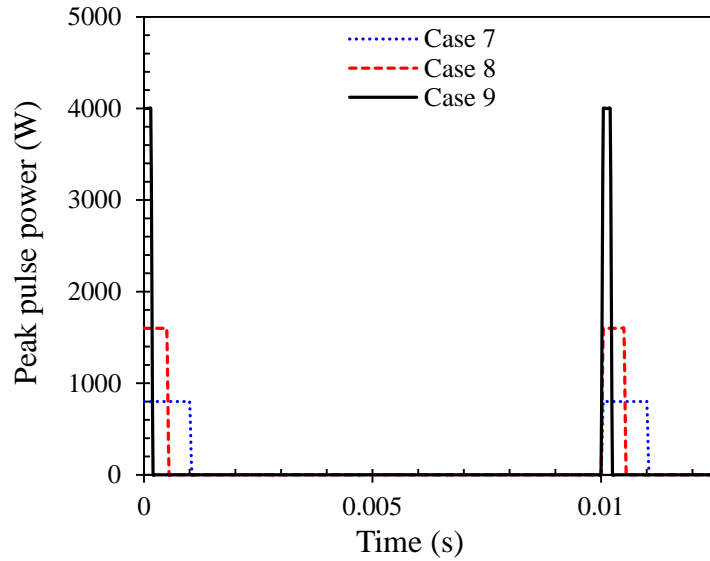


Fig. 4.6 Laser pulse shape for simulation cases 7, 8, and 9.

The laser frequency was 100 Hz, the laser spot radius on the top surface was 300 μm , and the top-to-bottom ratio of the heat flux diameter was determined by the entry-to-exit kerf width ratio in the experimental work in Ref. [25].

The key assumptions within this finite element model are as follows:

- The total energy absorption coefficient was assumed to be constant at 0.8.
- The heat generated inside the workpiece due to conductivity was small compared to the heat generated by the heat flux.
- When the temperature of the element exceeded the melting temperature, the element remained in the mesh. These elements were removed in post-processing in order to predict the kerf width.

4.4 Modeling of Nitinol Superelasticity and Shape Memory

4.4.1 Mechanical Behavior

For superelastic Nitinol, material is in an austenitic state at low stress level. Further mechanical loading will induce phase transformation from austenite to martensite. Large elastic deformation can be achieved. When unloading the material, a non-linear hysteresis loop will occur.

To model the unique thermomechanical behavior of Nitinol, a material user subroutine UMAT was used [29]. This material model was built upon the generalized plasticity [30] and thermomechanical continuum theory [31]. The constitutive equations can be written as:

$$\varepsilon = \varepsilon^{el} + \varepsilon^{tr} \quad 4.4$$

$$\varepsilon^{tr} = \varepsilon^L \xi_s \quad 4.5$$

$$F^{AS}(\tau, T) = ||t|| + 3\alpha p - C^{AS}T \quad 4.6$$

$$\Delta \xi_s^{AS} = H^{AS} \beta^{AS} (1 - \xi_s) \frac{\dot{F}^{AS}}{(F_f^{AS})^2} \quad 4.7$$

$$H^{AS} = \begin{cases} 1, & \text{if } F_s^{AS} > 0, F_f^{AS} < 0, \dot{F}^{AS} > 0 \\ 0, & \text{otherwise} \end{cases} \quad 4.8$$

In the elastic region, the total strain (ε) consists of two parts: elastic strain (ε^{el}) and transformation strain (ε^{tr}) as shown in Eq. 4.4. The second-order tensor transformation strain is determined by a multiplicative of the maximum residual strain (ε^L) and the fraction (ξ_s) of martensite created under loading. To model the temperature and pressure dependent phase transformation, a Drucker-Prager type loading function is given by Eq. 4.6. The fraction of martensite present in the material determines the actual stress level under loading. The change in

martensite fraction during the different transformation regions is calculated by [Eq. 4.7](#), where H^{AS} denotes the condition for conversion of austenite into martensite during stress evolution. Note that [Eqs. 4.4-4.8](#) only account for the austenite to martensite transformation. However, the same principle can be applied to define the reverse transformation.

[Fig. 4.7](#) shows the material parameters used to define the mechanical behavior used in the user-defined material model [29]. The material constants were based on a curve fitting process between a quasi-static stress strain curve from Split-Hopkinson Pressure Bar tests and the given theoretical model [32] under the assumption that tension and compression curves were symmetric with each other. The material constants are listed in [Table 4.3](#). In a previous research [32], these material constants successfully captured the superelastic-plastic mechanical behavior of Nitinol.

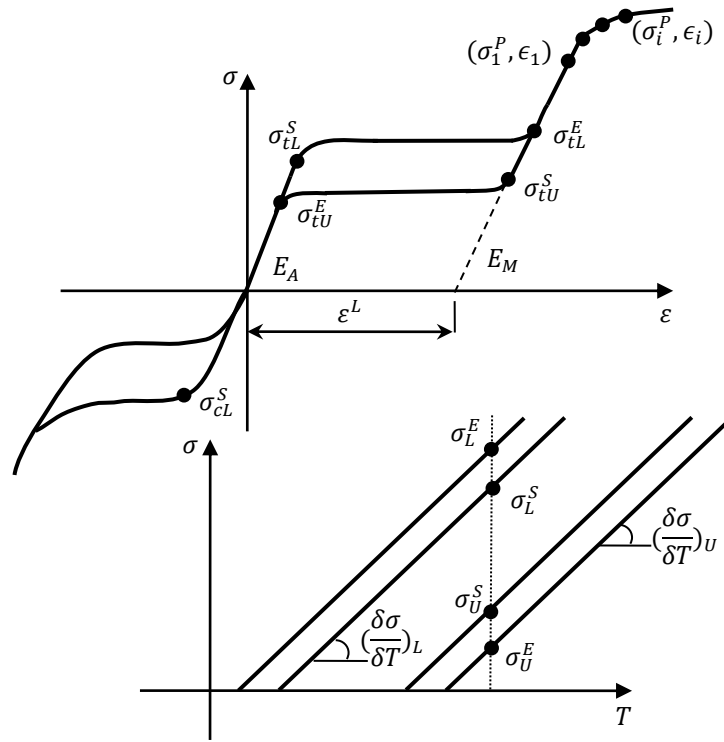


Fig. 4.7 Superelastic-plastic characteristics of Nitinol [29].

Table 4.3 UMAT Material Constants of Nitinol

Material parameter	Material Constant	Material Parameter	Material Constant		
E_a (Pa)	4.23E10	σ_3^p (Pa)	1.990E9	E_a	Austenite elasticity
V_a	0.3	ε_3	0.070	V_a	Austenite Poisson's ratio
E_m (Pa)	4.29E10	σ_4^p (Pa)	2.088E9	E_m	Martensite elasticity
V_m	0.3	ε_4	0.077	V_m	Martensite Poisson's ratio
ε^L	0.02	σ_5^p (Pa)	2.155E9	ε^L	Transformation strain
$(\frac{\delta\sigma}{\delta T})_L$	0	ε_5	0.084	$(\frac{\delta\sigma}{\delta T})_L$	$(\frac{\delta\sigma}{\delta T})$ loading
σ_L^S (Pa)	6.00E8	σ_6^p (Pa)	2.203E9	σ_L^S	Start of transformation loading
σ_L^E (Pa)	1.20E9	ε_6	0.091	σ_L^E	End of transformation loading
T_0 (°C)	22	σ_7^p (Pa)	2.424E9	T_0	Reference temperature
$(\frac{\delta\sigma}{\delta T})_U$	0	ε_7	0.098	$(\frac{\delta\sigma}{\delta T})_U$	$(\frac{\delta\sigma}{\delta T})$ unloading
σ_U^S (Pa)	5.00E8	σ_8^p (Pa)	2.275E9	σ_U^S	Start of transformation unloading
σ_U^E (Pa)	2.00E8	ε_8	0.105	σ_U^E	End of transformation unloading
σ_{cL}^S (Pa)	6.00E8	σ_9^p (Pa)	2.302E9	σ_{cL}^S	Start of transformation stress during loading in compression, as a positive value
ε_V^L	0.02	ε_9	0.112	ε_V^L	Volumetric transformation strain
N_p	11	σ_{10}^p (Pa)	2.325E9	N_p	Number of stress-strain pairs to define yield curve
σ_1^p (Pa)	1.556E9	ε_{10}	0.119	$\sigma_1^p, \varepsilon_1, \dots, \sigma_{11}^p, \varepsilon_{11}$	Stress-strain points in the yield curve
ε_1	0.056	σ_{11}^p (Pa)	2.343E9		
σ_2^p (Pa)	1.825E9	ε_{11}	0.126		
ε_2	0.063				

4.4.2 Physical Properties

The physical properties of Nitinol are listed in [Table 4.4](#). Since temperature dependent material properties were not available, all the physical properties were treated as temperature independent and isotropic in the simulations.

Table 4.4 Physical Properties of Nitinol

Density (kg/m ³)	6500
Melting point (°C)	1250
Specific heat (J/kg °C)	490
Conductivity (W/m °C)	14
Thermal expansion (m/°C)	11E-6

4.5 Results and Discussion

4.5.1 Prediction and Validation of Kerf Geometry

Fig. 4.8(a) shows the representative predicted kerf geometry with transient temperature contour. The FEA model predicted the important kerf characteristics in laser cutting, namely, taper and HAZ. Moreover, the predicted surface striation in Fig. 4.8(b) was similar to the striation pattern on the machined surface [25] under similar conditions. Therefore, kerf geometry, HAZ, and surface characteristics can be successfully predicted by the proposed modeling approaches of thermal loading and Nitinol properties.

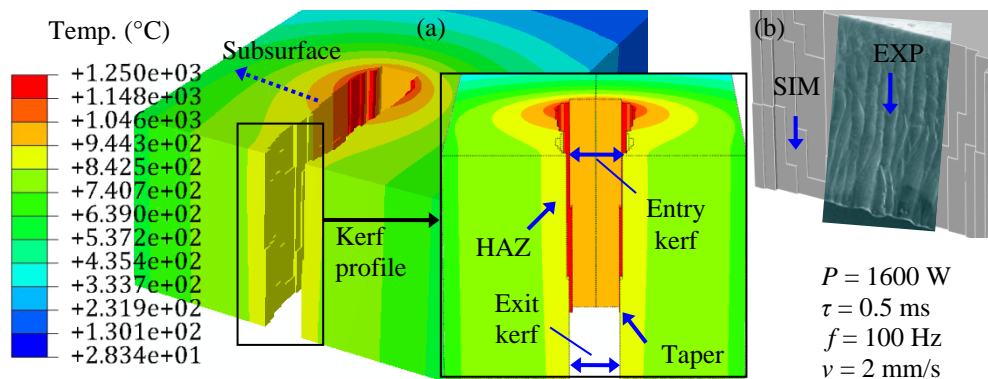


Fig. 4.8 (a) Representative prediction of laser cut kerf and (b) comparison between predicted and measured striated surfaces.

To validate the predicted dimensions of kerf geometry by laser cutting under different conditions, the predicted widths of entry kerf and exit kerf were compared with experimental data [25] under the same conditions. As shown in Fig. 4.9(a), predicted kerf widths agreed with experimental data reasonably well at all conditions. The discrepancy between the predicted and measured data can be attributed to measurement errors and FEA modeling error sources. The influence of temperature on Nitinol physical and thermal properties may also contribute to the discrepancy.

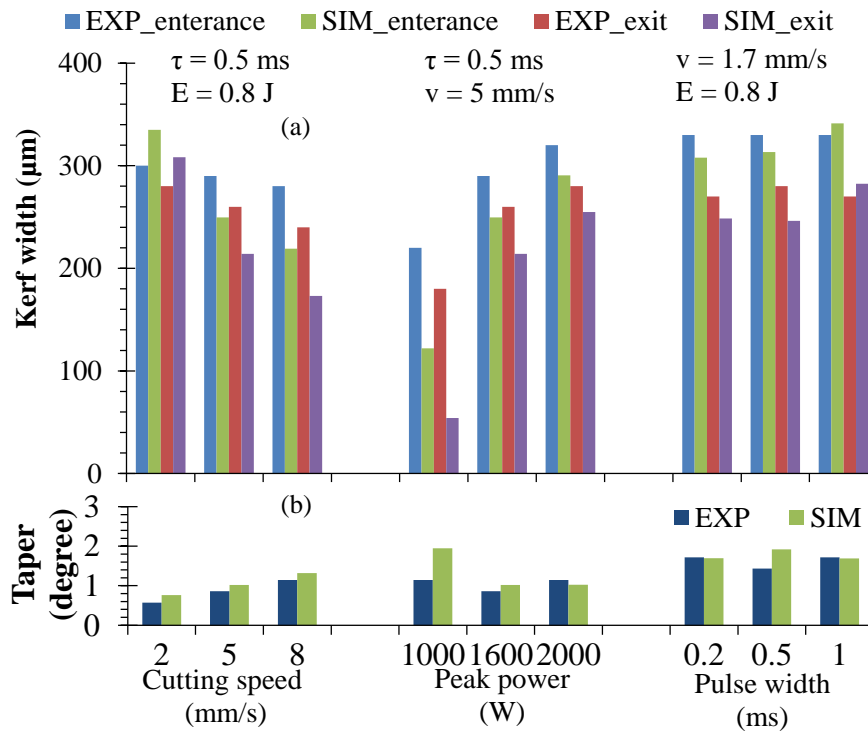


Fig. 4.9 The effect of cutting speed, peak power, and pulse width on (a) kerf width and (b) taper.

As indicated in Fig. 4.9(a), the kerf width can be significantly affected by cutting speed and peak power. As the cutting speed increased from 2 mm/s to 8 mm/s, the kerf width decreased. A peak power rise from 1000 W to 2000 W increased the kerf width. This was due to the fact that at low cutting speed and high peak power, energy input per unit volume was higher. As a result, the heat penetration became much deeper and was accompanied by a more intensive material melting. It was also found that pulse width did not have a significant impact on kerf width. At conditions considered in this study, the pulse width can be categorized into long pulse regime [33]. Within long pulse regime, the thermalization is dominated by thermal diffusion rather than plasma formation and explosions that occur in ultrashort pulse regime. Hence, the total energy input rather than pulse width dependent ultrafast phenomenon would determine the kerf dimensions.

Taper is another characteristic of kerf by laser cutting. The taper angle (α) can be calculated by:

$$\alpha = \tan^{-1} \frac{d_{entry} - d_{exit}}{2h} \quad 4.9$$

where d_{entry} and d_{exit} are the width of entry kerf and exit kerf, respectively. As shown in Fig. 4.9(b), the predicted taper can be reduced by decreasing cutting speed and increasing peak power, which was verified with reasonable accuracy by experimental data. Since non-uniform erosion and laser intensity decay in the thickness direction dominate the taper formation, a higher energy input per unit volume led to a more uniform thermal diffusion, and thus creates a smaller taper. In addition, pulse widths for the cases in this study did not affect taper formation.

4.5.2 Laser Cutting Temperature and Stress Development

Laser cutting temperature and stress development are the root causes for HAZ formation and part distortion, respectively. However, they are extremely difficult to measure experimentally due to their transient nature and small size. The predicted transient temperature in the subsurface is shown in Fig. 4.10(a). At a high cutting speed of 8 mm/s, a steep temperature gradient was produced. This was because higher cutting speed limits thermal diffusion time which results in less temperature rise in the subsurface. The temperature distribution was similar at all peak power levels in the subsurface zone of 80 μm . Beyond this depth, the temperature distributions were significantly different. It indicates that peak power influences the temperature distribution in the deep subsurface while having little or no effect near the top surface. Pulse widths were found to have little effect on the temperature distribution in the subsurface.

The predicted transient effective stress profiles in the subsurface are shown in Fig. 4.10(b). The maximum stress occurred on the cut surface with a magnitude of 520 MPa, 440 MPa, and 400 MPa at a cutting speed of 2 mm/s, 5 mm/s, and 8 mm/s, respectively. The slower cutting speed allowed more heat conduction into the workpiece, which generated more thermal expansion and led to high stress. At the highest laser peak power (2000 W), the maximum stress occurred on the top surface, while the lowest peak power (1000 W) produced the maximum stress in the subsurface. The predicted stress profile at the cutting speed of 8 mm/s provides a transition case of maximum stress from surface to subsurface, which suggests that the location of maximum stress was directly controlled by total energy input per unit volume. Lower energy shifted the maximum stress from the top surface to the subsurface. The shortest pulse width (0.2 ms), i.e. highest peak power, induced a localized stress concentration which generated the highest stress magnitude on the surface. The predicted stress at all simulation conditions was

still much lower than the yield strength (2 GPa) of Nitinol. Therefore, it can be inferred that there is no plastic distortion for these cases.

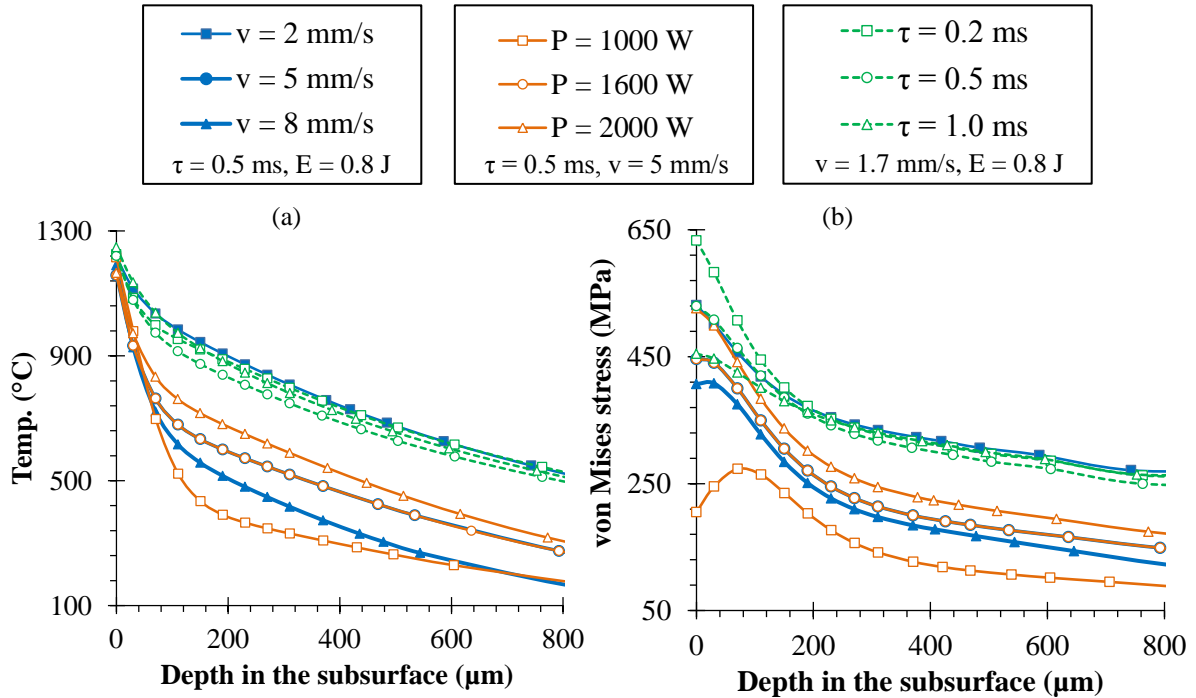


Fig. 4.10 The effects of cutting speed, peak power, and pulse width on (a) temperature and (b) stress in the subsurface.

4.5.3 Heat Affected Zone (HAZ)

It has been suggested that HAZ formation is directly controlled by temperature distribution [7], and therefore, HAZ thickness may be estimated based on a critical temperature. Based on a binary phase diagram of Nitinol, the critical temperature used is the solidus temperature (1025 °C). The predicted HAZ thickness is shown in Fig. 4.11. The predicted HAZ thickness is in the range of the measured HAZ thickness (<100 μm) [25].

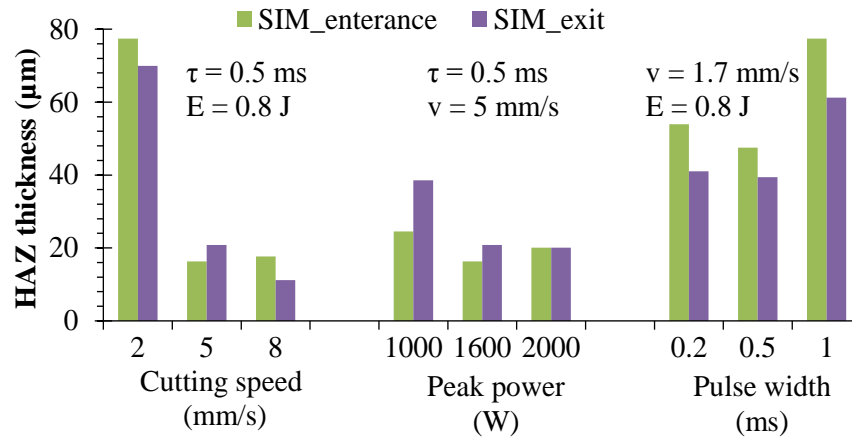


Fig. 4.11 The effect of cutting speed, peak power, and pulse width on HAZ thickness.

Fig. 4.11 also shows that low cutting speeds generate thick HAZ; this is due to excessive heat input into the workpiece. It is also noted that increasing peak power does not necessarily increase HAZ thickness. This agrees with the finding in section 5.2 that temperature distributions are similar at all peak power levels in the near subsurface. Therefore, HAZ was only slightly affected by peak power. Furthermore, the influence of pulse width on HAZ was not significant at the given laser cutting conditions.

4.6 Conclusions

This study focuses on the development of a predictive model for cutting of Nitinol using a pulsed laser. The predictions of kerf geometry and HAZ were verified by experimental data. Key findings are as follows:

- A new model of a moving volumetric heat flux by a pulsed laser has been developed with high spatial accuracy of thermal loading.
- A physics-based material user subroutine has been incorporated to simulate superelasticity and thermal shape memory of Nitinol.

- The characteristics of kerf width and taper were predicted and verified with reasonable accuracy by experimental data. Kerf width can be narrowed by increasing cutting speed and decreasing peak power, while taper can be reduced by decreasing cutting speed and increasing peak power.
- High cutting speed and low peak power not only lead to a steep temperature gradient in near subsurface, but also shift the maximum effective stress from top surface to the subsurface. Pulse width only affects stress distribution in near subsurface.
- Compared to peak power and pulse width, laser cutting speed is the deterministic factor for HAZ thickness.

4.7 References

- [1] T. Duerig, A. Pelton, D. Stöckel, 1999, An overview of nitinol medical applications, *Materials Science and Engineering: A*, 273: 149-160.
- [2] H.J. Chun, E.S. Kim, J.J. Hyun, Y.D. Kwon, B. Keum, C.D. Kim, 2010, Gastrointestinal and biliary stents, *Journal of gastroenterology and hepatology*, 25(2): 234-243.
- [3] K. Weinert, V. Petzoldt, D. Kötter, 2004, Turning and drilling of NiTi shape memory alloys, *CIRP Annals - Manufacturing Technology*, 53(1): 65-68.
- [4] Y. Guo, A. Klink, C. Fu, J. Snyder, 2013, Machinability and surface integrity of nitinol shape memory alloy, *CIRP Annals - Manufacturing Technology*, 62(1): 83-86.
- [5] F.O. Olsen, L. Alting, 1989, Cutting front formation in laser cutting, *CIRP Annals - Manufacturing Technology*, 38(1): 215-218.
- [6] A. Otto, H. Koch, K. Leitz, M. Schmidt, 2011, Numerical simulations - A versatile approach for better understanding dynamics in laser material processing, *Physics Procedia*, 12, Part A(0): 11-20.
- [7] H.K. Tönshoff, C. Emmelmann, 1989, Laser cutting of advanced ceramics, *CIRP Annals - Manufacturing Technology*, 38(1): 219-222.

- [8] U.S. Food and Drug Administration. 2010. Non-clinical engineering tests and recommended labeling for intravascular stents and associated delivery systems.
- [9] H. Huang, H. Zheng, G. Lim, 2004, Femtosecond laser machining characteristics of nitinol, *Applied Surface Science*, 228(1): 201-206.
- [10] N. Muhammad, L. Li, 2012, Underwater femtosecond laser micromachining of thin nitinol tubes for medical coronary stent manufacture, *Applied Physics A: Materials Science & Processing*, 107(4): 849-861.
- [11] J. Yang, S. Sun, M. Brandt, W. Yan, 2010, Experimental investigation and 3D finite element prediction of the heat affected zone during laser assisted machining of Ti6Al4V alloy, *Journal of Materials Processing Technology*, 210(15): 2215-2222.
- [12] S.H. Lee, 2000, Analysis of precision deburring using a laser—An experimental study and FEM simulation, *KSME international journal*, 14(2): 141-151.
- [13] V. Neela, A. De, 2009, Three-dimensional heat transfer analysis of LENSTM process using finite element method, *The International Journal of Advanced Manufacturing Technology*, 45(9-10): 935-943.
- [14] P. Lacki, K. Adamus, 2011, Numerical simulation of the electron beam welding process, *Computers & Structures*, 89(11): 977-985.
- [15] B.S. Yilbas, A.F.M. Arif, B.J.A. Aleem, 2009, Laser cutting of holes in thick sheet metals: Development of stress field, *Optics and Lasers in Engineering*, 47(9): 909-916.
- [16] J.F. Li, L. Li, F.H. Stott, 2004, Comparison of volumetric and surface heating sources in the modeling of laser melting of ceramic materials, *International Journal of Heat and Mass Transfer*, 47(6-7): 1159-1174.
- [17] Y. Wang, J. Lin, 2007, Characterization of the laser cleaving on glass sheets with a line-shape laser beam, *Optics & Laser Technology*, 39(5): 892-899.
- [18] S. Shuja, B. Yilbas, O. Momin, 2011, Laser heating of a moving slab: Influence of laser intensity parameter and scanning speed on temperature field and melt size, *Optics and Lasers in Engineering*, 49(2): 265-272.
- [19] Y. Luo, G. You, H. Ye, J. Liu, 2010, Simulation on welding thermal effect of AZ61 magnesium alloy based on three-dimensional modeling of vacuum electron beam welding heat source, *Vacuum*, 84(7): 890-895.
- [20] M. Zain-Ul-Abdein, D. Nélias, J.F. Jullien, D. Deloison, 2010, Experimental investigation and finite element simulation of laser beam welding induced residual stresses and distortions in thin sheets of AA 6056-T4, *Materials Science and Engineering: A*, 527(12): 3025-3039.

- [21] H. Kaebernick, D. Bicleanu, M. Brandt, 1999, Theoretical and experimental investigation of pulsed laser cutting, *CIRP Annals - Manufacturing Technology*, 48(1): 163-166.
- [22] L. Li, D.K.Y. Low, M. Ghoreishi, J.R. Crookall, 2002, Hole taper characterisation and control in laser percussion drilling, *CIRP Annals - Manufacturing Technology*, 51(1): 153-156.
- [23] F. Xuan, L. Cao, Z. Wang, S. Tu, 2010, Mass transport in laser surface nitriding involving the effect of high temperature gradient: Simulation and experiment, *Computational Materials Science*, 49(1): 104-111.
- [24] M.C. Kong, C.B. Miron, D.A. Axinte, S. Davies, J. Kell, 2012, On the relationship between the dynamics of the power density and workpiece surface texture in pulsed laser ablation, *CIRP Annals - Manufacturing Technology*, 61(1): 203-206.
- [25] R. Pfeifer, D. Herzog, M. Hustedt, S. Barcikowski, 2010, Pulsed nd: YAG laser cutting of NiTi shape memory alloys—Influence of process parameters, *Journal of Materials Processing Technology*, 210(14): 1918-1925.
- [26] N. Muhammad, D. Whitehead, A. Boor, W. Oppenlander, Z. Liu, L. Li, 2012, Picosecond laser micromachining of nitinol and platinum–iridium alloy for coronary stent applications, *Applied Physics A: Materials Science & Processing*, : 1-11.
- [27] H. Tönshoff, C. Emmelmann, 1989, Laser cutting of advanced ceramics, *CIRP Annals-Manufacturing Technology*, 38(1): 219-222.
- [28] R. Singh, M.J. Alberts, S.N. Melkote, 2008, Characterization and prediction of the heat-affected zone in a laser-assisted mechanical micromachining process, *International Journal of Machine Tools and Manufacture*, 48(9): 994-1004.
- [29] Dassault Systèmes, 2013, UMAT for superelasticity and plasticity of shape memory alloys, Abaqus, .
- [30] J. Lubliner, F. Auricchio, 1996, Generalized plasticity and shape memory alloys, *International Journal of Solids and Structures*, 33(7): 991-1003.
- [31] F. Auricchio, R.L. Taylor, 1997, Shape-memory alloys: Modelling and numerical simulations of the finite-strain superelastic behavior, *Computer Methods in Applied Mechanics and Engineering*, 143(1–2): 175-194.
- [32] C. Fu, Y. Guo, J. McKinney, X. Wei, 2012, Process mechanics of low plasticity burnishing of nitinol alloy, *Journal of Materials Engineering and Performance*, 21: 2607-2617.
- [33] J. Meijer, K. Du, A. Gillner, D. Hoffmann, V. Kovalenko, T. Masuzawa, A. Ostendorf, R. Poprawe, W. Schulz, 2002, Laser machining by short and ultrashort pulses, state of the art and new opportunities in the age of the photons, *CIRP Annals-Manufacturing Technology*, 51(2): 531-550.

CHAPTER 5

PROCESS – SURFACE INTEGRITY MAP IN FIBER LASER CUTTING OF SHAPE MEMORY ALLOY

Abstract

Laser cutting cardiovascular stents induces thermal damage which deteriorates surface integrity. However, the basic relationship between laser cutting and the resulting surface integrity is poorly understood. This study aims to clarify the process mechanism in fiber laser cutting of a shape memory alloy. Kerf profile, roughness, microstructure, nanohardness, and element variation were used to investigate laser cutting process capability. A process-surface integrity map was created to determine the process window for optimal surface integrity. A 3-dimensional finite element model with a moving volumetric heat flux of a pulsed laser was developed to explain the underlying mechanism of microscale material removal.

5.1 Introduction

Nitinol, a nearly equiatomic nickel-titanium shape memory alloy (SMA), has been widely used to fabricate vascular stents (Fig. 5.1a) due to its outstanding mechanical properties, fatigue and corrosion resistance, and biocompatibility [1]. Laser cutting is the predominate method in manufacturing stents via a complex multiphysics mechanism including thermal heating, dynamic melting, and vaporization [2].

Fiber laser cutting is an emerging process for microfabrication due to its exceptional beam quality, reliability, system flexibility, and process efficiency. In addition, the low acquisition cost and maintenance as well as the compact size have made fiber lasers suitable for production (Fig. 5.1b). Most fiber lasers are still considered to be in the “long pulse” range, and thus, still produce thermal damage such as dross, recast, heat affected zone (HAZ), microcracks, and high tensile residual stress [3]. The thermal-induced material damage deteriorates surface integrity and product performance. Finishing processes are often required to remove the thermally damaged layer, which leads to a high cost.

Numerous types of lasers have been used to cut Nitinol. Pfeifer et al. [4] have shown that Nd:YAG laser cutting of Nitinol results in significant thermal damage. Other studies have shown that short- and ultrashort-lasers reduce thermal damage, but as a consequence, lower the material removal rate to a level not suitable for production [5,6]. As an alternative, fiber lasers produce cleaner cuts in comparison to Nd:YAG lasers due to the better beam quality [7]. Therefore, fiber laser cutting Nitinol has great potential to manufacture high quality stents. However, little research has been done to investigate the process mechanisms, surface integrity, and thermal damage characteristics. Moreover, a general guideline for selecting process parameters to optimize surface integrity is highly demanded in production.

To address the pressing issues, the objectives of this study are to: (1) evaluate the effect of key process parameters on surface integrity; (2) understand the nature of thermal damage such as recast and HAZ using EDS, EBSD, and nano-indentation; (3) create a process window for optimal surface integrity; and (4) explain the underlying process mechanisms using a novel 3D finite element model with a moving pulsed volumetric heat flux.

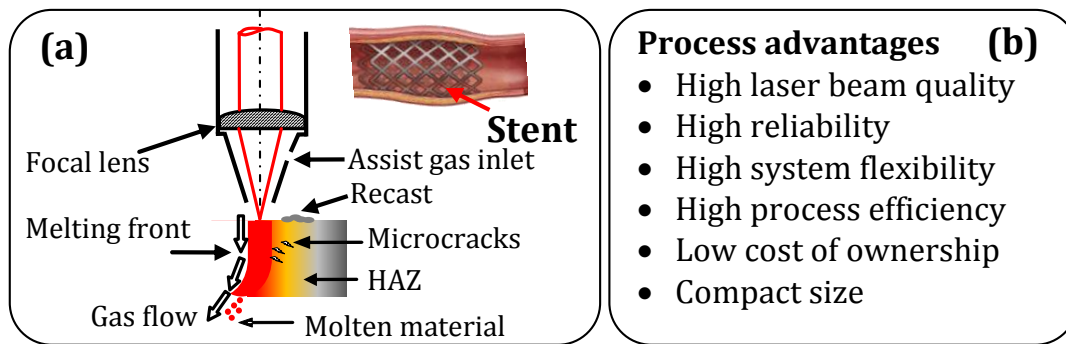


Fig 5.1 Fiber laser cutting Nitinol SMA – process characteristics.

5.2 Laser Cutting Experimental Procedure

The laser cutting experiment was performed using a single mode ytterbium fiber laser system. The fiber laser has an M^2 value of approximately one, which indicates outstanding beam quality. The detailed experimental conditions are listed in Table 5.1. A full factorial analysis was used to determine the effect of peak laser power and cutting speed on cutting quality. The pulse frequency and pulse width were kept constant since laser power and cutting speed directly control the total energy input to the workpiece and consequent thermal damage. Argon was used as the assisting gas to expel the molten material from the kerf and reduce oxidation. The laser focal position was on the workpiece surface. The workpiece (thickness 0.75 mm) exhibited an austenitic microstructure and had superelasticity at room temperature [8].

Table 5.1 Laser Cutting Conditions

Process parameters	Unit	Values
Peak power	W	450, 600, 750, 900, 1050, 1200
Cutting speed	mm/min	200, 300, 400, 500, 600, 700
Pulse frequency	Hz	100
Pulse width	ms	0.75
Pulse shape		Nearly rectangular
Assist gas		Ar
Gas pressure	psi	120
Nozzle stand-off	mm	1
Focal position	mm	0 (on the workpiece surface)
Focal spot diameter	μm	65

5.3 Process - Surface Integrity Map

5.3.1 Kerf Profile

[Fig. 5.2](#) shows the measured entry and exit kerf widths. The entry and exit kerf widths ranged from 75 μm to 160 μm . Kerf widths were larger in general at low cutting speeds compared to high speeds; however, narrow kerfs with a small deviation were obtained at the combination of high speed and low power. At low cutting speeds, kerf width was found to be less dependent on changes to laser power. At high cutting speeds, kerf width increased linearly with increasing laser power.

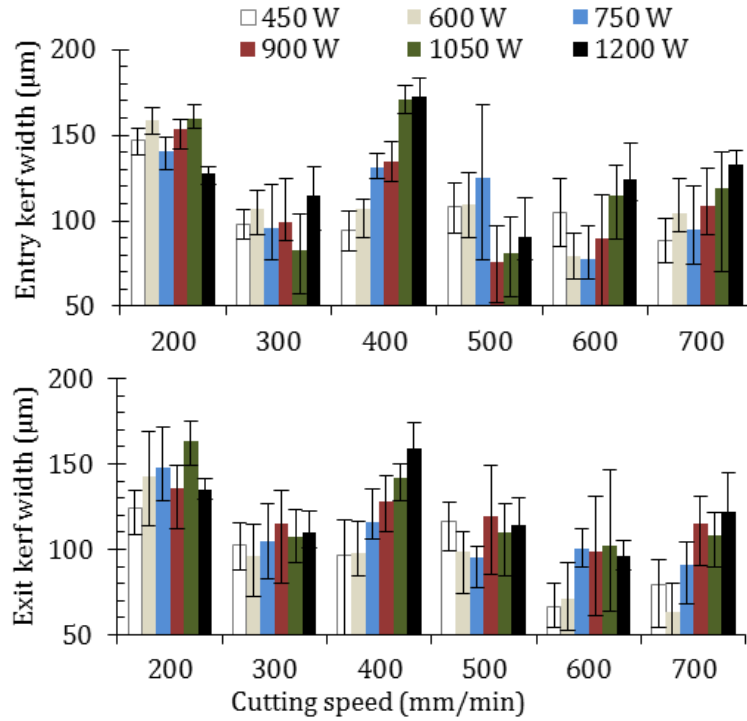


Fig. 5.2 Kerf width as a function of laser power and cutting speed.

5.3.2 Surface Roughness

Surface roughness (Ra) was measured using a profilometer with a sampling length of 2 mm. The measuring direction was parallel to the laser cutting direction. Fig. 5.3a shows the surface roughness as a function of laser power and cutting speed. Roughness was generally lower at low cutting speeds (200 mm/min to 300 mm/min) as compared to high cutting speeds (600 mm/min to 700 mm/min). The smallest roughness of 4 μm occurred at an intermediate cutting speed and highest laser power. Increasing cutting speed significantly increased surface roughness due to reduced pulse overlapping. At the same cutting speed, laser power only marginally influenced surface roughness except at medium speeds. Figs. 5.3b and 5.3c show the representative surface topography at low and high roughness conditions, respectively. At low speed and high power, the striation formation is mainly due to the molten material flow, which is

characterized by the wavy pattern. At high speed and low power, the striation formation is mainly due to the low pulse overlapping, which is indicated by the columnar micro grooves.

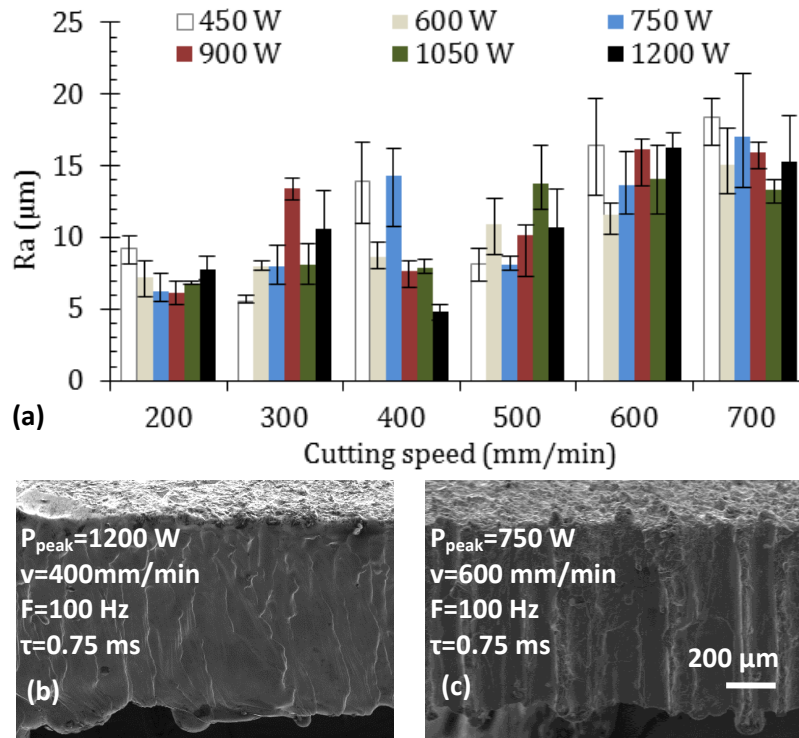


Fig. 5.3 (a) Roughness as a function of laser power and cutting speed; (b-c) surface topography w. low and high roughness.

Fig. 5.4 shows the effect size (η^2), i.e. degree of association, between cutting speed and laser power on the kerf geometrical characteristics. It is calculated as the ratio of a single process parameter's variance over the total variance. It can be seen that kerf width, taper angle, and surface roughness were predominately influenced by cutting speed. The effect of laser power on roughness was negligible.

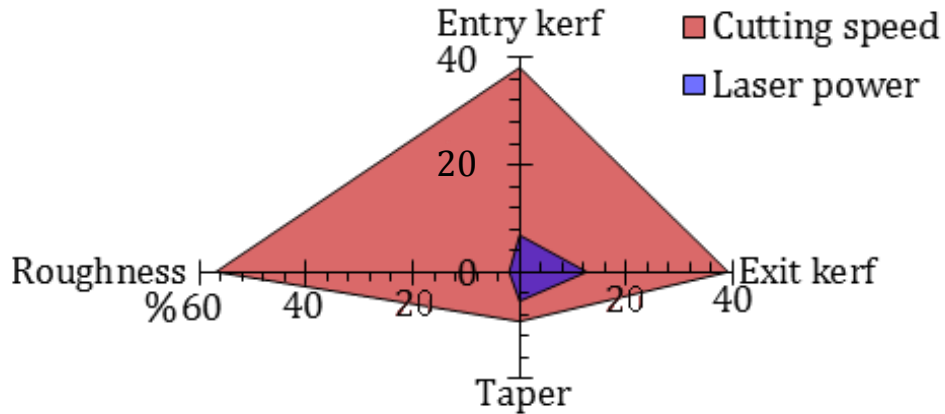


Fig. 5.4 Measure of the effect size (η^2), i.e. measure of the degree of association between process parameters and kerf characteristics.

5.3.3 Subsurface Microstructure Characterization

To reveal the subsurface microstructure, the samples were final polished using a 0.25 μm diamond spray and then etched. A representative microstructure after laser cutting is shown in Fig. 5.5. A clean cut with a uniform kerf and minor recast and dross is presented in Fig. 5.5a. In contrast, a rough cut characterized by severe recast and dross is shown in Fig. 5.5b. Recast was observed in two regions, i.e. on the sample surface at laser entry side (entry recast) and along the kerf (side recast). The entry recast was mainly due to the vaporization-recondensation of the molten material and thus, features a “coral reef” topography as shown in Fig. 5.5c. In contrast, the side recast was mainly due to a melting-resolidification process. Side recast covers the machined surface and directly influences surface roughness, microhardness, corrosion, and fatigue.

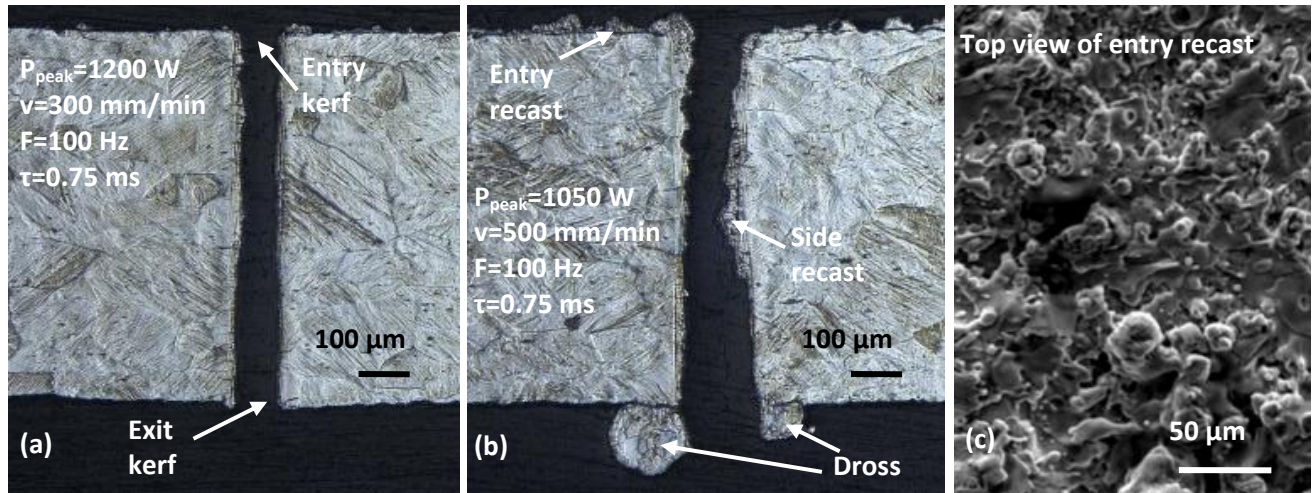


Fig. 5.5 Representative kerf geometry: (a) clean cut w.o. dross, (b) rough cut w. recast and dross, and (c) top view of the entry recast.

To further investigate the characteristics of the side recast, an electron backscatter diffraction (EBSD) analysis was performed on the cross-section of the laser cut workpiece. [Figs. 5.6a](#) and [5.6b](#) show the inverse pole figure (IPF) maps at high and low energy cases, respectively. With the high energy input, recast was clearly visible by a layer of much smaller grains ($< 1 \mu\text{m}$) than the bulk microstructure (grain size $\approx 70 \mu\text{m}$). The formation of these submicron grains was due to fast quenching caused by the assisting gas. No recast layer was detected at low energy level. [Figs. 5.6c](#) and [5.6d](#) show the Kernel average misorientation (KAM) at high and low energy cases, respectively. KAM is a reliable indicator of residual strain in crystalline materials. At high energy input, no significant misorientation was observed. This is associated with the fact that thermal energy is absorbed by the formation of new grains and thus, strain accumulation is relieved. At low energy input, a strained layer near the machined surface was observed as a result of the thermally induced tensile residual stress.

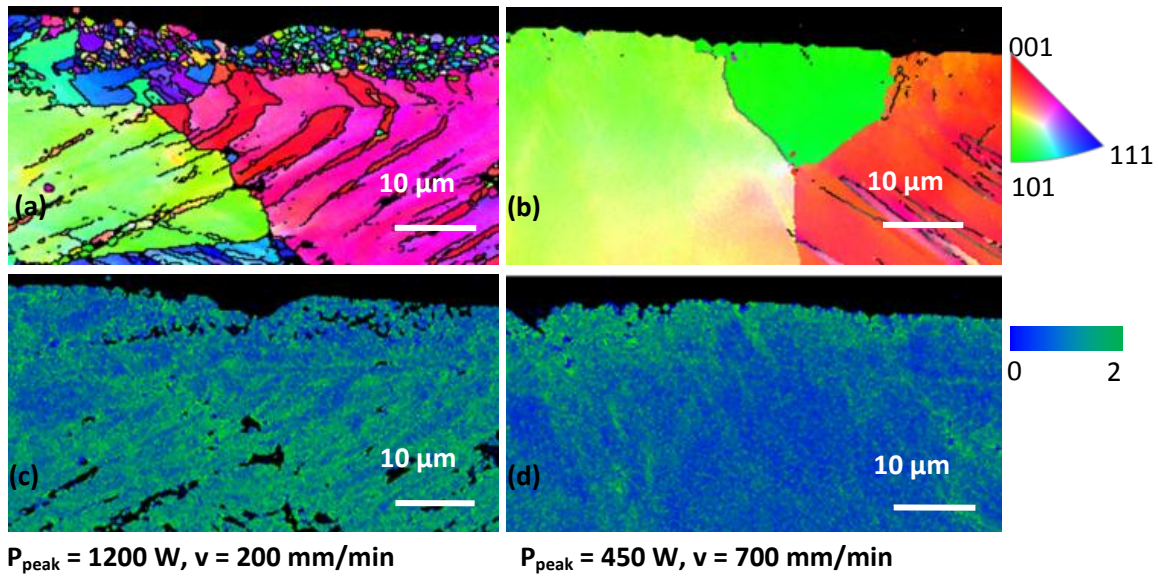


Fig. 5.6 (a, b) EBSD grain boundary; (c, d) grain misorientation.

5.3.4 Element Analysis

Energy dispersive spectroscopy (EDS) analysis (Fig. 5.7) near the machined surface shows that it only consists of Ti and Ni elements at both high energy and low energy conditions. There was less than 1% difference between the measured and nominal element weight. The absence of oxygen indicates that oxidization in the melting-solidification process can be effectively eliminated by using inert assisting gas.

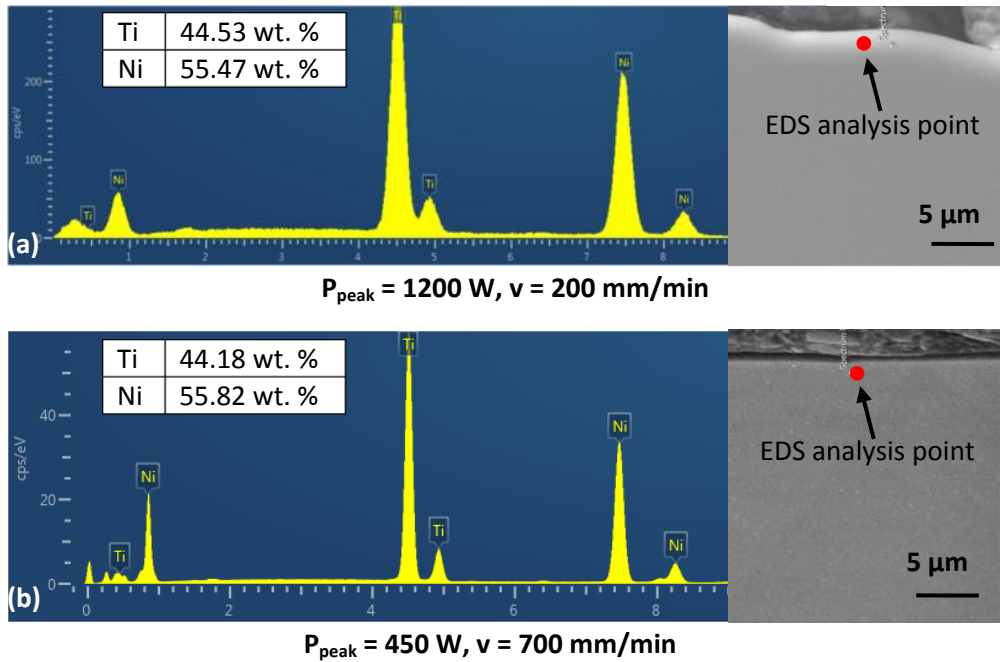


Fig. 5.7 EDS of the machined surface: (a) high power w. low speed; (b) low power w. high speed.

5.3.5 Nanohardness Profile and HAZ

To further investigate the mechanical properties and thickness of the recast layer and HAZ, nano-indentation was performed on the subsurface of the cut samples. A representative nano-hardness profile is shown in Fig. 5.8. The recast layer was found to have lower hardness than the bulk material. This finding contradicted other studies such as EDMed Nitinol [9] or femtosecond laser cut Nitinol [5]. The possible reason is that there were no detected carbides, nitrides, or element alloying as confirmed by the EDS analysis. Compared to the hardness of the base material, within a range of 50 μm in the subsurface, an overall hardness decrease of 20% was detected in the HAZ. The HAZ thickness (50 μm) in this study was found to be independent of the process parameters and was smaller than that (100 μm) produced by an Nd:YAG laser

under similar cutting conditions [4]. This indicates the advantage of using a high quality beam that is inherent to fiber laser when cutting Nitinol devices.

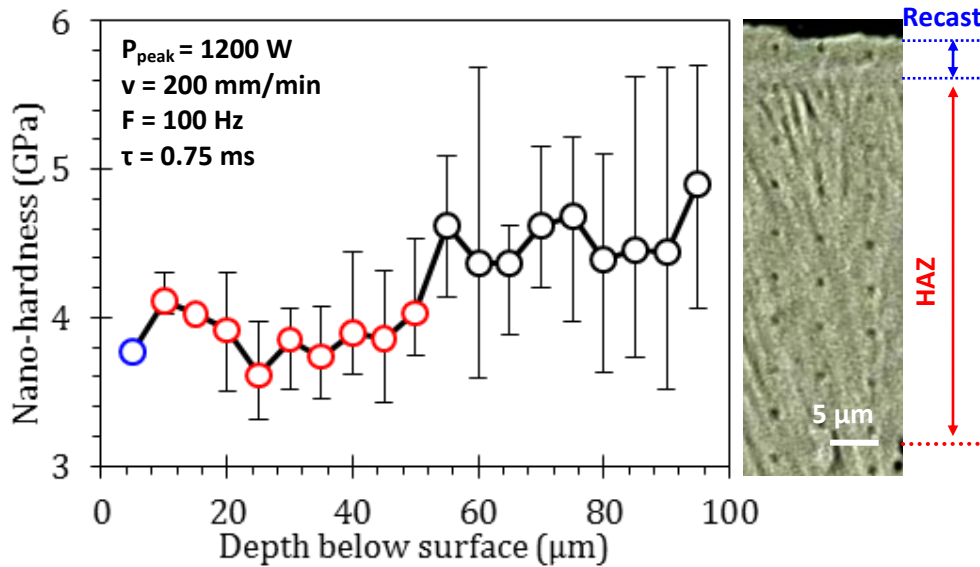


Fig. 5.8 Representative nanohardness profile in the subsurface.

5.3.6 Process – Surface Integrity Map for Optimal Surface Integrity

Key surface integrity characteristics such as roughness, recast, dross, and kerf geometry were selected as indicators for determining the process window as shown in Fig. 5.9. Three zones were identified as the primary, secondary, and tertiary process windows. The experimental cases that have low cutting speeds and high powers generated uniform kerf, low roughness, and small entry recast. However, the trade-off is the dross formation. At high cutting speeds and high powers, the dross formation can be minimized. Nevertheless, roughness and kerf uniformity is compromised with the formation of severe entry recast.

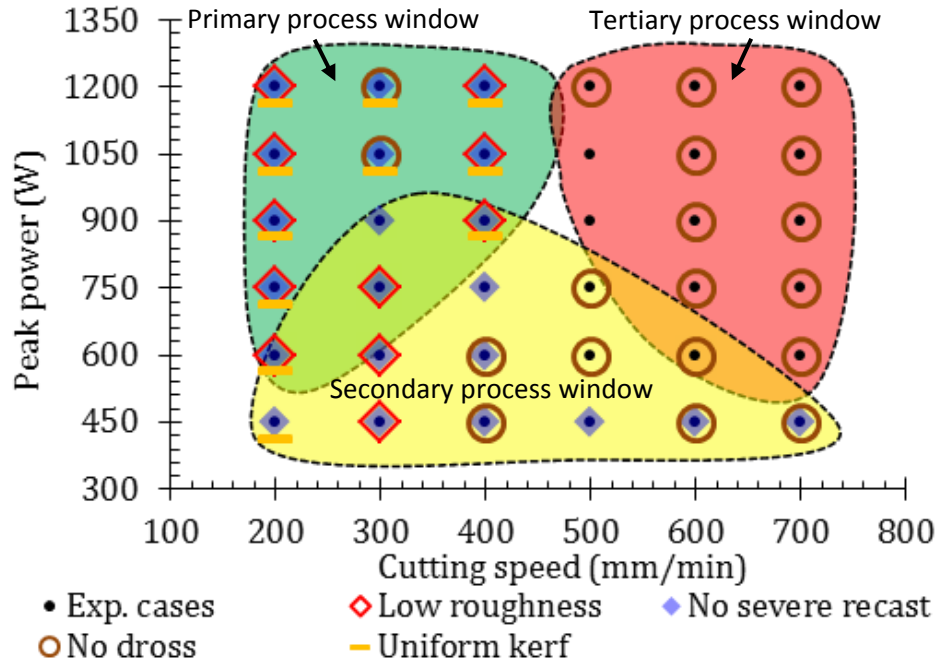


Fig. 5.9 Process – surface integrity map for optimal surface integrity.

5.4 Process Mechanisms

To investigate process mechanisms in laser cutting Nitinol, a 3D finite element model (Fig. 5.10a) was developed. Two extreme conditions with the maximum and minimal cutting energy cases in Table 1 were considered. Fig. 5.10b illustrates the modeling procedure for a moving volumetric heat flux of a pulsed laser. The modulated laser power was defined as a function of laser frequency (f), ratio (m) of period ($1/f$) to pulse width (τ), and time (t). The laser power (P) was equal to peak power (P_{peak}) during the pulse width. When there was no pulse within one period, P was set to zero. N was an integer that represented the N^{th} period. The moving heat flux was determined by the absorption coefficient (A), the time dependent laser power (P), laser spot radius (R_0) on the workpiece surface, and the sample thickness (h). A 3D Gaussian distributed heat flux was applied throughout the sample thickness. The instantaneous

laser spot radius (r) was a function of depth (z) and decreased in the thickness direction due to decaying laser intensity. A decay coefficient (D) was defined to accommodate the conical shape of the volumetric heat flux. The heat flux was implemented via a thermal loading subroutine DFLUX. The DFLUX subroutine calculates the heat flux according to the equations defined in Fig. 5.10b. The novelty of the modeling procedure has two aspects: first, it more realistically represents moving laser pulses with a volumetric heat flux that has a high spatial and temporal accuracy; second, it is a versatile approach since only laser cutting process parameters are required.

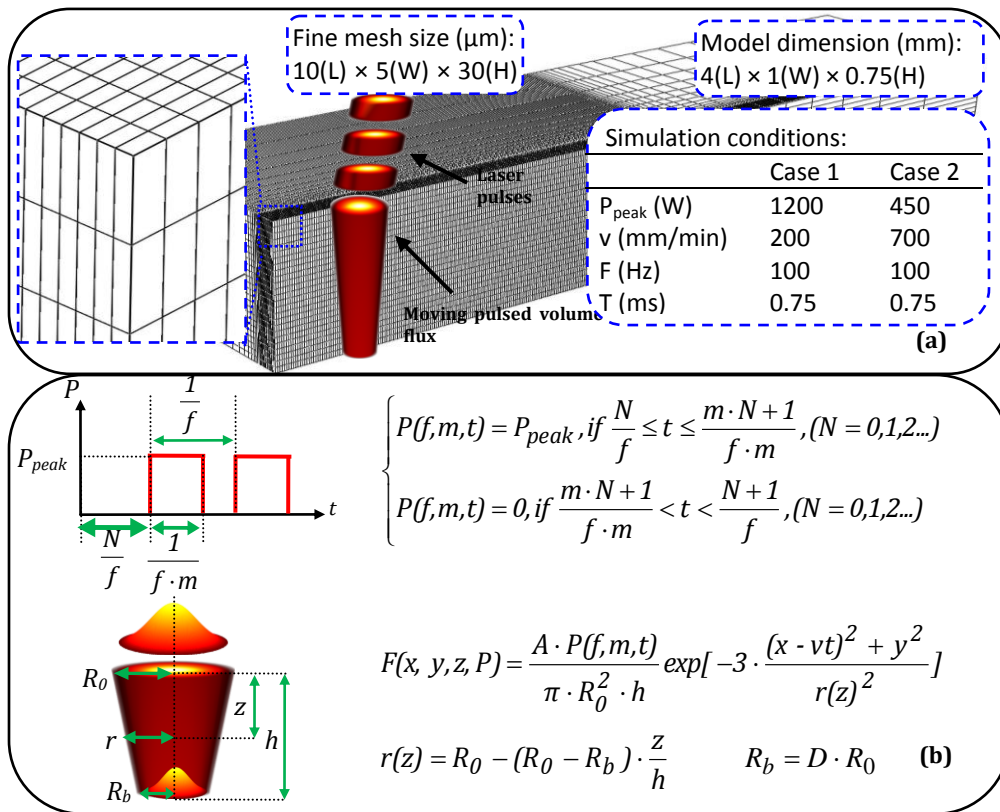


Fig. 5.10 (a) 3D simulation setup; (b) modeling of moving pulsed volumetric heat flux.

The key criterion to model material removal was based on whether nodal temperature has exceeded the melting temperature. The microscale material removal was realized via a USDFLD subroutine. Fig. 5.11 shows the representative predicted kerf geometries with temperature contours. The predicted surface topography resembled the measured ones in both cutting cases. More specifically, both the predicted and measured surface topography had a wavy surface texture at a low cutting energy and columnar micro grooves at a high cutting energy. The similar surface characteristics demonstrated the prediction capability of the developed process model. Although transient temperature is very challenging to measure in laser cutting, the temperature contour can be predicted to correlate temperature distribution and HAZ formation as the predicted temperature profile is directly related to HAZ thickness.

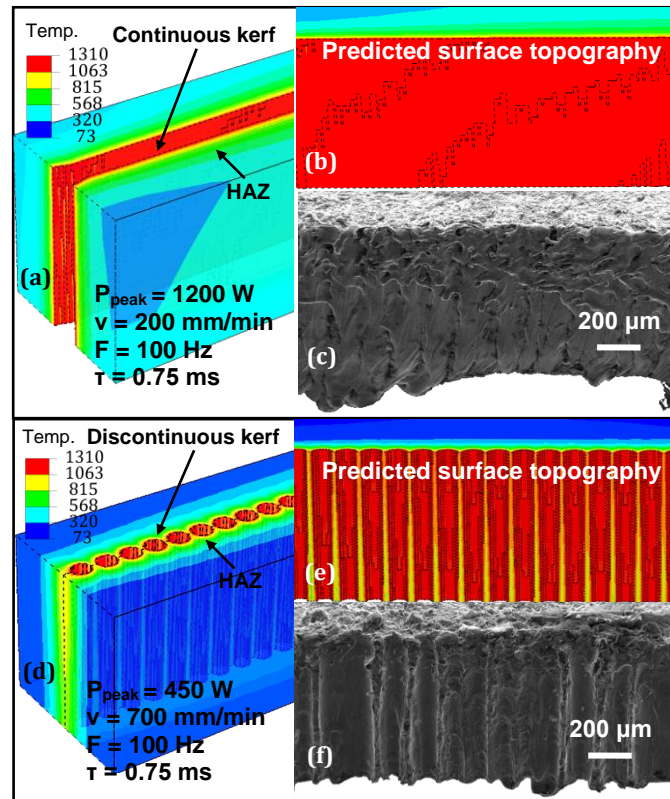


Fig. 5.11 The predicted and measured surface topography: (a-c) high power w. low speed, (d-f) low power w. high speed.

5.5 Conclusions

Surface integrity and process mechanisms in fiber laser cutting were investigated. Key findings are summarized as follows:

- The combination of high speed and low power produces a narrow and uniform kerf, while low speed with various power levels produces a small surface roughness. Cutting speed has a higher statistical significance than laser power in terms of kerf geometry and surface roughness.

- Melting-resolidification and vaporization-recondensation are mechanisms for side recast and entry recast, respectively. Side recast microstructure is characterized by sub-micron grains.
- The high beam quality of a fiber laser is the major contributing factor to smaller HAZ compared to an Nd:YAG laser.
- A process-surface integrity map is created for fiber laser cutting Nitinol.
- The 3D finite element process model with a moving pulsed volumetric heat flux can predict microscale material removal, kerf geometry, and surface topography characteristics.

5.6 References

- [1] T. Duerig, A. Pelton, D. Stöckel, 1999, An overview of nitinol medical applications, *Materials Science and Engineering: A*, 273:149-160.
- [2] F.O. Olsen, L. Alting, 1989, Cutting front formation in laser cutting, *CIRP Annals-Manufacturing Technology*, 38(1):215-218.
- [3] J. Meijer, K. Du, A. Gillner, D. Hoffmann, V. Kovalenko, T. Masuzawa, A. Ostendorf, R. Poprawe, W. Schulz, 2002, Laser machining by short and ultrashort pulses, state of the art and new opportunities in the age of the photons, *CIRP Annals-Manufacturing Technology*, 51(2):531-550.
- [4] R. Pfeifer, D. Herzog, M. Hustedt, S. Barcikowski, 2010, Pulsed nd: YAG laser cutting of NiTi shape memory alloys—Influence of process parameters, *Journal of Materials Processing Technology*, 210(14):1918-1925.
- [5] H. Huang, H. Zheng, G. Lim, 2004, Femtosecond laser machining characteristics of nitinol, *Applied Surface Science*, 228(1):201-206.
- [6] N. Muhammad, D. Whitehead, A. Boor, W. Oppenlander, Z. Liu, L. Li, 2012, Picosecond laser micromachining of nitinol and platinum–iridium alloy for coronary stent applications, *Applied Physics A: Materials Science & Processing*, :1-11.
- [7] H. Meng, J. Liao, Y. Zhou, Q. Zhang, 2009, Laser micro-processing of cardiovascular stent with fiber laser cutting system, *Optics & Laser Technology*, 41(3):300-302.

- [8] Y. Guo, A. Klink, C. Fu, J. Snyder, 2013, Machinability and surface integrity of nitinol shape memory alloy, *CIRP Annals - Manufacturing Technology*, 62(1):83-86.
- [9] J.F. Liu, L. Li, Y.B. Guo, 2014, Surface integrity evolution from main cut mode to finish trim cut mode in W-EDM of shape memory alloy, *Applied Surface Science*, 308(0):253-260.

CHAPTER 6

THE EFFECT OF SURFACE INTEGRITY ON TENSILE AND FATIGUE STRENGTH OF NITINOL BY FIBER LASER CUTTING

Abstract

Nitinol alloys are widely used in fabricating vascular stents due to their unique properties of shape memory, superelasticity, and biocompatibility. Laser cutting is the dominant manufacturing process to make Nitinol stents. However, laser cutting is a thermal process which will induce thermal damage such as recast layer and heat affected zone, which would negatively influence the tensile and fatigue strength of a Nitinol stent. In this study, three levels of surface integrity have been produced by varying the laser cutting parameters. Tensile and fatigue tests were performed to correlate the tensile and fatigue strength at different surface integrity levels. Moreover, a finite element analysis has been conducted to obtain insights into the integral effects of surface integrity and phase transformation on tensile and fatigue strength of the laser cutting Nitinol samples.

6.1 Introduction

6.1.1 Nitinol Material

Nitinol is a binary alloy consisting of a near equal mixture of nickel and titanium. It has broad applications in aerospace and biomedical industries due to its shape memory and superelastic properties. Shape memory describes the effect of restoring the original shape of a plastically deformed sample by heating it upon a transition temperature. Superelasticity corresponds to a process such that, within a certain temperature range, Nitinol has much greater elastic recoil (up to 8%) than other commonly used materials. Nitinol obtains its shape memory and superelastic characteristics from a temperature-controlled, diffusionless, reversible phase change from an austenitic to a martensitic microstructure. A detailed stress-strain-temperature based phase transformation diagram to illustrate the superelasticity and shape memory process of Nitinol can be found in [1].

6.1.2 Stent Application and Laser Cutting Process

Nitinol has gained extensive attention in the biomedical industries due to three reasons. Firstly, Nitinol is very biocompatible due to a formation of inert homogeneous oxidation layer [2]. Secondly, Nitinol shares a very similar mechanical response to biological material such as hair, tendon and bone [3]. Lastly, Nitinol's superelasticity within the certain temperature range shows great potential in deploying devices in human body. Many devices are designed based on this concept, such as endovascular stents. Stent is a medical device that is used to restore the patency of a stenosed or narrowed luman [4]. Currently, the majority of stents are manufactured by laser cutting process due to the small size and complex geometry of a stent [5]. A finely focused laser beam can produce a micrometer size kerf on Nitinol. Also, the non-contact thermal

process can eliminate pressing issues such as burr formation and tool wear inherited from mechanical cutting [1].

6.1.3 Research Objective

This study focuses on the tensile and fatigue strength of Nitinol after laser cutting. The rationales for this research are as follows: (1) for medical devices such as stent, it is required to demonstrate exceedingly good fatigue performance. More specifically, the fatigue testing of the stent should include in vitro testing until ten-year equivalent (400 million) cycles in an appropriate test solution to simulate physiological condition; (2) laser cutting is a thermal process, which will lead to thermal damages such as striation, heat affected zone, recast layer, and tensile residual stress. The thermal damage worsens the surface integrity of the parts and detrimentally affects the performance; and (3) in vivo loading conditions for Nitinol medical devices are very complex. More specifically, Nitinol not only are subjected to cyclic loading, but also “single-event” overloads. To mimic these loading conditions, both tensile testing and fatigue testing needs to be conducted. However, based on a literature survey, little research has been done to investigate the integral relationship between surface integrity by laser cutting, tensile strength, and fatigue performance. Therefore, the specific objectives of this study are to (1) generate three levels of surface integrity by changing laser cutting parameters, (2) establish the relationship between surface integrity, tensile, and fatigue performance of laser cut Nitinol, and (3) correlate the mechanical response, phase transformation, and fracture by a finite element analysis.

6.2 Literature Review

6.2.1 Effect of Surface Integrity on Tensile Performance by Laser Cutting

Laser cutting is a thermal process, which will induce thermal damages that could degrade the surface integrity and potentially reduce the tensile strength. Extensive studies have been conducted to explore the effect of surface integrity on the tensile performance after thermal processing such as welding and laser cutting. Watanabe et al. [6] established the relationship between laser processing parameters, surface integrity, and mechanical property of laser treated cast titanium. It was found that the laser treatment improved the surface integrity of cast titanium and consequently increased the tensile strength. A similar finding was published by Poulonquintin et al. [7], where the correlation between laser processing, microstructure, and mechanical properties was investigated. Zoeram et al. [8] performed dissimilar welding of Ti-6Al-4V and Nitinol. It was found that the tensile strength decreased due to the formation of brittle phases. The fractured occurred through the weld metal interface. He et al. [9] studied the effect of hydrogen embrittlement of the fracture toughness of Nitinol. It was found that the toughness dramatically decreased with the increase of hydrogen content. Khan et al. [10] studied the effects of welding parameters on the mechanical response of commercially available SE508 superelastic Nitinol sheet. The results showed that varying the welding parameters dramatically affects the mechanical properties of the material. More specifically, higher peak power and lower pulse frequency provided the best mechanical response from the welded specimens. Dawood et al. [11] investigated the effect of surface roughness on the mechanical properties of 6061 aluminium alloy by friction stir welding. It was stated that the surface roughness had a perceptible influence on the tensile properties. More specifically, the highest ultimate tensile strength was achieved with the smallest roughness.

Unlike traditional materials, phase transformation of Nitinol can be stress induced. Due to the unsymmetrical crystal structure of the stress induced martensites, the hardness of Nitinol martensite is lower than the austenite [12]. The local phase change and hardness variations could influence the tensile performance of laser cut Nitinol. McNaney et al. [13] found martensitic transformation under biaxial loading of Nitinol due to local stress concentration. Khan et al. [14] investigated the local phase change during tensile testing after laser cutting Nitinol. It was found that martensite was added in the laser processed zone. Consequently, the tensile property of Nitinol was detrimentally affected.

6.2.2 Effect of Surface Integrity on Fatigue Performance by Laser Cutting

Fatigue of Nitinol medical device has been an ongoing research topic for the past three decades due to stringent requirement on the fatigue performance. The total life fatigue testing of Nitinol alloys starts with “stress-life” test using standard uniaxial tension-compression on dogbone specimen [15]. Varying conditions such as material composition, testing temperature, microstructure would lead to significant change in the fatigue limits. The testing methods then gradually evolve to “strain-life” due to the uniqueness of the stress-strain behavior of the material. It is a well-known rule of thumb that strain based fatigue test is preferred over stress based fatigue test on Nitinol. It is because the monotonic stress-strain curve shows that global strain is continuous whereas stress tends to ‘plateau’ due to the detwinning mechanism in martensite or due to stress induced martensitic transformation in superelastic material. Therefore, the stress is constant over a wide range of strains. This makes stress based test conditions less certain than strain based. Furthermore, displacement controlled testing requires less sophisticated equipment than load controlled testing. Rotating bending test on Nitinol wires was widely used

as the fatigue testing method [16-18]. It is a convenient way to collect strain based fatigue data since the strain amplitude can be calculated by the ratio of the wire diameter to the curvature diameter and hence a range of strain amplitudes can be achieved for a given wire diameter with slight adjustments in the curvature. Later on, the subcomponents of stent were tested. The processing sequence of the specimens was exactly as the medical device. These specimens therefore can reflect the actual material condition of the devices [19,20]. A very comprehensive review that focused on giving a more universal understanding of the inherent fatigue and fracture resistance of Nitinol for biomedical applications can be found in [21].

Other than the testing method and sample geometry, the complex phase transformation is another factor that needs to be considered when evaluating the fatigue performance of Nitinol. Crystallographic orientations i.e. superelastic austenite, stable austenite, thermal martensite and mixed phase are critical when considering the fatigue crack growth behavior. Robertson et al. [21] concluded that Nitinol with martensite microstructure have the best crack growth resistance, while superelastic austenite Nitinol have the worst.

For conventional metallic materials, it has been found that surface conditions significantly affect the fatigue performance [22,23]. Laser induced thermal damages such as recast layer, micro-cracks, and tensile residual stresses are very likely to detrimentally affect Nitinol fatigue performance. However, based on the literature survey, the effect of surface integrity on the fatigue performance of Nitinol devices has not been well studied, and the relationship between process parameters, surface integrity, and fatigue is not yet established.

6.3 Experimental Procedure

6.3.1 Laser Cutting Experimental Setup

The laser cutting experiments were performed with an IPG[®] fiber laser (Model #: YLR-150/1500-QCW-MM). It is an ytterbium fiber laser with a maximum average power of 150 W when operated at pulsed mode. Due to the outstanding beam delivery capability, the fiber laser can achieve a very good beam quality with an M^2 value close to one.

The work material is superelastic Nitinol (SE508) with a nominal nickel composition of 50.8 at.%. The detailed elemental composition of this Nitinol alloy is listed in [Table 6.1](#). This particular Nitinol alloy is commonly used in biomedical applications. Moreover, the material revealed an austenitic microstructure with a grain size of approximately 60 μm at room temperature. The sheet sample had a thickness of 0.75 mm.

[Table 6.1](#) Compositions of Nitinol SE508

Element	at. %
Ni (nominal)	50.8
Ti	Balance
O (max.)	0.0017
C (max.)	0.0009

6.3.2 Experimental Conditions

The laser cutting Nitinol experimental setup is shown in [Fig. 6.1\(a\)](#). The laser delivery fiber was inserted into an IPG[®] cutting head with a collimation length of 100 mm and a focal length of 125 mm. The laser beam passed through coaxial assisting gas jet and was finely focused on the top surface of the sample. The laser spot diameter at focal position was 62.5 μm .

Argon was used as the assisting gas to avoid nitriding phenomenon. The standoff distance was kept at minimum (1 mm) to reduce dross formation.

Figs. 6.1(b) and 6.1(c) shows the Nitinol sample before and after laser cut, respectively. The dimension of the sample is shown in Fig. 6.1(d). The samples had a width of 25 mm and length of 51 mm. The extended top and bottom regions were to increase the grip area to avoid slip during tensile test. The sample had a diamond shape, which can closely mimic a stent subcomponent. This sample design was previous used to study the fatigue performance [20]. It was adapted in this study to investigate the tensile and fatigue strength.

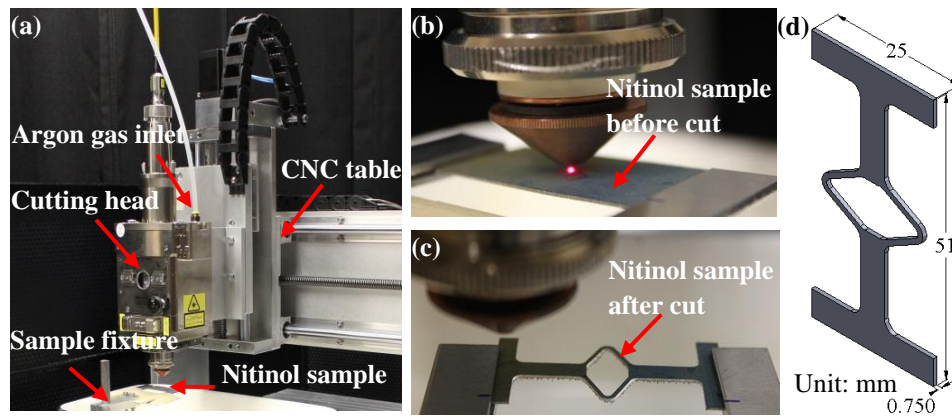


Fig. 6.1 Laser cutting Nitinol experimental setup (a) laser cutting system configuration, (b) Nitinol sheet sample before cut, (c) Nitinol sample after laser cut, and (d) sample dimensions.

The laser cutting conditions is not the focus of this study; instead, the resulting surface integrity in terms of roughness, recast layer thickness, and heat affected zone is the key input parameters, whereas the tensile and fatigue strength is the output. To investigate the relationship between surface integrity and tensile and fatigue strength, three levels of surface integrity was

designed and achieved. The detailed laser cutting parameters to realize the surface integrity levels are listed in [Table 6.2](#). These parameters were chosen based on a previous study [24].

Table 6.2 Laser Cutting Conditions for Three Levels of Surface Integrity

Cut #	Speed (mm/mim)	Peak power (W)	Frequency (Hz)	Pulse width (ms)	Surface integrity
Cut 1	200	1200	100	0.75	Good
Cut 2	400	1200	100	0.75	
Cut 3	200	900	100	0.75	
Cut 4	200	450	100	0.75	Intermediate
Cut 5	400	600	100	0.75	
Cut 6	500	600	100	0.75	
Cut 7	500	1050	100	0.75	Poor
Cut 8	600	1200	100	0.75	
Cut 9	700	1050	100	0.75	

6.3.3 Surface Integrity Characterization

After the laser cutting experiments, key surface integrity features including surface roughness, topography, microstructure, and nanohardness were characterized. The surface roughness was measured using a profilometer. The sampling length was 2 mm on the laser cut surface along the laser cutting direction. Three measurements were acquired and averaged to reduce to measurement error. JOEL 7000 FE-SEM was used to take pictures of the laser cut surface to attain the topography. To study the microstructure, the cross-section of the laser cutting samples were first grinded by sandpaper up to 4000 grit and then polished with diamond spray up to a 0.25 μm finish. All the samples were etched with an aqueous solution that contains 5% HF and 15% HNO₃ [25] to reveal the grain boundaries. HYSITRON TI 900 TriboIndenter was used to measure the nanohardness of all the laser cut samples. All indentations were

performed with a diamond Berkovich indenter that has a nose radius of 100 nm. The loading type was triangle with the maximum load of 1mN. The total time was 20 seconds for each indentation. The indentation matrix was a 3×20 array in the subsurface with an indentation spacing of 5 μm .

6.3.4 Tensile and Fatigue Testing

To evaluate the influence of surface integrity on tensile strength of laser cut Nitinol, uniaxial tensile test was performed with a QTEST tensile testing machine. The load was measured with a load cell. The machine had a constant displacement rate of 3.8 mm/min. The displacement rate was slow enough to ensure quasi-static loading conditions.

The tension-tension fatigue testing was performed using a MTS Landmark® Servohydraulic test system. Displacement control was applied during the fatigue testing. The fatigue test was performed in the tension – tension regime to avoid out-of-plane buckling. The break detection was realized by applying the load drop criterion, i.e., as the fatigue samples fractures, the load drop on the load cell was monitored and used to automatically terminate the test.

6.4 Experimental Results

6.4.1 Surface Integrity

Three key features, i.e., surface roughness (Ra), topography, and microstructure were used to evaluate the surface integrity. More specifically, three levels of microstructure, topography, and roughness values was simultaneously achieved, which divide the surface integrity into three zones as shown in [Fig. 6.2](#). In the first zone, low roughness, uniform

topography, and kerf with little recast were realized. This region was identified as the “good SI”. On the other hand, in the “poor SI” region, very high surface roughness, uneven surface topography, and very large recast layer attaching to the kerf were found. Moreover, microcracks were observed in the thick recast layer as shown in Fig. 6.2. These cracks have the potential to detrimentally affect the tensile and fatigue strength of the laser cut Nitinol.

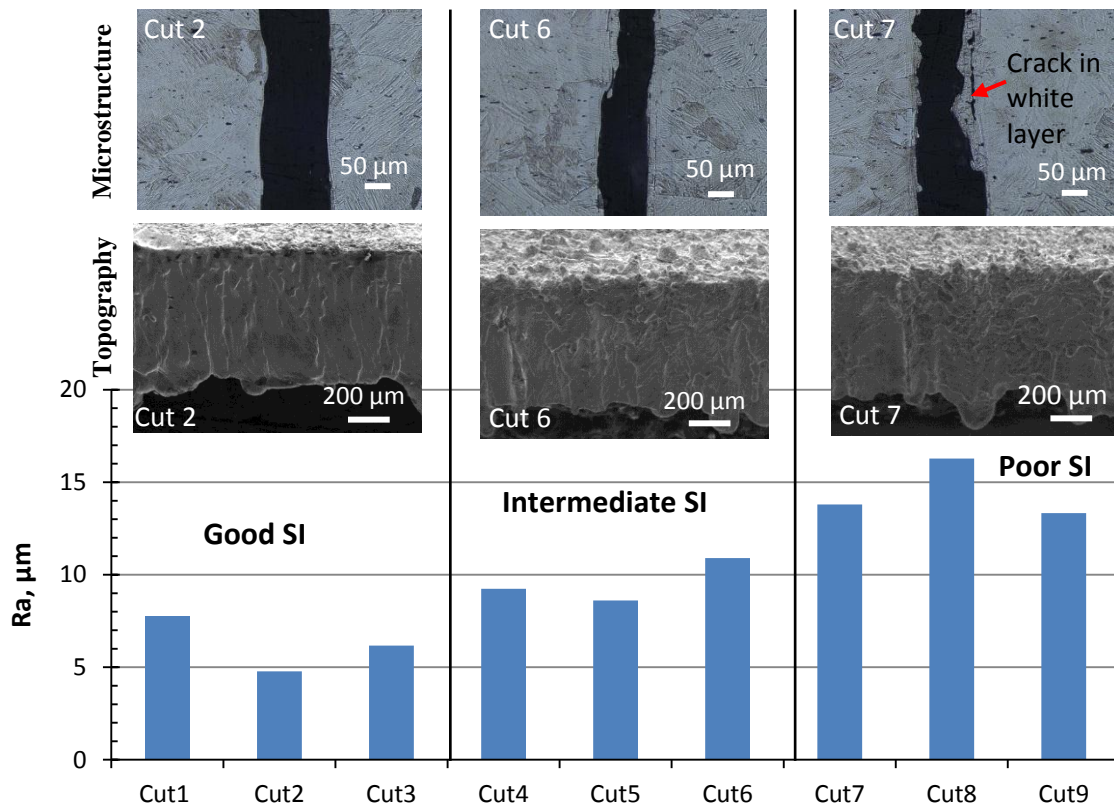


Fig. 6.2 Representative samples with three distinct levels of surface integrity.

A close exam to the microstructure showed that no HAZ coarsening was detected near the laser cut surface. Typically, materials that have undergone laser processing often contain a heat affected zone, where grain coarsening is commonly experienced. This phenomenon is more prominent in materials that originally have a small grain size. An example can be found in the

work by Ogata et al. [26], where significant grain size increasing was observed after laser processing of cold worked Nitinol. However, in the present study, the large grain structure in the bulk material due to the heat treatment weakens the grain coarsening effect in the HAZ. To further confirm this observation, nanoindentation was performed. The nanoindentation profile in the depth direction is shown in Fig. 6.3. There is no hardness reduction found in the HAZ for all the tested cases. This finding proves that no HAZ weakening was induced by the laser cutting process due to the large grain size. However, it was found that the recast layer hardness, which is indicated by the first data point of each condition, generally had lower value than the bulk. The low hardness recast layer covers the laser cut surface, which could reduce the tensile strength of the laser cut Nitinol parts.

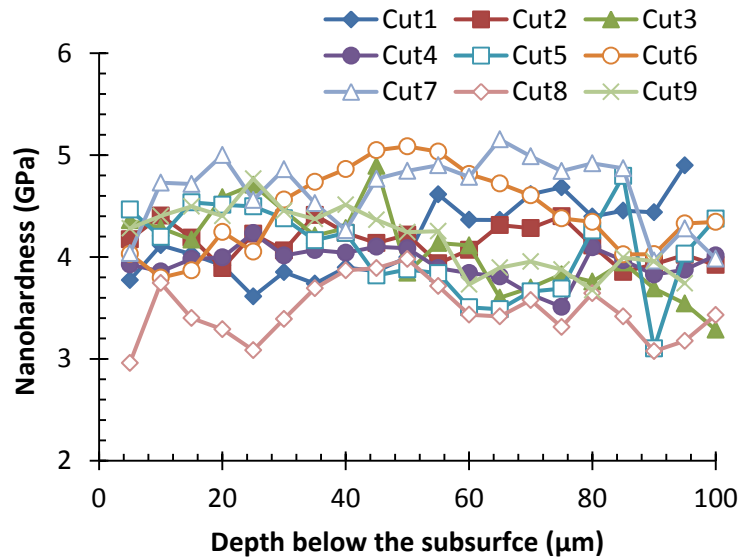


Fig. 6.3 Nanoindentation profiles in the subsurface.

6.4.2 Tensile Testing

Fig. 6.4(a) shows the experimental setup for the tensile test. Figs.6.4(b) and 6.4(c) shows the laser cut Nitinol sample before and after the tensile test, respectively. The fracture occurred in the bended regions (i.e. the knees) of the samples. The tensile test was terminated when both of the knees were fractured. The load – displacement curve for all the tested conditions is shown in Fig. 6.5. All the samples had similar loading curve before fracture. However, the fracture loads, which are the maximum loads before the first load drop, were different for different laser cutting conditions. The fracture loads were averaged at each surface integrity levels and plotted in Fig. 6.6. It was found that the fracture loads decreases as the surface integrity worsens. Moreover, the randomness of the fracture load is smaller at the good surface integrity level than that at poor surface integrity level, as indicated by the error bar range. It can be stated that different surface integrities generated by laser cutting have a significant influence on the tensile properties of laser cut Nitinol. Better surface integrity will lead to a better tensile performance.

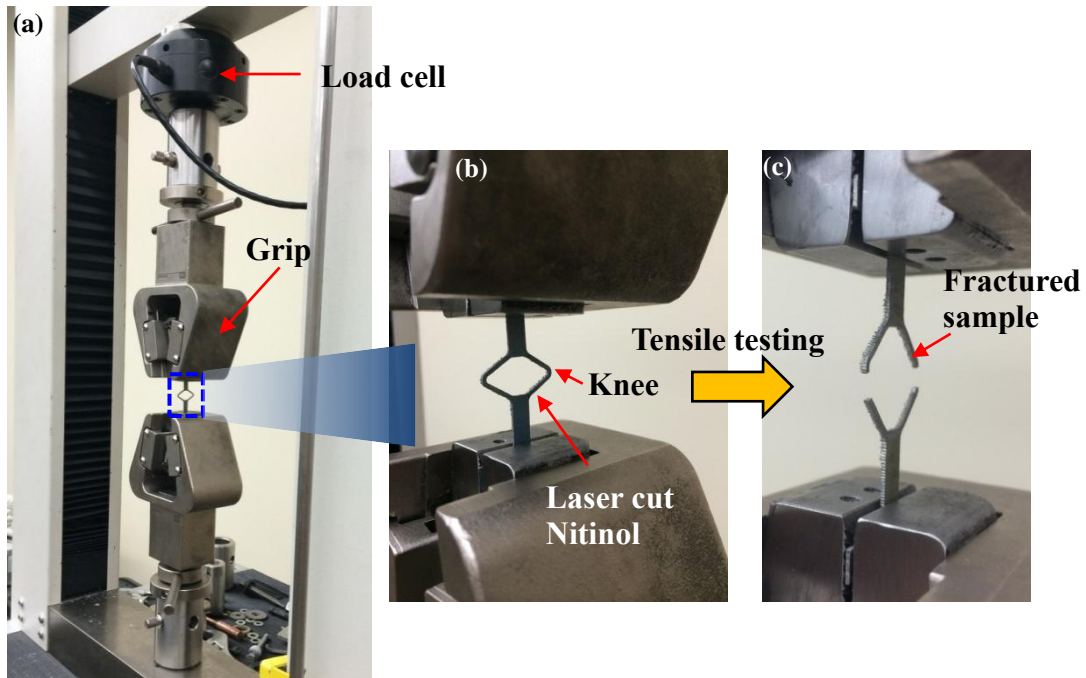


Fig. 6.4 Tensile testing setup.

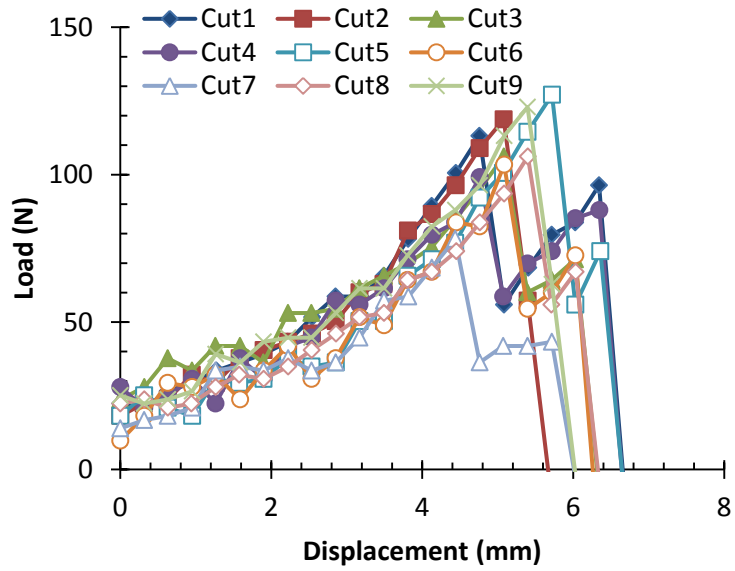


Fig. 6.5 Load displacement curves for different laser cutting conditions.

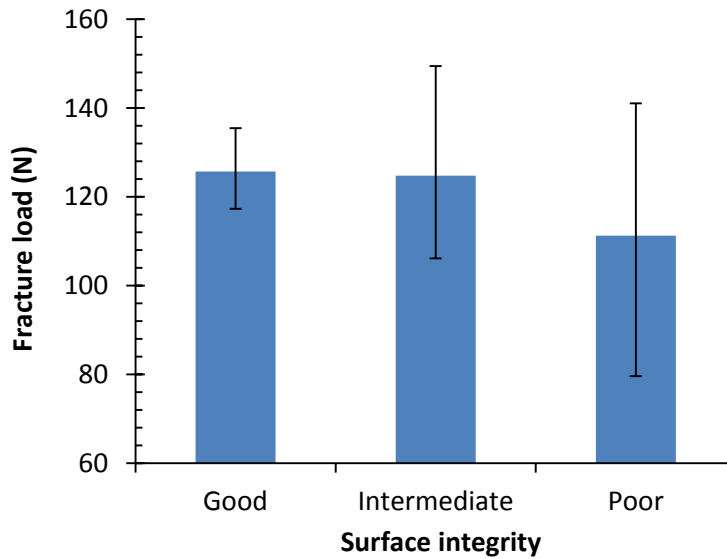


Fig. 6.6 Fracture load at three surface integrity levels.

Figs. 6.7(a) and 6.7(b) shows the fracture loads as a function of surface roughness and maximum recast layer thickness, respectively. The maximum recast layer thickness was acquired at the location where the recast layer is the thickest along the laser cut kerf. The results indicated that as the roughness and the maximum recast layer thickness increases, the fracture loads decreases. As the roughness increases, the striation patterns penetrate deeper into the subsurface, which eventually act as a notch. The presence of the micro-notches worsens the tensile strength of the laser cut part. Similarly, when the recast layer becomes thicker, there could be more microcracks embedded inside the recast and consequently reduce the tensile strength.

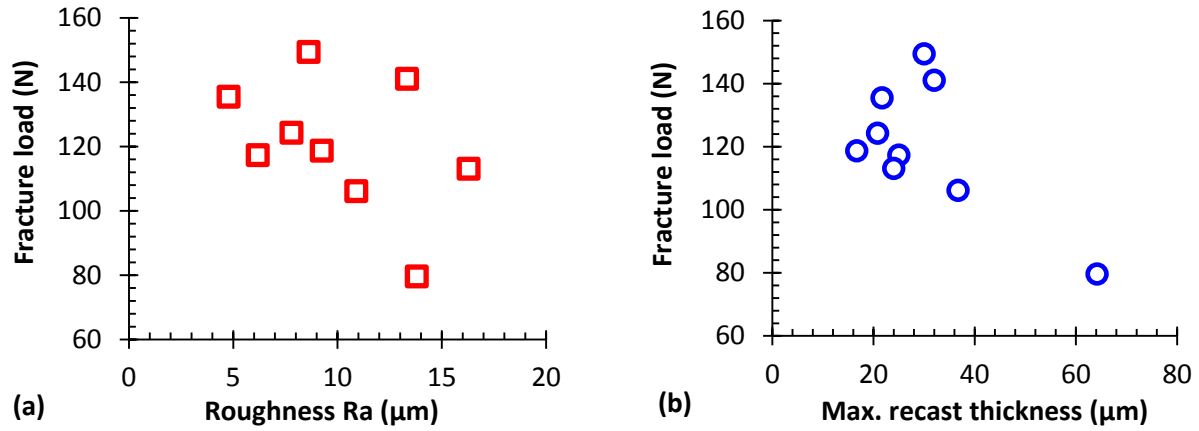


Fig. 6.7 Fracture load as a function of (a) roughness and (b) max. recast thickness.

6.4.3 Fatigue Testing

Fig. 6.8 shows the experimental setup for the fatigue test. Displacements from 0.81mm to 0.99 mm was used in this study, which correspond to a mean strain of 2% and a strain amplitude of 0.3% based on a finite element analysis (FEA). The FEA model is discussed in detail in section 6.5.



Fig. 6.8 Fatigue testing setup.

Similarly to the tensile testing samples, the fracture occurred in the knee region in the fatigue tests. The number of cycles were averaged at each surface integrity levels and plotted in Fig. 6.9. It can be seen that the number of cycles decreases as the surface integrity worsens. This finding confirms the direct correlation between surface integrity and fatigue performance and it can be stated that a better surface integrity will lead to a better fatigue performance.

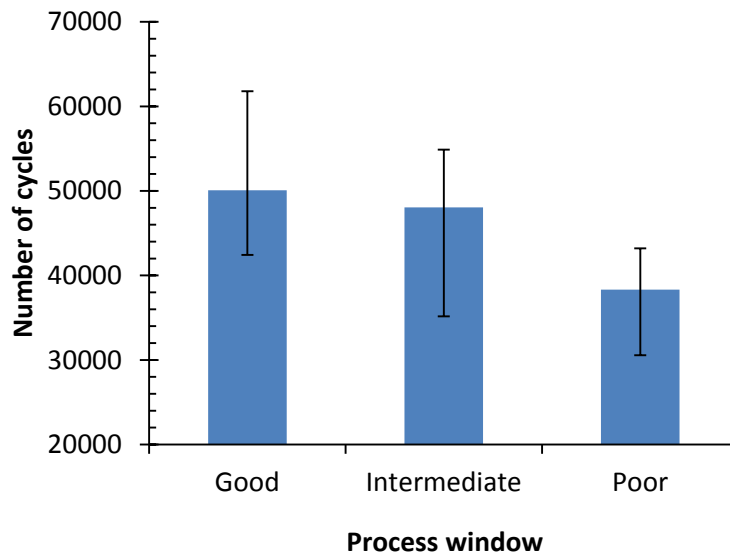


Fig. 6.9 Fatigue life at three levels of surface integrity.

Figs. 6.10(a) and 6.10(b) shows the number of cycles as a function of surface roughness and maximum recast layer thickness, respectively. No obvious trend can be found in these plots, which indicates that the fatigue performance is not solely depend upon a single surface integrity characteristic, such as roughness or recast layer thickness. Instead, the fatigue performance was affected by the surface integrity as an integral factor.

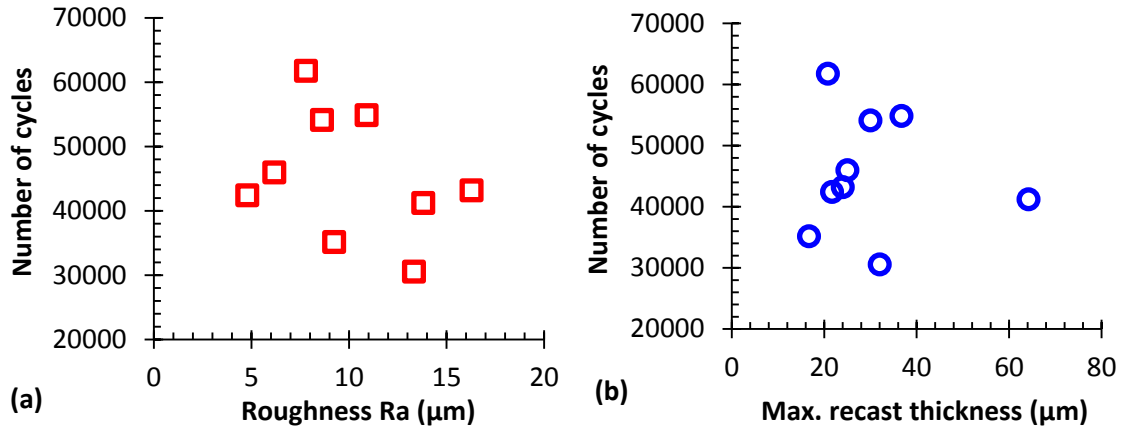


Fig. 6.10 Fatigue life as a function of (a) roughness and (b) max. recast thickness.

6.5 Finite Element Analysis

6.5.1 Mesh

Due to the complex shape of the laser cut sample, the stress and strain at loading was very challenging to calculate. As an alternative, finite element analysis used to predict the stress, strain, and phase transformation of the laser cut samples under tensile loading. ABAQUS finite element package was used. A standard solver was employed to ensure the quasi-static loading conditions. The mesh design is shown in Fig. 6.11. It has the same dimension as the laser cut Nitinol sample in the experiments. Element size was biased with a higher density in the knee region. The boundary condition on the bottom was fixed to provide proper constrain during the loading. Displacement control was applied on the top surface. The total displacement was 6 mm, which was the largest displacement achieved before fracture among all the tested conditions. The total simulation time was 1 second.

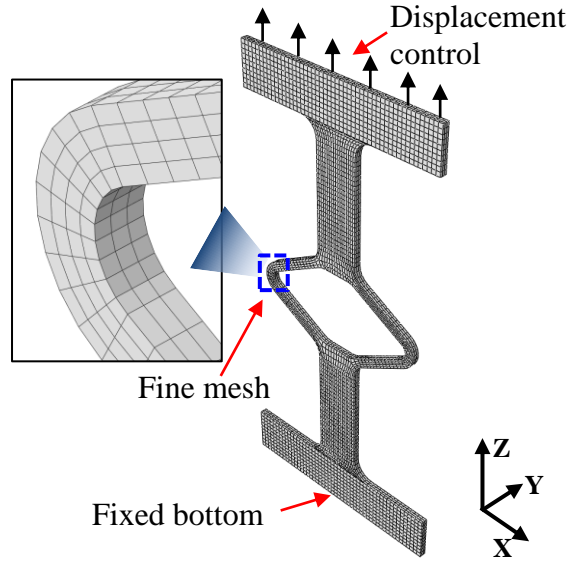


Fig. 6.11 Simulation schematic of tensile and fatigue loading.

6.5.2 Material Modeling of Nitinol

To account for the superelastic property of Nitinol, a material user subroutine UMAT was used. This material model was previously used to simulate Nitinol stent deployment [27], fatigue test of diamond shaped Nitinol sample [20], and burnishing process of superelastic Nitinol [28]. It has been shown that this model can successfully capture the superelasticity and phase transformation of Nitinol. The constitutive equations were based on the work by Auricchio and Taylor [29,30]. The total elastic strain (ε) is the summation of elastic strain (ε^{el}) and the transformation strain (ε^{tr}), which is described by Eq. 6.1.

$$\varepsilon = \varepsilon^{el} + \varepsilon^{tr} \quad 6.1$$

The transformation strain is calculated by

$$\varepsilon^{tr} = \varepsilon^L \xi_S \quad 6.2$$

where ε^L is the maximum residual strain and ξ_s is the fraction of martensite under loading. The stress induced martensitic transformation is described by Eq. 6.3

$$\Delta\xi_s^{AS} = H^{AS}\beta^{AS}(1 - \xi_s)\frac{\dot{F}^{AS}}{(F_f^{AS})^2} \quad 6.3$$

where H^{AS} is the operator for austenite to martensite phase transformation, β^{AS} is the transformation speed, F^{AS} is a Drucker-Prager type loading function to define the temperature and pressure dependent phase transformation. H^{AS} and F^{AS} is calculated by Eq. 6.4 and 6.5, respectively.

$$H^{AS} = \begin{cases} 1, & \text{if } F_s^{AS} > 0, F_f^{AS} < 0, \dot{F}^{AS} > 0 \\ 0, & \text{otherwise} \end{cases} \quad 6.4$$

$$F^{AS}(\tau, T) = ||t|| + 3\alpha p - C^{AS}T \quad 6.5$$

where t is the deviatoric stress, α and C^{AS} are material parameters, p is pressure, and T is temperature. The material constants used in this study were acquired from a curve fitting process between a uniaxial tensile test [13] and the theoretical stress – strain curve [31] as shown in Fig. 6.12. The material constants are listed in Table 6.3.

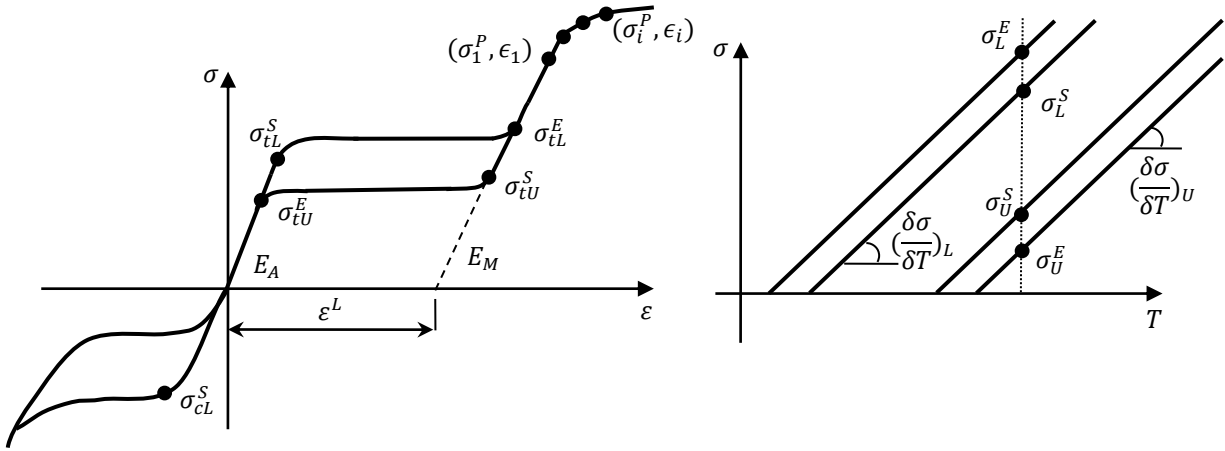


Fig. 6.12 Superelastic-plastic behavior based on the uniaxial behavior.

Table 6.3: UMAT Material Constants of Nitinol in Tension

Material parameter	Material Constant	Material Parameter	Material Constant		
E_a (Pa)	2.140E10	σ_3^p (Pa)	8.470E8	E_a	Austenite elasticity
V_a	0.3	ε_3	0.087	V_a	Austenite Poisson's ratio
E_m (Pa)	1.350E10	σ_4^p (Pa)	9.080E8	E_m	Martensite elasticity
V_m	0.3	ε_4	0.093	V_m	Martensite Poisson's ratio
ε^L	0.02	σ_5^p (Pa)	9.430E8	ε^L	Transformation strain
$(\frac{\delta\sigma}{\delta T})_L$	0	ε_5	0.097	$(\frac{\delta\sigma}{\delta T})_L$	$(\frac{\delta\sigma}{\delta T})$ loading
σ_L^S (Pa)	2.500E8	σ_6^p (Pa)	9.850E8	σ_L^S	Start of transformation loading
σ_L^E (Pa)	5.000E9	ε_6	0.104	σ_L^E	End of transformation loading
T_0 (°C)	22	σ_7^p (Pa)	1.016E9	T_0	Reference temperature
$(\frac{\delta\sigma}{\delta T})_U$	0	ε_7	0.108	$(\frac{\delta\sigma}{\delta T})_U$	$(\frac{\delta\sigma}{\delta T})$ unloading
σ_U^S (Pa)	2.500E8	σ_8^p (Pa)	1.053E9	σ_U^S	Start of transformation unloading
σ_U^E (Pa)	1.000E8	ε_8	0.115	σ_U^E	End of transformation unloading
σ_{cL}^S (Pa)	6.000E8	σ_9^p (Pa)	1.071E9	σ_{cL}^S	Start of transformation stress during loading in compression, as a positive value
ε_V^L	0.02	ε_9	0.119	ε_V^L	Volumetric transformation strain
N_p	11	σ_{10}^p (Pa)	1.088E9	N_p	Number of stress-strain pairs to define yield curve
σ_1^p (Pa)	7.180E8	ε_{10}	0.125		
ε_1	0.076	σ_{11}^p (Pa)	1.097E9		
σ_2^p (Pa)	8.000E8	ε_{11}	0.127	$\sigma_1^p, \varepsilon_1, \dots, \sigma_{11}^p, \varepsilon_{11}$	Stress-strain points in the yield curve
ε_2	0.083				

6.6 Simulation Results

6.6.1 Load – Displacement

To validate the simulations, the predicted load – displacement curve was compared with the measured one as shown in Fig. 6.13. It can be seen that there is approximately 10% difference between the predicted and experimental data. Moreover, the predicted load was higher than the experiment at the same displacement. One possible reason could be the adversely affected surface integrity by laser cutting process. After laser cutting, surface striation, recast layer, and heat affect zone could reduce the material stiffness, which leads to the load – displacement curve shifting down as compared to the simulation results.

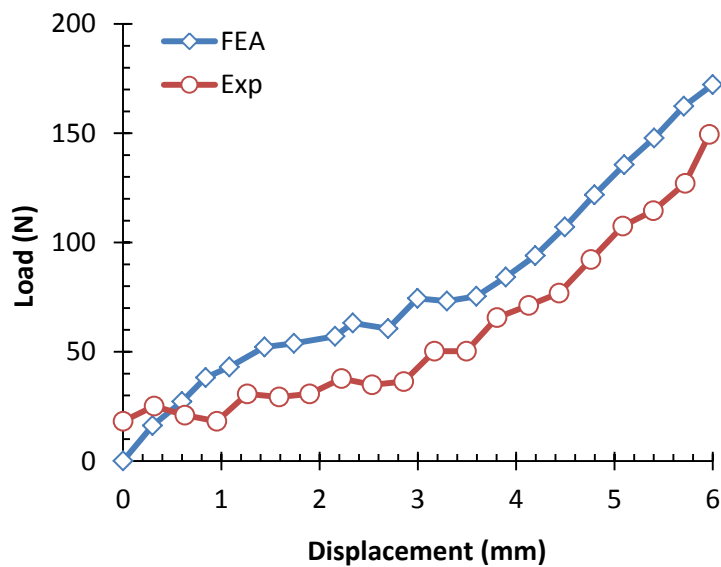


Fig. 6.13 Predicted load – displacement curve and the experimental data.

6.6.2 Stress Evolution

Fig. 6.14 shows the von Mises evolution as the displacement changes from 0 mm to 6 mm. It can be seen that the stress concentration sites correspond to the fracture sites in the experiment. As the displacement becomes larger, the stress magnitude increases. The maximum von Mises stress was 1.2 GPa, which is larger than the yield stress (approximately 0.6 GPa).

Fig. 6.15 shows the stress in Y direction (S_{22}) along the width of the strut. It was found that the inner surface of the knee is under tension, while the outer surface is under compression. As the displacement increases, the magnitude of tensile and compressive stresses increase. The tensile stress on the inner surface of the knee region is responsible for opening the micro-notches as results of the very rough surface striation. Therefore, it could be inferred that the inner surface of the knee region is most susceptible to fracture. In addition, crack growth direction is from the inner surface to the outer surface.

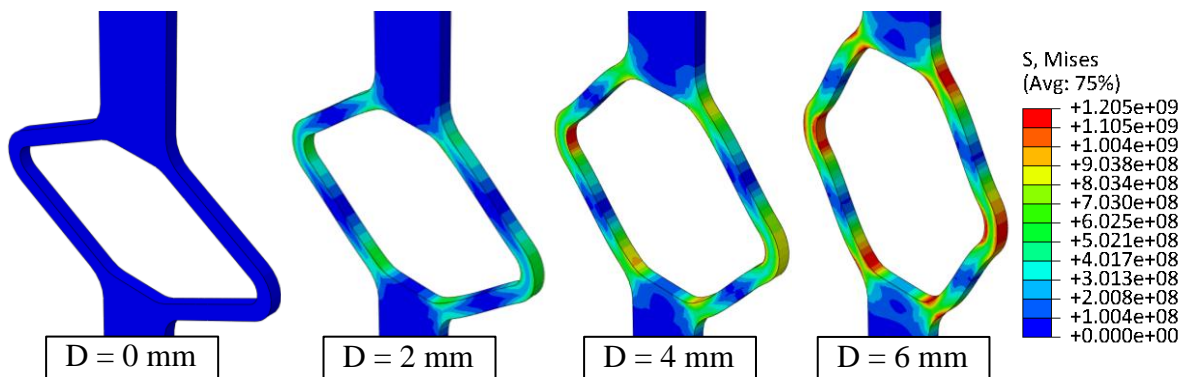


Fig. 6.14 von Mises stress evolution at different displacements.

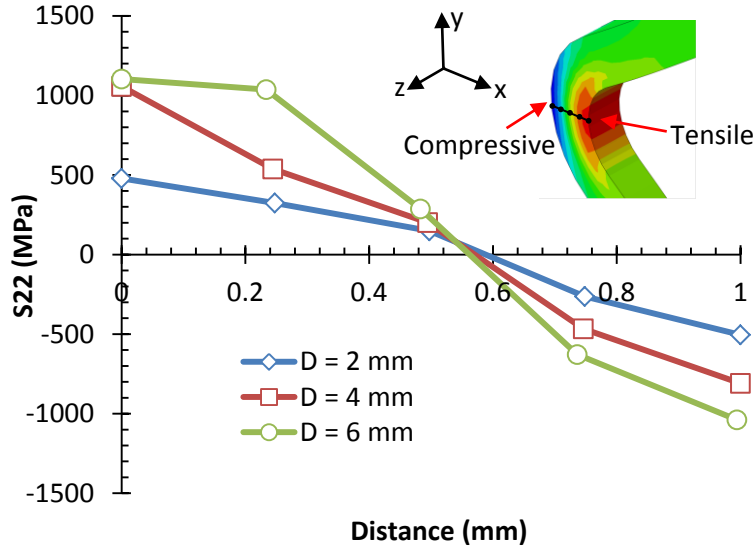


Fig. 6.15 S22 distribution along the thickness direction at different displacements.

6.6.3 Phase Transformation

It is very challenging to experimentally observe the phase transformation by studying the microstructure of Nitinol. Since revealing the microstructure requires polishing, which is a mechanical process that can easily induce martensitic transformation. The polish induced martensites will be mixed up with temperature/stress induced martensite and bring uncertainty to the analysis [25]. Therefore, in this study, finite element analysis was used as an alternative to investigate the phase transformation under tensile loading. Fig. 6.16 shows the martensitic phase transformation in the inner surface of the knee region as displacement increases. Results indicated that the martensitic phase transformation was started at displacement of 0.6 mm. For all the fractured samples in the tensile and fatigue experiments, the displacements were larger than 0.6 mm. Therefore, the fractured sites were all at partially or fully martensite state. These stress induced martensites are known to have lower fracture toughness, when compared to fully

austenite Nitinol [32]. Hence, it could be inferred that the stress induced martensite will further adversely affect the tensile and fatigue strength.

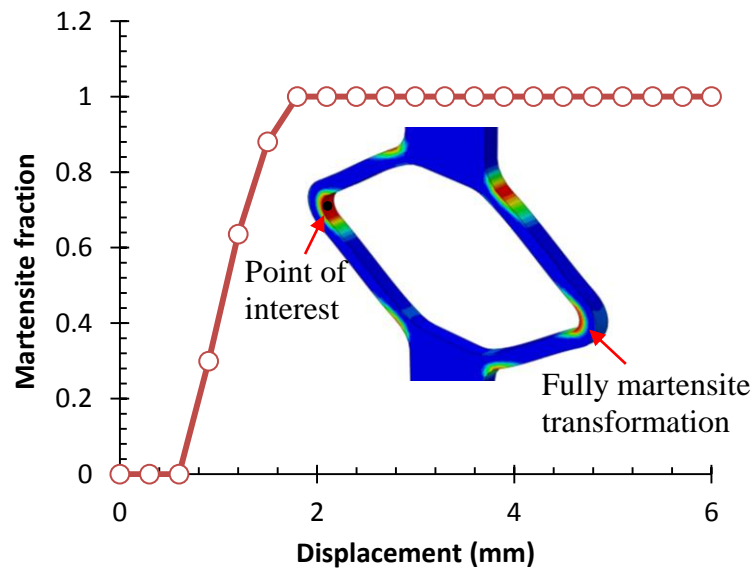


Fig. 6.16 Martensitic transformation at the stress concentration locations.

6.7 Conclusions

This study focuses on the effect of surface integrity on the tensile and fatigue strength of Nitinol by laser cutting. Three levels of surface integrity were produced by varying the laser cutting parameters. A finite element analysis was also performed to correlate the surface integrity, stress concentration, phase transformation, and the tensile and fatigue strength of the Nitinol samples. Key findings are summarized as follows:

- Poor surface integrity induced by laser cutting adversely affects the tensile and fatigue strength of Nitinol. Fatigue life was affected by surface integrity as an integral factor instead of a single surface integrity characteristic.

- The heat affected zone after laser cutting is not detectable due to the large grain size in the bulk material.
- The inner surface of the knee region of the diamond Nitinol sample is the most susceptible sites for fracture due to the tensile stress concentration which induces martensitic phase transformation.

6.8 Reference

- [1] Y. Guo, A. Klink, C. Fu, J. Snyder, 2013, Machinability and surface integrity of Nitinol shape memory alloy, *CIRP Annals - Manufacturing Technology*, 62(1):83-86.
- [2] N. Figueira, T. Silva, M. Carmezim, J. Fernandes, 2009, Corrosion behaviour of NiTi alloy, *Electrochimica Acta*, 54(3):921-926.
- [3] D. Stoeckel, A. Pelton, T. Duerig, 2004, Self-expanding Nitinol stents: Material and design considerations, *European radiology*, 14(2):292-301.
- [4] H.J. Chun, E.S. Kim, J.J. Hyun, Y.D. Kwon, B. Keum, C.D. Kim, 2010, Gastrointestinal and biliary stents, *Journal of gastroenterology and hepatology*, 25(2):234-243.
- [5] D. Stoeckel, C. Bonsignore, S. Duda, 2002, A survey of stent designs, *Minimally Invasive Therapy & Allied Technologies*, 11(4):137-147.
- [6] I. Watanabe, M. McBride, P. Newton, K.S. Kurtz, 2009, Laser surface treatment to improve mechanical properties of cast titanium, *Dental Materials*, 25(5):629-633.
- [7] A. Poulon-Quintin, I. Watanabe, E. Watanabe, C. Bertrand, 2012, Microstructure and mechanical properties of surface treated cast titanium with nd:YAG laser, *Dental Materials*, 28(9):945-951.
- [8] A. Shojaei Zoeram, S.A.A. Akbari Mousavi, 2014, Laser welding of Ti-6Al-4V to Nitinol, *Materials & Design*, 61(0):185-190.
- [9] J.Y. He, K.W. Gao, Y.J. Su, L.J. Qiao, W.Y. Chu, 2004, The role of hydride, martensite and atomic hydrogen in hydrogen-induced delayed fracture of TiNi alloy, *Materials Science and Engineering: A*, 364(1-2):333-338.
- [10] M. Khan, S. Panda, Y. Zhou, 2008, Effects of welding parameters on the mechanical performance of laser welded Nitinol, *Materials Transaction.*, 49(11):2702-2708.

- [11] H.I. Dawood, K.S. Mohammed, A. Rahmat, U. M.B., 2015, The influence of the surface roughness on the microstructures and mechanical properties of 6061 aluminium alloy using friction stir welding, *Surface and Coatings Technology*, 270(0):272-283.
- [12] G.A. Porter, P.K. Liaw, T.N. Tieg, K.H. Wu, 2001, Fatigue and fracture behavior of nickel–titanium shape-memory alloy reinforced aluminum composites, *Materials Science and Engineering: A*, 314(1–2):186-193.
- [13] J.M. McNaney, V. Imbeni, Y. Jung, P. Papadopoulos, R. Ritchie, 2003, An experimental study of the superelastic effect in a shape-memory Nitinol alloy under biaxial loading, *Mechanics of Materials*, 35(10):969-986.
- [14] M. Khan, Y. Zhou, 2010, Effects of local phase conversion on the tensile loading of pulsed nd: YAG laser processed Nitinol, *Materials Science and Engineering: A*, 527(23):6235-6238.
- [15] S. Miyazaki, Y. Sugaya, K. Otsuka, 1988, Effects of various factors on fatigue life of ti-ni alloys, 9:251-256.
- [16] M. Wagner, T. Sawaguchi, G. Kausträter, D. Höffken, G. Eggeler, 2004, Structural fatigue of pseudoelastic NiTi shape memory wires, *Materials Science and Engineering: A*, 378(1):105-109.
- [17] J.M. Young, K.J. Van Vliet, 2005, Predicting in vivo failure of pseudoelastic NiTi devices under low cycle, high amplitude fatigue, *Journal of Biomedical Materials Research Part B: Applied Biomaterials*, 72(1):17-26.
- [18] A.M. Figueiredo, P. Modenesi, V. Buono, 2009, Low-cycle fatigue life of superelastic NiTi wires, *International Journal of Fatigue*, 31(4):751-758.
- [19] D. Tolomeo, S. Davidson, M. Santinoranout, 2000, Cyclic properties of superelastic Nitinol: Design implications, :409-417.
- [20] A. Pelton, V. Schroeder, M. Mitchell, X.Y. Gong, M. Barney, S. Robertson, 2008, Fatigue and durability of Nitinol stents, *Journal of the mechanical behavior of biomedical materials*, 1(2):153-164.
- [21] S. Robertson, A. Pelton, R. Ritchie, 2012, Mechanical fatigue and fracture of Nitinol, *International Materials Reviews*, 57(1):1-37.
- [22] Bannantine JA, Comer JJ, Handrock JL. 1990. *Fundamentals of metal fatigue analysis*. Prentice Hall Englewood Cliffs, NJ.
- [23] A. Javidi, U. Rieger, W. Eichlseder, 2008, The effect of machining on the surface integrity and fatigue life, *International Journal of Fatigue*, 30(10):2050-2055.
- [24] C. Fu, J. Liu, A. Guo, 2015, Statistical characteristics of surface integrity by fiber laser cutting of Nitinol vascular stents, *Applied Surface Science*, .

- [25] C.H. Fu, M.P. Sealy, Y.B. Guo, X.T. Wei, 2014, Austenite–martensite phase transformation of biomedical Nitinol by ball burnishing, *Journal of Materials Processing Technology*, 214(12):3122-3130.
- [26] Y. Ogata, M. Takatugu, T. Kunimasa, K. Uenishi, K.F. Kobayashi, 2004, Tensile strength and pseudo-elasticity of YAG laser spot melted ti-ni shape memory alloy wires, *Materials Transactions*, 45(4):1070-1076.
- [27] D. McGrath, M. Bruzzi, P. McHugh, 2014, Nitinol stent design–understanding axial buckling, *Journal of the mechanical behavior of biomedical materials*, 40:252-263.
- [28] C. Fu, Y. Guo, J. McKinney, X. Wei, 2012, Process mechanics of low plasticity burnishing of Nitinol alloy, *Journal of Materials Engineering and Performance*, 21:2607-2617.
- [29] F. Auricchio, R.L. Taylor, 1997, Shape-memory alloys: Modelling and numerical simulations of the finite-strain superelastic behavior, *Computer Methods in Applied Mechanics and Engineering*, 143(1):175-194.
- [30] M. Conti, F. Auricchio, M. De Beule, B. Verheghe, 2009, Numerical simulation of Nitinol peripheral stents: From laser-cutting to deployment in a patient specific anatomy.
- [31] Dassault Systèmes, 2013, UMAT for superelasticity and plasticity of shape memory alloys, Abaqus, .
- [32] R.L. Holtz, K. Sadananda, M.A. Imam, 1999, Fatigue thresholds of ni-ti alloy near the shape memory transition temperature, *International Journal of Fatigue*, 21, Supplement 1(0):S137-S145.

CHAPTER 7

SUMMARY, CONCLUSIONS AND RECOMMENDATIONS

7.1 Summary and Conclusions

The major objectives of this research are to (1) better understand Nitinol alloy; (2) study fiber laser cutting mechanisms of Nitinol for optimal surface integrity in medical device applications; and (3) establish the relationship between laser cutting, surface integrity, and functionality of the laser cut samples. To achieve these objectives, low plasticity burnishing process was first applied to understand the deformation behavior of superelastic Nitinol. Then, a fiber laser cutting system was developed to cut Nitinol for surface integrity characterization. The laser cutting process window has been identified for optimal surface integrity. Also, to better understand the process mechanism of laser cutting Nitinol, a 3-dimensional finite element analysis has been developed by integrating a novel moving volumetric heat flux model at the pulse mode and the phase-dependent superelastic Nitinol material property. Tensile and fatigue testing was also conducted to correlate surface integrity and sample performance. It was found that the tensile and fatigue strength of laser cut Nitinol samples was highly related to surface integrity. Specifically, the tensile and fatigue strength can be significantly improved by adjusting surface integrity in a laser cutting process.

7.2 Recommendations

7.2.1 Improvement on the Laser Cutting Process

In this study, a fiber laser cutting system has been developed. The rationale for developing the fiber laser cutting system rather than other types of lasers such as Nd:YAG or ultrafast lasers is that fiber laser has better beam quality with relative low cost. Nevertheless, fiber laser cutting is still a thermal process which induces thermal damage. To eliminate or mitigate the thermal damage, it is suggested that a water assisted laser cutting system be developed. A schematic of the water assisted laser cutting system is shown in Fig. 7.1.

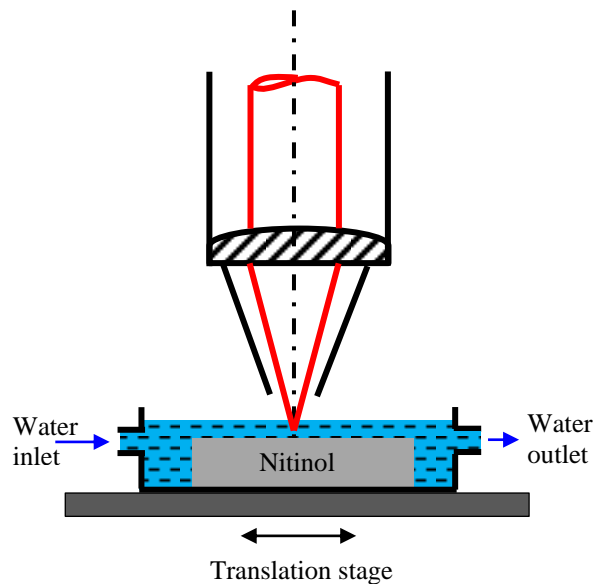


Fig. 7.1 Schematic of water assisted laser cutting setup.

The water cools the cut area and eliminates any thermal damage such as HAZ and micro-cracks. The flowing water also flushes away the laser ablated material debris so that contamination can be reduced and part accuracy can be increased. However, the challenge of developing such a system is that the water layer thickness needs to be precisely controlled so that

it will not interfere with the focus of the laser beam. Furthermore, inducing water to a high precision CNC system could be a hazard to the electrical system.

7.2.2 Surface Treatment after Laser Cutting

In medical device industry, it is a standard practice to use electropolishing process to remove burrs and improve surface integrity of a laser cut Nitinol device. However, the detailed electropolishing process is treated as trade secrets and therefore not accessible in the public domain. In this study, there was no surface treatment applied to laser cut samples since one of the objectives of this study is to establish the relationship between surface integrity and performance. If surface treatment is applied, surface integrity by laser cutting will be altered and would not reflect the original surface integrity of the as-cut samples. However, it is suggested that the surface treatment be applied to laser cut samples in a future research to develop an effective post process to enhance the performance of the laser cut devices. Such a post process is critical since there is no “standardized” surface treatment available to improve the surface integrity of the laser cut Nitinol devices.

7.2.3 Fatigue Testing

In this study, the preliminary fatigue data was obtained to establish the relationship between surface integrity and fatigue after laser cutting. It is suggested that more sophisticated fatigue testing be performed in the near future to more closely mimic the complex in-vivo loading condition. In addition, it is suggested that strain – life curve be used to evaluate the effectiveness of the laser cutting process as well as the subsequent post process.